Adjoint Based Uncertainty Quantification and Sensitivity Analysis for Nuclear Thermal-Fluids Codes

by

Timothy J. Drzewiecki

A dissertation submitted in partial fulfillment
of the requirements for the degree of
Doctor of Philosophy
(Nuclear Engineering and Radiological Sciences)
in the University of Michigan
2013

Doctoral Committee:

Professor Thomas J. Downar, Co-Chair
Associate Professor Annalisa Manera, Co-Chair
Assistant Professor Krzysztof J. Fidkowski
Professor John C. Lee

A C K N O W L E D G M E N T S

I would like to start by thanking my advisors Prof. Downar and Prof. Manera for bringing me to Michigan, providing guidance and support, and providing an outstanding Ph.D experience. I am very appreciative of the numerous opportunities that I've had to receive training, give talks, and work with scholars from abroad.

I would like to express my gratitude to the other members of my committee. It was in a collaborative work with Prof. Fidkowski that I became interested in sensitivity analysis and UQ, and it was he who provided the material that introduced me to the adjoint method. Prof. Lee introduced me the probabilistic side of safety analysis in his Risk and Safety Analysis class and generously shared his time and knowledge.

The following individuals made significant contributions to this work. Joseph M. Kelly of the U.S. NRC was instrumental in laying out the design for the primal system of the AGREE code. The work of Dr. Nam-Il Tak of KAERI during his sabbatical at the University of Michigan provided the validation basis for the AGREE code. It was Dr. Tak that set up the test cases for the SNU bypass flow tests, and HENDEL validation tests. A special appreciation goes out to Dr. Volkan Seker, whom I worked with closely during my Ph.D studies. His guidance and friendship are appreciated.

I would like to express my gratitude to my wife, Sengul, for the support, encouragement, and patience provided over the past four years. My pursuit of the Ph.D would not have been possible without her personal sacrifices.

I would like to recognize the US DOE NEUP fellowship program that provided financial support from 2009-2012.

TABLE OF CONTENTS

LIST OF FIGURES

LIST OF TABLES

LIST OF APPENDICES

LIST OF ABBREVIATIONS

AGREE Advanced Gas REactor Evaluator

BE Best Estimate

BEPU Best Estimate Plus Uncertainty

CDF Cumulative Distribution Function

CFD Computational Fluid Dynamics

CSAU Code Scaling, Applicability, and Uncertainty

ECCS Emergency Core Cooling System

HTTR High Temperature Test Reactor

LWRs Light Water Reactors

MDNBR Minimum Departure from Nucleate Boiling Ratio

NGNP Next Generation Nuclear Plant

PBA Probability Bounds Analysis

PIRT Phenomena Identification and Ranking Table

PDF Probability Distribution Function

PMR Prismatic Module Reactor

PWR Pressurized Water Reactor

SRQ System Response Quantity

UQ Uncertainty Quantification

ABSTRACT

Adjoint Based Uncertainty Quantification and Sensitivity Analysis for Nuclear Thermal-Fluids Codes

by

Timothy J. Drzewiecki

Chair: Prof. Thomas J. Downar and Prof. Annalisa Manera

Safety analysis in nuclear engineering has been adopting a best estimate plus uncertainty (BEPU) approach over a traditional conservative approach in order to provide more realistic estimates of plant safety margins. Traditionally, these BEPU approaches have relied on an expensive phenomena identification and table (PIRT) process to identify the most significant contributors to uncertainty. More recent work has utilized statistical-based sensitivity measures (e.g. the Spearman rank correlation coefficient) to highlight the important contributors to uncertainty. Currently, the most popular method for dealing with uncertainty is based on the Wilks' formula, where a specified number of calculations needs to be performed in order to establish a certain confidence level of a certain reliability. These methods have the advantage that a relatively limited number of runs needs to be performed, typically less than 100. Situations exist, however, where one is required to exhaustively sample the space of uncertain input parameters. In these situations, where tens of thousands of calculations may be required, sampling the true function may be too computationally expensive and a surrogate is sampled in place of the true function.

In this thesis the various methods of obtaining sensitivity derivatives are explored in order to highlight the significant contributors of uncertainty, and the adjoint approach is shown to be the most efficient. The implementation of the adjoint method into the NRC Advanced Gas REactor Evaluator (AGREE) code is performed. Additionally, a method for obtaining an approximation that has a leading error term of third order is derived by calculating both forward and adjoint sensitivities. The approximation is demonstrated to be accurate locally. A method for combining these surrogates is demonstrated using the DAKOTA code. The utility of the method is demonstrated by performing three different analyses related to the High Temperature Test Reactor (HTTR) in Japan. First, the bypass flow experiment of Kaburaki and Takizuka is analyzed to inspect the sensitivity and variability of the bypass flow with respect to the cross-flow gap geometry, loss coefficient and boundary conditions. Next, the HENDEL experiment is analyzed to investigate the factors impacting peak core temperatures and the initial amount of stored energy in the core. Last, an analysis of the actual HTTR reactor is performed. A key result from these analyses is that the cross-flow gap geometry and loss coefficients were of relatively low significance with regard to the quantities that pertain to core temperature.

In addition to the implementation of the adjoint and surrogate, this thesis presents the development, verification, and validation of the fluids models in the AGREE code. To aid in the potential licensing of the NGNP, the AGREE code was developed to support the US NRC NGNP evaluation model. A review of existing methods is presented and a set of code requirements is discussed along with the mathematical model of the code. Validation of the fluids portion of the code is performed by comparing calculations against data taken from bypass flow experiments performed by JAERI and Seoul National University.

CHAPTER 1

Introduction

1.1 Motivation

The purpose of computing is insight, not numbers is a motto commonly heard in the realm of scientific computing [1]. Although this motto is certainly true, it is frequently the case in nuclear engineering that the necessary insight regarding the performance of a system can be expressed by a single number (e.g. peak stresses or temperatures in structural components, reactivity coefficients for a reactor core, Minimum Departure from Nucleate Boiling Ratio (MDNBR) in a Pressurized Water Reactor (PWR)). In this document such a number will be referred as a System Response Quantity (SRQ). When arriving at a SRQ via a computational code, one is faced with a credibility issue (i.e. whether the results from the calculation are worthy of belief or confidence).

In the analysis of complex systems for reliability and safety related performance, computing can be utilized in two different situations. The first situation is to supplement test-based engineering. For example, in the development of gas turbines, commercial and military aircraft, and rocket engines, these systems go through a long and careful development process based on testing, modification, and retesting [2]. In this type of test driven environment, computing plays more of a supportive role. The second situation is to depend almost entirely on computational results. This second situation is frequently encountered in nuclear engineering, where engineers are tasked with analysing the response of a complex engineering system to postulated accidents with severe health, financial, and environmental implications. These types of high-consequence system analyses attempt to predict events that rarely, if ever, occur. For these types of analyses, the burden of credibility and confidence that is required of scientific computing is much higher than when scientific computing supplements test-based engineering.

In nuclear engineering a paradigm of this issue can be taken from Emergency Core Cooling System (ECCS) performance analysis for Light Water Reactors (LWRs). Due to

limitations in knowledge, early evaluation methods were based on a conservative approach, as outlined in 10 CFR 50 Appendix K [3]. As research progressed and Best Estimate (BE) codes matured a move toward Best Estimate Plus Uncertainty (BEPU) methodologies occurred. The Code Scaling, Applicability, and Uncertainty (CSAU) methodology [4–8] has now become the standard for modern evaluation of nuclear systems and recent work has been focused on improving the CSAU methodology through the use of forward sensitivity analysis [9].

The fundamental elements that build credibility in computational results are specified in Table 1.1 [2]. This thesis will addresses all items of credibility related to code development with an emphasis placed on item 4, uncertainty quantification and sensitivity analysis. The following sections will provide background on uncertainty quantification and sensitivity analysis, introduce the Advanced Gas REactor Evaluator (AGREE) thermal-fluids code, highlight the contributions of this thesis, and layout the remainder of the report.

Table 1.1: Elements of Credibility for Computational Results

1.	Quality of the analysts conducting the work
2.	Quality of the physics modeling
3.	Verification and validation activities
4.	Uncertainty quantification and sensitivity analysis

1.2 Uncertainty Quantification and Sensitivity Analysis

Uncertainty quantification and sensitivity analysis critically contribute to credibility in scientific computing by informing the user of the simulation results how uncertain the results are and what input parameters are the most important. Uncertainty quantification of experimental data is a well understood topic that is often covered in undergraduate thermal-fluids texts [10], whereas the quantification of uncertainty in computational results remains an active area of research. A computation brings together what is known and what is uncertain in the analysis of a system. Thus it becomes critical to discuss how uncertainty in treated in a computation, and and how these uncertainties propagate through the simulation.

1.2.1 Sources of Uncertainties

Uncertainties in a simulation can originate from many sources, including: uncertainties in initial conditions, uncertainties in boundary conditions, uncertainties regarding the physical

geometry of the system, uncertainties attributed to the mathematical models and constitutive relationships that describe the physical processes. Additionally, numerical errors can also be treated as sources of variation. These errors include: errors attributed to the discretization of the continuous field equations, errors resulting from the use of finite precision floating point computations, and errors attributed to the residual of the iterative solvers.

Two fundamental types of classification, aleatory and epistemic [11], are encountered when setting up a simulation. Aleatory uncertainty is attributed to physical variability present in the system being analysed or its environment. It is not strictly due to a lack of knowledge and cannot be reduced. Common examples of aleatory uncertainty are random variations in manufacturing tolerances, material composition, test conditions, and environmental factors. Aleatory uncertainty is generally characterized by a Probability Distribution Function (PDF) or a Cumulative Distribution Function (CDF). Epistemic uncertainty is attributed to a lack of knowledge and can be reduced by a combination of calibration, inference from experimental observations and improvement of the physical models [12]. Epistemic uncertainty is traditionally represented as either an interval with no associated PDF or a PDF which represents the degree of belief of the analyst (as opposed to frequency of occurrence of an event in aleatory uncertainty) [13].

1.2.2 Propagation of Uncertainties

Once the sources of uncertainties have been quantified, these uncertainties need to be propagated through the simulation to the SRQ. SRQs are functions of all the variables that describe the sources of uncertainty. The primary method for the propagation of uncertainty is the sampling or Monte-Carlo method.

In the Monte-Carlo method, the sources of uncertainty are sampled as random variables according to their PDF and used as inputs to a series of deterministic calculations. The output from the deterministic calculations can then be used to produce an empirical PDF for a probabilistic based analysis, or a p-box for a Probability Bounds Analysis (PBA) [13]. Sampling methods are a common approach because of a number of advantages: (a) they can be applied to essentially any type of mathematical model, regardless of the model's complexity or nonlinearity; (b) they can be applied to both aleatory and epistemic uncertainties, regardless of the magnitude of their uncertainties; and (c) they are not intrusive to the numerical solution of the mathematical model (i.e. sampling is done outside of the numerical solution of the PDEs) [2]. Additionally, Monte-Carlo methods are naturally insensitive to the dimensionality of the parameter space.

1.2.3 Wilks' Formula and 95/95

A popular practice for dealing with uncertainty in nuclear safety calculations is to utilize BE codes and nonparametric statistics [14–16] to ensure that a system demonstrates 95% reliability with 95% confidence, (95/95). This method is attributed to Wilks [17, 18] and assumes that all uncertainty parameters are independent, i.e. no correlation between them. It can be understood as follows, by considering a one-sided probability and invoking the binomial distribution we arrive at Eq. 1.1 [19]. The minimum number of calculations required to achieve a desired confidence level, α, assuming a reliability, μ, is provided in Table 1.2. It becomes apparent from the values in Table 1.2 that 95/95 can be achieved by performing only 59 calculations. It should be noted, however, that a simple use of Eq. 1.1 may not provide a sufficiently robust statistical estimate of the uncertainties involved since only a relatively small portion of the input parameter space may be sampled [19].

$$P\{\text{obtaining at least } k \text{ values } y \geq y^*\} = 1 - \sum_{m=0}^{k-1} \binom{N}{m} \mu^{N-m}(1-\mu)^m = \alpha \tag{1.1}$$

with

$$\mu = P\{y < y^*\} \tag{1.2}$$

Table 1.2: Minimum of calculations for one-sided statistical tolerance limit

	$k=1$		$k=2$	
α/μ	0.95	0.99	0.95	0.99
0.95	59	299	93	473
0.99	90	459	130	662

1.2.4 Surrogates

Wilks' formula is a powerful tool for establishing confidence bounds regarding the reliability of a system. There are situations, however, where one is interested in exhaustively sampling the model. In particular, if one is interested in the distribution of the SRQ, or range of possible outcomes, then a much larger sample size must be obtained. Sampling the true function may not be viable if the function evaluation is expensive, and an inexpensive surrogate is used in its place. Much work in the Uncertainty Quantification (UQ) is involved with constructing accurate surrogates. It can be argued that the distinguishing

feature in the field of UQ is that the function evaluation is computationally expensive [20]. There are several approaches to building surrogates, but the most popular can be categorized as resposne surface models, polynomial chaos, and sensitivity methods.

There are several approaches to building response surfaces including kriging interpolation [21], the Multivariate Adaptive Regression Spline (MARS) function approximation method [22]. the Alternating Conditional Expectation (ACE) algorithm [23, 24], and the Gaussian Process Model [25]. Use of these response surface models can be a relatively painless process as kriging, MARS, and GPM have been implemented into the large-scale engineering optimization and uncertainty analysis software DAKOTA [26]. These response surfaces, however, tend to have limitations regarding the number of input parameters [27] and can become ill-conditioned if the number of samples becomes too large [28].

Polynomial chaos methods can go by many names including but not limited to: generalized polynomial chaos, stochastic Galerkin, stochastic collocation, probabilistic collocation, and non-intrusive spectral projection [20]. Although there may be differences in the approach, the results are often equivalent (e.g. collocation is Galerkin via Guass quatrature, see Theorem 16 from Boyd [29]). The main idea in all these approaches is the same, which is to build a polynomial surrogate of the solution in terms of the uncertain parameters. For a deterministic equation of the form in Eq. 1.3 with an associated objective function describing some SRQ, $J(u)$, we seek a solution of the form in Eq. 1.4, where $\mathscr{L}$ is an integro-differential operator, $\mathbf{x}$ is the spatial variable, t is the temporal variable, $\mathbf{s}$ is the collective of random variables that represent the uncertain parameters, and f is a source term.

$$\mathscr{L}u(\mathbf{x},t;\mathbf{s}) = f \tag{1.3}$$

$$J(\mathbf{s}) \approx \sum_{i=1}^{M} \hat{J}_i \Phi(\mathbf{s}) \tag{1.4}$$

The expansion of the objective function and its coefficients is the final result of the polynomial chaos analysis [30] and has the advantage that many important statistics, such as mean and variance, can be analytically calculated from this expansion. Additionally, sampling Eq. 1.4 is inexpensive and can be used, in combination with Monte-Carlo analysis, to determine more complex statistics. The major drawback of polynomial chaos methods is the curse of dimensionality. The number of terms in the polynomial expansion expressed by Eq. 1.4 grows rapidly with an increase in dimension. To give perspective, the number of grid points required for a 10 and 20 dimension interpolation is given for tensor product and total degree grids in Table 1.3 (cardinality of tensor product grid is calculated as $(N+1)^d$, and the cardinality of the total degree grid is calculated as $\frac{(N+d)!}{N!d!}$). Even for these modest

sized problems the number of function evaluations required can be cost prohibitive. Current research, such as sparse (Smolyak) grids, is focused on reducing the required number of calculations.

Table 1.3: Cardinality of Interpolation Grids

Dimension (d)	Truncation (N)	Tensor Product	Total Degree
10	1	1,024	11
	2	59,049	66
	3	1,048,576	286
	4	9,765,625	1001
20	1	1,048,576	21
	2	348,678,440	231

Sensitivity-based methods are a class of uncertainty propagation methods that use the derivatives of the SRQ with respect to the random variables describing the sources of uncertainty, i.e. the sensitivity derivative, $\frac{dJ}{ds}$ [31]. There are multiple ways to utilize the sensitivities in propagating the uncertainty. One method is to use the sensitivity derivatives to build a first or second order Taylor series approximation to the objective function as shown in Eq. 1.5, where μ is the mean, $G_i = \frac{dJ}{ds_i}\big|_\mu$, and $H_{i,k} = \frac{d^2J}{ds_i ds_k}\big|_\mu$.

$$J(\mathbf{s}) = J(\mu) + \sum_i G_i \delta s_i + \frac{1}{2}\sum_{i,k} H_{i,k}\delta s_i \delta s_k + O(\|\delta \mathbf{s}\|^3) \tag{1.5}$$

From a probabilistic standpoint, we can obtain approximations to the mean and variance directly by taking moments about Eq. 1.5 [32]. Additionally, the Taylor series approximation may be used as a surrogate for Monte-Carlo sampling for a probability bounds analysis. Approximating the objective function by its Taylor series is an efficient way of producing a surrogate, but may not be accurate for uncertain parameters over a large range of variability. In this case, the sensitivity derivatives can be utilized to reduce the dimension space of the random variables in order to make one of a response surface or polynomial chaos method more feasible.

There are several ways to compute sensitivity derivatives, including finite differencing, the tangent-linear approach, and the adjoint approach. As will be shown in Ch. 3, the adjoint approach is the clear choice when the number of SRQs is much smaller than the dimensionality of the uncertain parameter space. This thesis is focused on nuclear system codes for analysing complex systems with a large number of uncertain input parameters. These analyses are typically focused on a few SRQs, such as peak temperatures and pressures. From the preceding discussion regarding the methods of uncertainty propagation, the adjoint based sensitivity approach will be the focus in this thesis.

1.3 The Advanced Gas REactor Evaluator (AGREE)

The AGREE code was originally developed as a multiphysics simulation code to perform design and safety analysis of next generation Pebble Bed High Temperature Gas Cooled Reactors [33]. AGREE utilizes a suite of code modules to solve the coupled thermal-fluids and neutronics field equations. The thermal-fluids module is based on the three dimensional solution of the mass, momentum, and energy equations in cylindrical coordinates within the framework of the porous media method. The neutronics module is a part of the PARCS code and provides a fine mesh finite difference solution of the neutron diffusion equation in three dimensional cylindrical coordinates [34]. Over the past few years, a rigorous effort has been in place to extend the capabilities of AGREE in order to model Prismatic Module Reactor (PMR)s in support of the US NRC Next Generation Nuclear Plant (NGNP) evaluation model [35–40]. The development of the AGREE code, along with the associated verification and validation, constitutes a significant part of the thesis work. Adjoint implementation, and the associated uncertainty quantification and sensitivity analysis, will further extend the capabilities of AGREE and provide additional credibility to PMR analyses. Details of the primal equations in the AGREE code are provided in Ch. 2

1.4 Accomplishments

The accomplishments and original contributions of this thesis consist of:

- Development, verification, and validation of the AGREE thermal-fluids code.
- A generalized and simple method for the implementation of the adjoint solution into large system codes.
- Identification and quantification of the factors impacting bypass flow and core temperatures in the NGNP.
- Development and study in the use of adjoint corrected approximations as a surrogate in nuclear thermal-fluids codes.

The first contribution is the *development, verification, and validation of the AGREE thermal-fluids code*. Although other codes exist for the analysis of PMR cores, as will be discussed in Ch. 2, the AGREE code is unique in its scale and approach. The approach utilized in AGREE was decided upon after reviewing existing approaches for their strengths and weaknesses and ultimately deciding on a unique path.

The second contribution is *a generalized and simple method for the implementation of the adjoint solution into large system codes*. An implementation of local sensitivity derivatives into the RELAP5/MOD3.2 code [41] was based off of the early work of Cacuci et. al. [42–44]. This rigorous approach is rooted in functional analysis, and can be difficult to grasp and implement. The approach outlined in this thesis is greatly simplified as it relies on the discrete adjoint (see Ch. 3).

A similar situation exists in the commercial CFD community. Many of these codes utilize the (Semi-Implicit Method for Pressure Linked Equations) SIMPLE algorithm of Patankar [45] or one of its derivatives (SIMPLEC, SIMPLER, PISO) [46]. The difficulty in calculating the adjoint in SIMPLE based codes is that the Jacobian matrix of the coupled system is not available. Approaches for overcoming this obstacle involve formulating the continuous adjoint system (along with the associated boundary and initial conditions) or a hybrid approach utilizing both discrete and continuous adjoints [47]. The approach outlined in this thesis is to retain the SIMPLE algorithm as a preconditoiner for a Newton solver, which deals directly with the continuity equation.

The third contribution is the *identification and quantification of the factors impacting bypass flow and core temperatures in the NGNP*. Current guidance in regards to sources of uncertainty and their importance has relied on expert opinion in the form of a Phenomena Identification and Ranking Table (PIRT) [48]. The adjoint implementation into the AGREE code would quantify the effect of this uncertainty on the key SRQs. Such information can be used to identify current weaknesses in the NGNP evaluation model and provide guidance on future experiments.

The final contribution is a *study of adjoint corrected approximations as a surrogate to the application of systems codes*. There has been some work in the aerospace Computational Fluid Dynamics (CFD) community, utilizing second order adjoints, that has produced approximations of the mean and variance of SRQs within a few percent of a brute force Monte-Carlo simulation [49]. Similarly, a recent work has utilized a linear surrogate function, built from the adjoint solution, as an acceleration scheme for a Monte-Carlo based risk assessment [50]. Adjoint corrected approximations to SRQs can be obtained that have a leading error term of third order with respect to input parameter perturbation. By combining several of these surrogates one can build an accurate surrogate that can utilize inputs from non-parametric statistics evaluations, is not sensitive to the number of inputs, and does not suffer from ill-posedness resulting from sample size.

1.5 Layout of the Report

This thesis is broken up into four parts, namely, the introduction, primal system, adjoint theory and implementation, and conclusions. In this introductory chapter the motivation for the work was discussed. The main ideas in uncertainty quantification and sensitivity analyses have been discussed along with a short introduction to the AGREE code. Finally, the contributions of the proposed thesis have been highlighted. The primal system, the AGREE code will be described in detail in Ch. 2 along with some verification and validation calculations. A discussion of the adjoint method is provided in Ch. 3 and details of its implementation and testing are provided in Ch. 4. Concluding remarks are provided at the end along with suggestions on future research and a candid discussion on lessons learned during the production of this work.

CHAPTER 2

The Primal System (AGREE)

2.1 Introduction

The US Department of Energy (DOE) has determined that the Next Generation Nuclear Plant (NGNP) will be a VHTR (Very High Temperature Reactor) for the production of electricity, process heat, and hydrogen [51]. To aid in the potential licensing process of the NGNP, the Advanced Gas REactor Evaluator (AGREE) program was developed in support of the NRC NGNP evaluation model, shown in Fig. 2.1. AGREE is designed to be capable of modeling the thermal-fluid conditions of Pebble Bed Reactors (PBRs) and Prismatic Modular Reactors (PMRs), core shown in Fig. 2.2, and will be linked to PARCS to capture the thermal-fluid reactivity feedback.

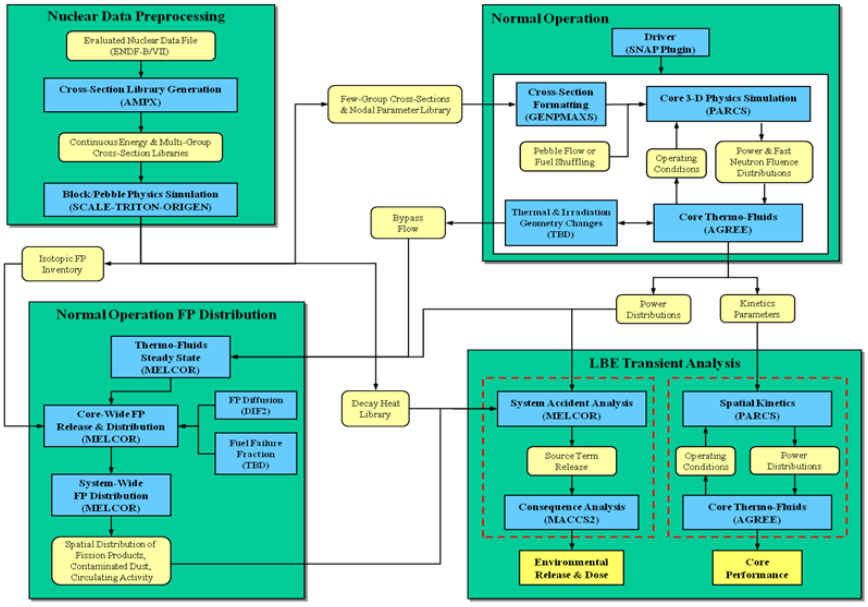

Figure 2.1: US NRC NGNP Evaluation Model

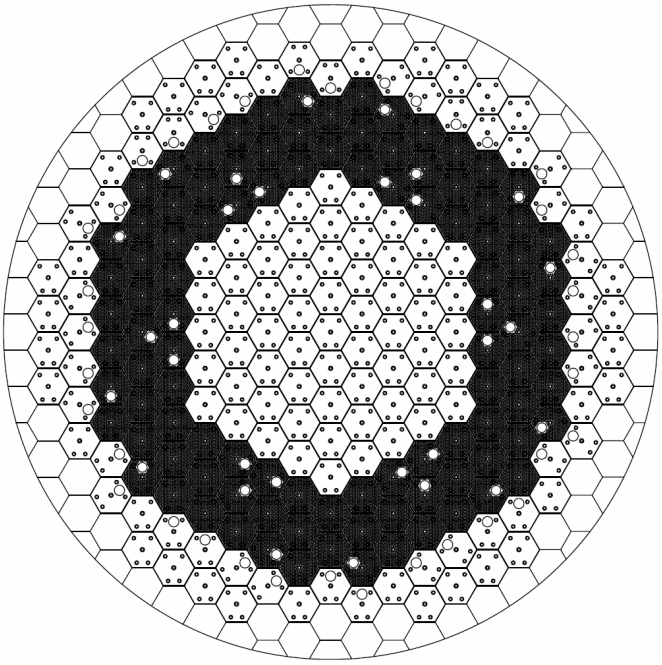

Figure 2.2: Core arrangement for Modular Helium Reactor (MHR) of General Atomics

In this chapter the requirements for core fluids modeling of PMRs are specified and discussed, the corresponding mathematical model is developed, and validation cases are presented. In Section 2.2, the code requirements are specified along with a discussion of why these requirements were chosen, and the overall plan to meet these requirements. The mathematical model is developed in Section 2.3 and consists of the continuous field equations, their discretization, and the associated constitutive equations required to close the model. The validation cases are provided in Section 2.5.

2.2 Code Requirements for the Fluids Model in AGREE

After reviewing the necessary physics required for PMR core fluids modeling, a set of code requirements has been established for the fluid flow module. The key requirements are: calculation of core bypass flow, capturing the momentum flux term in the momentum equation, and the ability to handle flow reversals.

A Phenomena Identification and Ranking Table (PIRT) process has been completed for the NGNP [48]. The accident and thermal fluids PIRT panel has identified core coolant bypass flow as having an importance rank of high with a corresponding knowledge level of low. In the case of the PMR with the inter-block gaps, radial and axial manufacturing

and refueling tolerances for the graphite blocks, irradiation swelling and cracking and the distribution of the thermal expansion, past experience and expertise indicates that the core bypass flow could be a significant proportion of the total core flow [52]. The bypass flow paths are located in the in-core and ex-core vertical columns between the stacks of hexagonal graphite blocks and through control rod holes within the graphite blocks, see Fig. 2.3 and Fig. 2.4. Additionally, the coolant can pass between the primary coolant flow path and the bypass flow path through horizontal gaps formed between the stacked graphite blocks. Therefore, the core fluid flow is essentially three-dimensional.

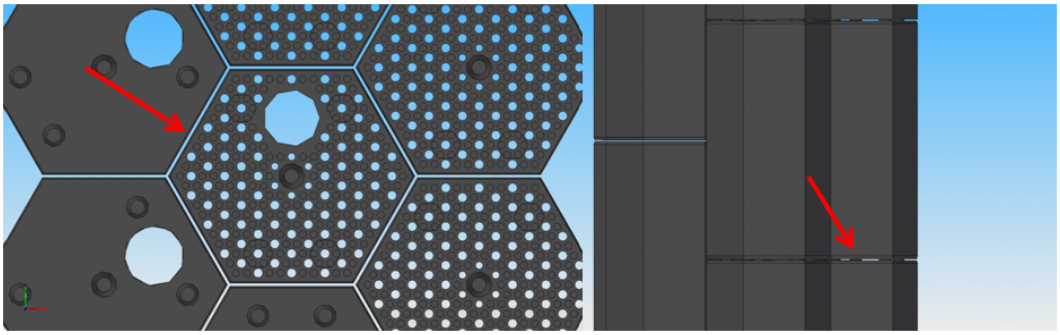

Figure 2.3: Location of bypass flowpaths in the NGNP

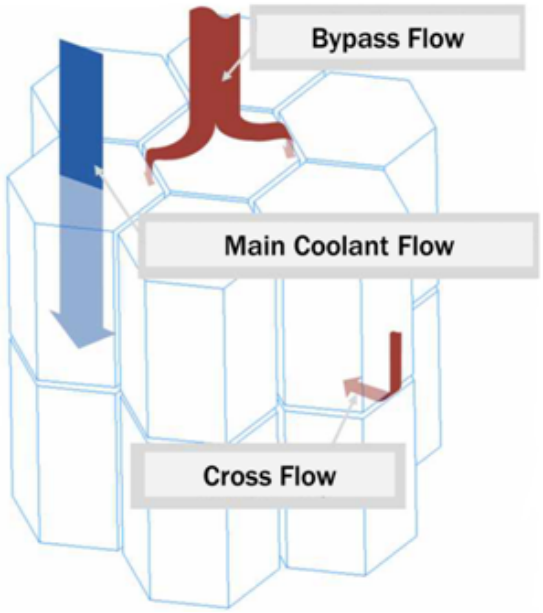

Figure 2.4: Bypass and crossflow paths in the NGNP

A large temperature change occurs over the PMR core. For a GT-MHR, Helium enters the core at $490^{\circ}C$ and exits at $850^{\circ}C$ [53]. This large temperature increase results in a significant reduction in the Helium density with a corresponding fluid acceleration and pressure drop. To capture this effect, the momentum flux terms need to be retained in the momentum equation. In addition, the momentum flux terms are significant for any accident scenario involving depressurization.

2.2.1 A Review of Existing Modeling Methods

Several approaches to modeling fluid flow though the core of a PMR have been utilized that range from flow networks to full 3D CFD simulation. Flow network codes such as FLOPSY [54] and GAS-NET [55], shown in Fig 2.5, have been used by General Atomics and others to determine the flow distribution in the PMR core. These flow network codes are zero-dimensional in the sense that the convective terms are neglected and the solution represents a balance between pressure and friction forces. Neglecting the convective terms makes the solution computationally inexpensive, but these terms can be significant, especially during a transient (e.g. pressure wave propagation, flow-reversal, etc.).

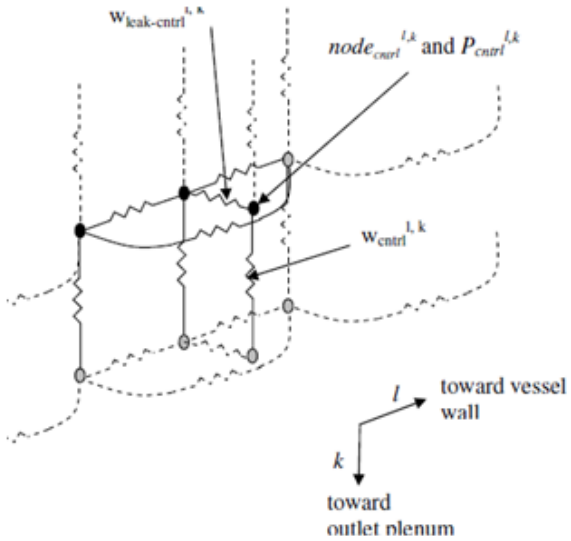

Figure 2.5: Representative computational domain in GAS-NET (figure taken from ANL-GenIV-071 [52])

Another approach is to use existing 1D system codes such as RELAP, TRACE, etc. (e.g. RELAP5 has been utilized to study leakage flows through the PMR core [56] where the cross-flows are modeled as the result of algebraic pressure drop balances). 1D system

codes have the benefit of a very flexible input structure and a history of successful use for the analysis of light water reactors. These analyses typically utilize a nodalization that is quite coarse, see Fig. 2.6. Implementation of 1D system codes for PMR analyses may require substantial modification to implement the necessary physics and correlations, and concern remains in regards to 3D flow modeling. Finally, literature is available that demonstrates 3D CFD modeling of the PMR [57, 58]. CFD provides high fidelity solutions and has been coupled with neutron transport codes [58]. The primary drawback to CFD analysis is the large computational expense associated with the relatively finely meshed computational domain. This large computational expense is amplified by the length of the transients that need to be performed for the PMR (i.e. peak kernel temperature for the DLOFC occurs days into the event). As a compromise between the 1D system codes and CFD, a subchannel approach has been selected as the basis to model PMR fluids in AGREE.

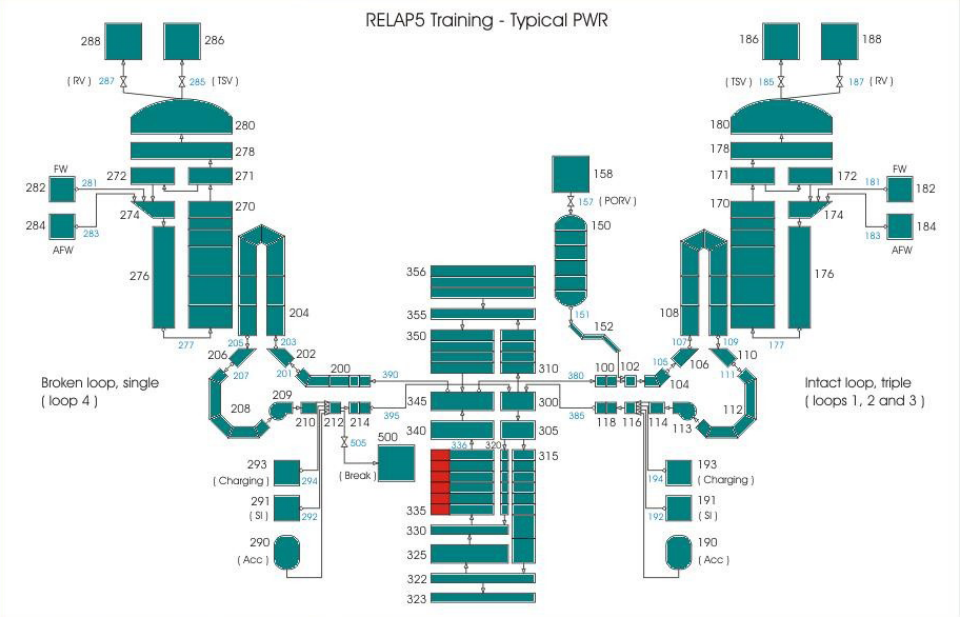

Figure 2.6: Typical nodalization used in a RELAP5 analysis for a pressurized water reactor.

2.2.2 The Subchannel Approach

The subchannel approach divides the entire core into several subchannels, where each subchannel is representative of the flow in that specified region of the core. Each subchannel consists of several smaller volumes stacked axially upon each other. These subchannels

can be connected to other subchannels in juxtaposition by specifying gaps. Gaps consist of several junctions that provide a flowpath between adjacent subchannels.

Calculating the axial momentum flux terms allows the code to capture the pressure and velocity changes that occur when flow acceleration is significant. This local acceleration can occur by area changes in the flowpath as well as expansion of the coolant due to heat transfer. Inclusion of the momentum flux terms results in non-linear partial differential equations which will be handled in the mathematical model.

The normal flow path of the coolant through the core is from the top of the core to the bottom of the core. In the Loss of Forced Circulation (LOFC) accident scenario natural circulation is anticipated to occur during the transient, where the coolant flows from the bottom of the core to the top of the core. Hence, during the LOFC event the coolant flow through the core will initially be relatively large in the normal direction, slow down to stagnation and then change direction. In order for the code to capture this change in flow direction, a hybrid differencing scheme will be used in the axial dimension. The hybrid differencing scheme is a combination of upwind differencing with zero diffusion and central differencing [45].

The application of the subchannel approach to AGREE produces a three-dimensional core represented by a series of cross-connected one-dimensional subchannels. As a visualization aid, a cluster of six graphite-elements is shown in Fig. 2.7 and Fig. 2.8, where each graphite-element is broken up into six individual subchannels and each bypass flowpath is represented as an individual subchannel.

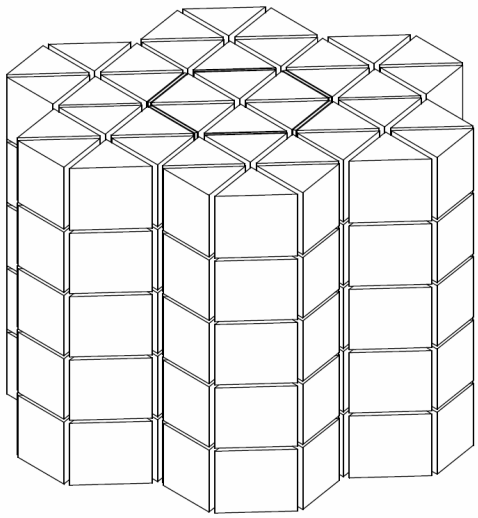

Figure 2.7: Representative computational domain used in the subchannel approach.

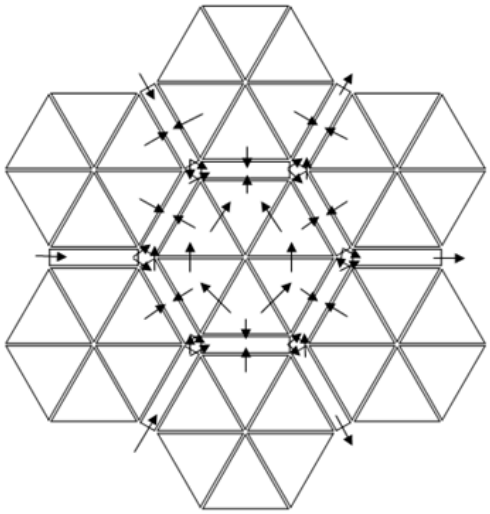

Figure 2.8: Top view of computational domain with emphasis on lateral-flow junctions (gaps).

The velocity field is broken up into axial and lateral components. The axial component corresponds to the fluid flowing vertically through the core and utilizes a general momentum transport equation. The lateral component of momentum is aligned normal to the axial component, and an assumption is imposed that the lateral component of fluid flow is only significant near the lateral faces. Hence, the lateral flux terms are assumed to be negligible. The assumption imposed on the lateral momentum equation has its origins in the subchannel codes used successfully for Light Water Reactor (LWR) core thermal-hydraulic analysis, namely the COBRA [59] and VIPRE [60] codes. This assumption greatly simplifies the governing equations by reducing a fully-three-dimensional system to a network of 1-D subchannels and has been applied successfully for LWR analysis where the axial component of the flow is significantly larger than the lateral component of the flow.

2.2.3 Treatment at Block Interfaces

The portrayal of lateral flow junctions shown in Fig. 2.8 demonstrates the radial locations of the junctions, but the axial locations of the junctions depend on what is being connected. The lateral junctions that connect bypass channels to adjacent bypass channels are placed at the lateral faces of the control volumes since these gaps are open along the entire length of the graphite block, and therefore do not impose any additional modelling concerns. Crossflow to or from the main coolant occurs at block faces, and therefore occurs at an axial face of a control volume and requires special treatment. Instead of placing a lateral

junction at the top or bottom control volume within a graphite block, zero-volume nodes are placed between axially aligned components as shown in Fig. 2.9 and Fig. 2.10.

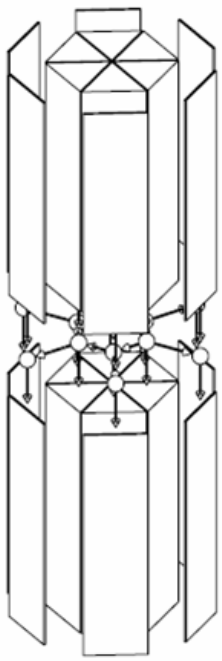

Figure 2.9: Illustration of axial components connected through zero-volume nodes.

2.3 Mathematical Model

Development of the mathematical model occurs in three stages: derivation of the general integral transport equation, application of the integral transport equation to obtain the appropriate balance equations, and discretization of the balance equations to obtain a form amenable to a linear solver. In the paragraph below, a precaution is given to the reader regarding the additional complexity added by the introduction of single-volumes and single-junctions into the model.

The computational domain of the mathematical model is represented by subchannels, single-volumes, and single-junctions. A subchannel consists of user specified n volumes with $n-1$ internal junctions. Therefore, the internal volumes inside of a subchannel have one inlet junction and one outlet junction, but the first and last volume inside of a subchannel can have an arbitrary number of inlet/outlet single-junctions. Likewise a single-volume can have an arbitrary number of inlet/outlet single-junctions. Hence, the introduction of

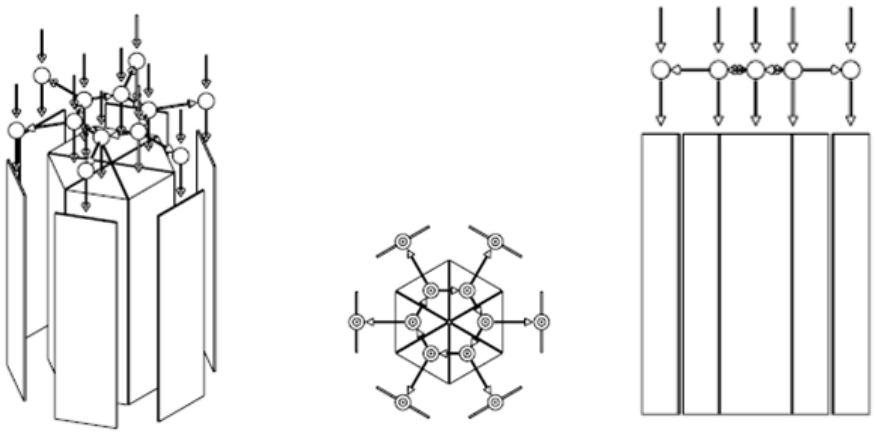

Isometric View Top View Front View

Figure 2.10: Lateral junctions connecting zero volume nodes for crossflow between coolant channels and between coolant channel and bypass channel.

single-junctions affects the convective term in the balance equations. During the conceptual development of AGREE, this added complexity was dealt with by deriving the appropriate discretizations for each situation that could be encountered [61]. After running actual test cases, it was found that the situations where these complexities arise are always associated with abrupt area changes and required special treatment. This special treatment is discussed in Section 2.3.2

2.3.1 The Field Equations

The field equations are obtained by applying the a generalized integral transport equation to the mass, axial momentum, and energy. The lateral momentum equation is obtained via a local instantaneous force balance. The procedure to obtain the general integral transport equation is widely available in the literature, and the procedure applied here is taken from Ishii [62]. A general integral balance is obtained by introducing the density ρ, the efflux $\mathbb{J}$, and the volumetric source S_ϕ for any variable ϕ.

$$\frac{d}{dt}\int_{CV}\rho\phi dV = -\oint_{CS}\vec{n}\cdot\mathbb{J}dA + \int_{CV}S_\phi dV \tag{2.1}$$

Application of the fundamental theorem of calculus to the time derivative results in the following:

$$\frac{d}{dt}\int_{CV}\rho\phi dV = \frac{\partial}{\partial t}\int_{CV}\rho\phi dV + \oint_{CS}\rho\phi\vec{U}\cdot\vec{n}dA \tag{2.2}$$

Combining these results, we obtain the general integral transport equation:

$$\frac{\partial}{\partial t}\int_{CV}\rho\phi dV+\oint_{CS}\rho\phi\vec{U}\cdot\vec{n}dA=-\oint_{CS}\vec{n}\cdot\mathbb{J}dA+\int_{CV}S_{\phi}dV \tag{2.3}$$

The integral transport equation can be reduced further to obtain the differential form of the transport equations. Since the code utilizes finite volumes, further reduction of the equations is unnecessary.

Next, we apply the integral transport equation to a control volume, shown in Fig. 2.11, and carry out integrations over space and time. Integrating Eq. 2.3 over time:

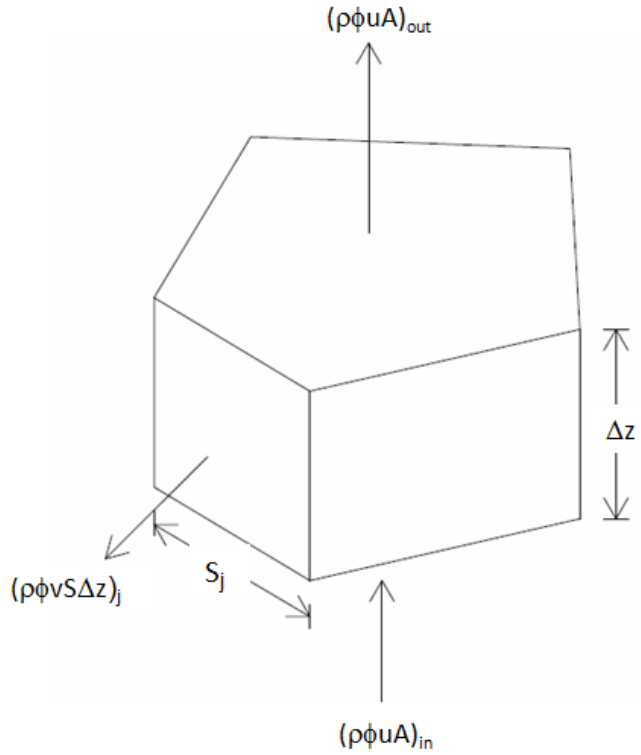

Figure 2.11: Representative control volume (shape is arbitrary)

$$\begin{aligned}\int_{CV}\int_{t}^{t+\Delta t}\frac{\partial\rho\phi}{\partial t}dtdV+\int_{t}^{t+\Delta t}\oint_{CS}\rho\phi\vec{U}\cdot\vec{n}dAdt = &-\int_{t}^{t+\Delta t}\oint_{CS}\vec{n}\cdot\mathbb{J}dAdt\\ &+\int_{t}^{t+\Delta t}\int_{CV}S_{\phi}dVdt\end{aligned} \tag{2.4}$$

For the representation of the term $\partial\rho\phi/\partial t$, a single value for $\rho\phi$ is assumed to prevail through the control volume.

$$\int_{CV}\int_{t}^{t+\Delta t}\frac{\partial \rho\phi}{\partial t}dtdV = A\Delta z\left[(\rho\phi)-(\rho\phi)^{0}\right] \tag{2.5}$$

$$\int_{t}^{t+\Delta t}\oint_{CS}\rho\phi\vec{U}\cdot\vec{n}dAdt = \Delta t\left[(\rho\phi uA)_{out}-(\rho\phi uA)_{in}+\sum_{j}(\rho\phi vS\Delta z)_{j}\right] \tag{2.6}$$

$$\int_{t}^{t+\Delta t}\oint_{CS}\vec{n}\cdot\mathbb{J}dAdt = \Delta t J_{out}A_{CS} \tag{2.7}$$

$$\int_{t}^{t+\Delta t}\int_{CV}S_{\phi}dVdt = A\Delta z\Delta t S_{\phi} \tag{2.8}$$

Combining Eq. 2.5 through Eq. 2.8:

$$\begin{aligned}\frac{A\Delta z}{\Delta t}(\rho\phi)+(\rho\phi uA)_{out} &- (\rho\phi uA)_{in}+\sum_{j}(\rho\phi vS\Delta z)_{j}\\ &= J_{out}A_{CS}+A\Delta zS_{\phi}+\frac{A\Delta z}{\Delta t}(\rho\phi)^{0}\end{aligned} \tag{2.9}$$

2.3.1.1 Conservation of Mass

Since there are no surface or volume sources of mass with respect to a fixed control mass, the efflux and volumetric source terms are zero.

$$\phi = 1, \quad J = 0, \quad S_{\phi} = 0$$

Hence, from Eq. 2.9 the continuity equation can be written as:

$$\frac{A\Delta z}{\Delta t}\rho+(\rho uA)_{out}-(\rho uA)_{in}+\sum_{j}(\rho vS\Delta z)_{j} = \frac{A\Delta z}{\Delta t}\rho^{0} \tag{2.10}$$

Eq. 2.10 is easily extended to a volume with multiple inlet/outlet junctions, see Eq. 2.11.

$$\frac{A\Delta z}{\Delta t}\rho+\sum_{out}(\rho uA)_{out}-\sum_{in}(\rho uA)_{in}+\sum_{j}(\rho vS\Delta z)_{j} = \frac{A\Delta z}{\Delta t}\rho^{0} \tag{2.11}$$

2.3.1.2 Conservation of Energy

An energy balance in term of enthalpy captures the work performed by the fluid across the boundaries of the control volume. The enthalpy transport equation is obtained by introducing the heat efflux and source terms into Eq. 2.9.

$$\phi = h, \quad J_{out}A_{CS} = -q''_{in}\xi_{H}\Delta z-\left(kA\frac{\partial T}{\partial z}\right)_{out}+\left(kA\frac{\partial T}{\partial z}\right)_{in}, \quad S_{\phi} = q'''A\Delta z$$

In the terms above, the viscous dissipation and the substantial derivative of pressure have been dropped as they have negligible contributions to the energy balance. The resulting enthalpy transport equation is given in Eq. 2.12.

$$\begin{aligned}\frac{A\Delta z}{\Delta t}(\rho h) &+ (\rho huA)_{out} - (\rho huA)_{in} + \sum_j (\rho hvS\Delta z)_j \\ &= q''_{in}\xi_H \Delta z + \left(kA\frac{\partial T}{\partial z}\right)_{out} - \left(kA\frac{\partial T}{\partial z}\right)_{in} + \frac{A\Delta z}{\Delta t}(\rho h)^0 \end{aligned} \tag{2.12}$$

Eq. 2.12 is easily extended to a volume with multiple inlet/outlet junctions, see Eq. 2.13.

$$\begin{aligned}\frac{A\Delta z}{\Delta t}(\rho h) &+ \sum_{out}(\rho huA)_{out} - \sum_{in}(\rho huA)_{in} + \sum_j (\rho hvS\Delta z)_j \\ &= q''_{in}\xi_H \Delta z + \sum_{out}\left(kA\frac{\partial T}{\partial z}\right)_{out} - \sum_{in}\left(kA\frac{\partial T}{\partial z}\right)_{in} \\ &+ \frac{A\Delta z}{\Delta t}(\rho h)^0 \end{aligned} \tag{2.13}$$

2.3.1.3 Conservation of Axial Momentum

The axial momentum equation is obtained by introducing the surface and body forces. Additionally, the axial momentum equations are solved at the faced of the control volume. Thus the pressures utilized in the axial momentum equation are taken at the centers of the adjacent control volumes. The efflux and source terms are given below.

$$\phi = u, \quad J_{out}A_{CS} = (p_{out} - p_{in})A + \left(K + \tfrac{fl}{D_H}\right)\left(\rho\tfrac{|u|u}{2}A\right), \quad S_\phi = (\rho A\Delta z)\cos\theta$$

Placing the terms above into Eq. 2.9:

$$\begin{aligned}\frac{A\Delta z}{\Delta t}(\rho u) &+ (\rho u^2 A)_{out} - (\rho u^2 A)_{in} \\ &= (p_{in} - p_{ou})A - \left(K + \frac{fl}{D_H}\right)\left(\rho\frac{|u|u}{2}A\right) \\ &+ (\rho A\Delta z)\cos\theta + \frac{A\Delta z}{\Delta t}(\rho u)^0 \end{aligned} \tag{2.14}$$

2.3.1.4 Conservation of Lateral Momentum

The lateral momentum equations are obtained by performing a localized instantaneous force balance on the lateral flow junctions. In the resulting equation, Eq. 2.15, the temporal and momentum flux terms drop out.

$$K\rho\frac{|v|v}{2} = p_{in} - p_{out} \tag{2.15}$$

2.3.2 Discretization of the Field Equations

In this section the transport equations are placed in a form amenable to a linear solver. The equations to be solved will be the energy equation, linear momentum equation, lateral momentum equation, and pressure correction equation. Although it may appear that the conservation of mass equation is not present, it will be shown to be present in the form of the pressure correction equation. Additionally, in the previous sections the flow across a boundary was specified as either *in* or *out* for simplicity. This simplified nomenclature will be insufficient in this section because different quantities are stored at different locations within the computational domain, i.e. fluid properties are stored at the centers of the control volumes, whereas the velocities are stored at the faces of the control volumes (junctions/gaps). Therefore, *in* and *out* will be replaced by iv, ov, ij, and oj for inlet volume, outlet volume, inlet junction, and outlet junction respectively.

2.3.2.1 Useful Quantities

From the previous paragraph, fluid properties are stored at the control volume centers and the velocities are stored at the faces of the control volumes in junctions and gaps. However, there are quantities that are required for nearly all the transport equations and need to be extrapolated. The calculation of density at the junctions and the mass flow at the volume center are useful quantities and are calculated below.

Junction density is obtained by linear interpolation:

$$\rho_{ij} = \frac{\rho\Delta z_{iv} + \rho_{iv}\Delta z}{(\Delta z + \Delta z_{iv})} \tag{2.16}$$

$$\rho_{oj} = \frac{\rho\Delta z_{ov} + \rho_{ov}\Delta z}{(\Delta z + \Delta z_{ov})} \tag{2.17}$$

The mass flow rate calculated at the volume center utilizes the above definition given by Eq. 2.18.

$$F = \frac{\rho}{2}\Big(\sum_{m}(uA)_{oj} + \sum_{n}(uA)_{ij}\Big) \tag{2.18}$$

2.3.2.2 Conservation of Energy

The conservation of energy equation is given by Eq. 2.12. To place this equation into an algebraic form, the differentials need to be approximated.

$$\sum_{out} kA\frac{\partial T}{\partial z} = \sum_{oj} 2k_{oj}A_{oj}\frac{T_{ov} - T}{\Delta z + \Delta z_{ov}} \tag{2.19}$$

The equation above leads to the following definitions to simplify the expressions.

$$D_{h,oj} = \frac{2k_{oj}A_{oj}}{\Delta z + \Delta z_{ov}} \tag{2.20}$$

$$D_{h,ij} = \frac{2k_{ij}A_{ij}}{\Delta z + \Delta z_{iv}} \tag{2.21}$$

Next, an approximation needs to be imposed for the enthalpy values that are convected though the faces. As a first approximation, and to aid in the development of the equations, the central differencing scheme will be applied.

$$h_{oj} = \frac{c_p T\Delta z + (c_p T\Delta z)_{ov}}{\Delta z + \Delta z_{ov}} \tag{2.22}$$

$$h_{ij} = \frac{c_p T\Delta z + (c_p T\Delta z)_{iv}}{\Delta z + \Delta z_{iv}} \tag{2.23}$$

Then, the convective terms become the following:

$$\begin{aligned}\sum_{out}(\rho huA) &= \sum_{oj}\Big[(\rho uA)_{oj}\frac{\Delta z}{\Delta z + \Delta z_{ov}}c_p T\Big] \\ &+ \sum_{oj}\Big[(\rho uA)_{oj}\frac{\Delta z}{\Delta z + \Delta z_{ov}}(c_p T)_{ov}\Big]\end{aligned} \tag{2.24}$$

Eq. 2.24 leads to the following definitions to simplify the expressions.

$$F_{oj} = (\rho uA)_{oj} \tag{2.25}$$

$$F_{ij} = (\rho uA)_{ij} \tag{2.26}$$

Using Eq. 2.19 through Eq. 2.26, conservation of of energy, Eq. 2.13, can be written in the discretized form of Eq. 2.27.

$$\begin{aligned}\Big[\frac{\rho A\Delta z}{\Delta t} &+ \sum_{oj}\Big(D_{h,oj}+F_{oj}\frac{\Delta z}{\Delta z+\Delta z_{ov}}\Big)+\sum_{ij}\Big(D_{h,ij}-F_{ij}\frac{\Delta z}{\Delta z+\Delta z_{ov}}\Big)\Big]c_pT \\ &= \sum_{oj}\Big(D_{h,oj}-F_{oj}\frac{\Delta z}{\Delta z+\Delta z_{ov}}\Big)c_pT_{ov} \\ &+ \sum_{ij}\Big(D_{h,ij}+F_{ij}\frac{\Delta z}{\Delta z+\Delta z_{iv}}\Big)c_pT_{iv} \\ &+ q''\xi_H\Delta z-\sum_j(\rho c_pTvS\Delta z)_j+\frac{\rho A\Delta z}{\Delta t}(c_pT)^0 \end{aligned} \tag{2.27}$$

For implementation, conservation of energy is expressed as Eq.2.28.

$$a_TT=\sum_{ov}a_{T,ov}T_{ov}+\sum_{iv}a_{T,iv}T_{iv}+b_T \tag{2.28}$$

with,

$$a_{T,ov}=\Big(D_{h,oj}-F_{oj}\frac{\Delta z}{\Delta z+\Delta z_{ov}}\Big)c_{p,ov}$$

$$a_{T,iv}=\Big(D_{h,ij}+F_{ij}\frac{\Delta z}{\Delta z+\Delta z_{iv}}\Big)c_{p,iv}$$

$$a_T=\Big[\frac{\rho A\Delta x}{\Delta t}+\sum_{ov}\Big(\frac{a_{T,ov}}{c_{p,ov}}+F_{oj}\Big)+\sum_{iv}\Big(\frac{a_{T,iv}}{c_{p,iv}}-F_{ij}\Big)\Big]c_p$$

$$b_T=q''\xi_H\Delta z-\sum_j(\rho c_pTvS\Delta z)_j+\frac{\rho A\Delta z}{\Delta t}(c_pT)^0 \tag{2.29}$$

It must be stated again that the above discretization is for central differencing, and has one large drawback. Namely, central differencing can become unstable for large flow rates. This can be seen by understanding that all coefficients, given by Eq. 2.29, must be positive to ensure numerical stability. For this condition to be satisfied, the following criterion must be satisfied for central differencing to be stable.

$$Pe_{oj}<\frac{\Delta z+\Delta z_{ov}}{\Delta z_{ov}} \tag{2.30}$$

Where $Pe_{oj}=F_{oj}/D_{oj}$ is the volume Peclet number and represents the relative ratio of convection to diffusion. As most of the flows this code is being design to analyse are

strongly convective, the fine mesh size required to achieve stability with central differencing is not acceptable. A better approach is to use hybrid differencing, which is a combination of central differencing and zero diffusion upwind differencing [45]. The application of hybrid differencing at this stage is a simple matter. Eq. 2.28 remains unchanged. Only the coefficients in Eq. 2.29 need to be updated to reflect the hybrid differencing scheme as shown below.

$$a_{T,ov} = \max\left\{0, D_{h,oj} - F_{oj}\frac{\Delta z}{\Delta z + \Delta z_{ov}}, -F_{oj}\right\}$$

$$a_{T,iv} = \max\left\{F_{ij}, D_{h,ij} + F_{ij}\frac{\Delta z}{\Delta z + \Delta z_{ov}}, 0\right\} c_{p,iv}$$

$$a_T = \left[\frac{\rho A \Delta x}{\Delta t} + \sum_{ov}\left(\frac{a_{T,ov}}{c_{p,ov}} + F_{oj}\right) + \sum_{iv}\left(\frac{a_{T,iv}}{c_{p,iv}} - F_{ij}\right)\right] c_p$$

$$b_T = q'' \xi_H \Delta z - \sum_j (\rho c_p T v S \Delta z)_j + \frac{\rho A \Delta z}{\Delta t}(c_p T)^0 \tag{2.31}$$

2.3.2.3 Conservation of Axial Momentum

Treatment of the axial momentum equations follows the same approach as the energy equation, but there is a notable difference. There is no axial diffusion term so central differencing is unconditionally unstable for axial momentum. Thus, equations are derived for upwind differencing.

The conservation of axial momentum equation for a typical junction is given by Eq. 2.14. The algebraic approximation of this equation for flow in the normal direction is given by Eq. 2.32.

$$\begin{aligned}\left[\frac{\rho A \Delta z}{\Delta t}\right. &+ \left. F_{ov} + \left(K + \frac{fl}{D_H}\right)\left(\rho \frac{|u|}{2} A\right)\right] u \\ &= F_{iv} u_{ij} + (p_{iv} - p_{ov}) A + \rho A \Delta z g \cos\theta + \frac{\rho A \Delta z}{\Delta t} u^0 \end{aligned} \tag{2.32}$$

The algebraic approximation of Eq. 2.14 for flow in the reverse direction is given by Eq. 2.33.

$$\left[\frac{\rho A\Delta z}{\Delta t} - F_{iv} + \left(K + \frac{fl}{D_H}\right)\left(\rho\frac{|u|}{2}A\right)\right]u$$
$$= -F_{ov}u_{oj} + (p_{iv} - p_{ov})A + \rho A\Delta z g\cos\theta + \frac{\rho A\Delta z}{\Delta t}u^0 \quad (2.33)$$

Eq. 2.32 and Eq. 2.33 can be combined into a generalized upwind expression given by Eq. 2.34.

$$a_u u = a_{u,oj}u_{oj} + a_{u,ij}u_{ij} + (p_{iv} - p_{ov})A + b_u \quad (2.34)$$

with,

$$a_{u,oj} = \max\left\{0, -F_{ov}\right\}$$

$$a_{u,ij} = \max\left\{F_{iv}, 0\right\}$$

$$a_u = \frac{\rho A\Delta z}{\Delta t} + a_{u,oj} + a_{u,ij} + (F_{ov} - F_{iv}) + \left(K + \frac{fl}{D_H}\right)\left(\rho\frac{|u|}{2}A\right)$$

$$b_u = \rho A\Delta z g\cos\theta + \frac{\rho A\Delta z}{\Delta t}u^0 \quad (2.35)$$

2.3.2.4 Special Models

In modeling the actual reactor core, several abrupt area changes occur at the core inlet and outlet. Standard upwind differencing cannot capture this behavior with fidelity. To deal with this behavior a branching type of junction is utilized to handle abrupt area changes. Such an approach is taken in RELAP5 [63], and is utilized in AGREE for treatment at abrupt area changes and at the inlet/outlet of the core.

Abrupt Area Change

The special treatment is for a generalized contraction, consisting of multiple upstream junctions, shown in Fig. 2.12, requires the definition of an effective upwind area. The effective upwind area of the junction is calculated as shown in Eq. 2.36 , where W is the mass flow rate:

$$A_{eff} = \max\left\{A_{ov}, \left|\frac{W_j}{W_{iv}}\right|A_{iv}\right\} \quad (2.36)$$

Figure 2.12: Visualization of a generalized contraction/expansion in AGREE

Using the definition for A_{eff}, the discretization for the junction is derived from a mechanical energy balance:

$$(p+\frac{1}{2}\rho u^2)_{iv} = (p+\frac{1}{2}\rho u^2)_{ov} \tag{2.37}$$

Treating the fluid as incompressible, continuity gives Eq. 2.38, where $\varepsilon = \frac{A_{ov}}{A_{eff}}$

$$u_{iv} = u_{ov}\varepsilon \tag{2.38}$$

rearranging,

$$p_{iv} - p_{ov} = \frac{1}{2}(1-\varepsilon^2)\rho u_{ov}^2 \tag{2.39}$$

Introducing the additional loss and source terms, we arrive at the discretized equation given by Eq. 2.40.

$$a_u u = (p_{iv} - p_{ov})A + b_u \tag{2.40}$$

with,

$$a_u = \frac{1}{2}(1-\varepsilon^2)W + \left(K + \frac{fl}{D_H}\right)\left(\rho\frac{|u|}{2}A\right)$$

$$b_u = \rho A \Delta z g \cos\theta \tag{2.41}$$

The development for a generalized expansion is completely analogous. Furthermore, the equations derived for the generalized contraction exactly reproduce the result for a generalized expansion when the flow is revered, which is demonstrated in the verification tests.

Crossflow with/without Abrupt Area Change

At block interfaces, the possibility of an abrupt area change with cross flow can occur. This section demonstrates that upwind differencing captures the Borda-Carnot loss coefficient [64]. A standard crossflow junction without any area changes is depicted in Fig. 2.13.

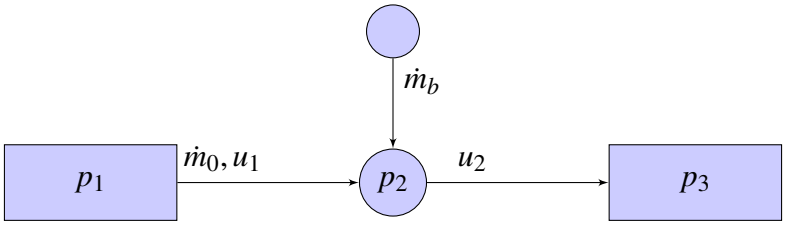

Figure 2.13: Diagrm of crossflow

Applying the impulse momentum equation on junction 1 and ignoring any friction losses one arrives at Eq. 2.46:

$$\oint_1 \rho u(\vec{u} \cdot \vec{dA} = (p_1 - p_2)A \tag{2.42}$$

$$F_{out} = \frac{1}{2}(u_1 + u_2)\rho A = \dot{m}_0 + \frac{1}{2}\dot{m}_b \tag{2.43}$$

$$F_{in} = \dot{m}_0 \tag{2.44}$$

$$\left(\dot{m}_0 + \frac{1}{2}\dot{m}_b\right)u_1 - \dot{m}_0 u_1 = (p_1 - p_2)A \tag{2.45}$$

$$p_1 - p_2 = \frac{1}{\rho A^2}\left(\frac{1}{2}\dot{m}_0\dot{m}_b\right) \tag{2.46}$$

Repeat the process for junction 2 and combine the results for overall Δp:

$$F_{out} = \dot{m}_0 + \dot{m}_b \tag{2.47}$$

$$F_{in} = \dot{m}_0 + \frac{1}{2}\dot{m}_b \tag{2.48}$$

$$p_2 - p_3 = \frac{1}{\rho A^2}\left(\frac{3}{2}\dot{m}_0\dot{m}_b + \dot{m}_b^2\right) \tag{2.49}$$

$$\Delta p = \frac{1}{\rho A^2}(2\dot{m}_0\dot{m}_b + \dot{m}_b^2) \tag{2.50}$$

Eq. 2.50 is the analytic solution for crossflow at a T-junction. Next, introduce an expansion as depicted in Fig. 2.14 and repeat the process. Note that in this argument, the areas are provided at the volume centers and the velocities are located at the junctions.

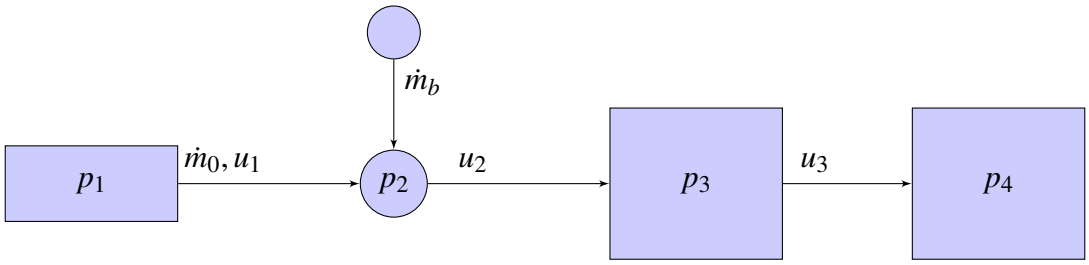

Figure 2.14: Diagrm of crossflow with expansion

The situation for junction 1 is exactly the same, so Eq. 2.46 still holds, but the area change affects junction 2. From continuity:

$$u_3 = \frac{A_2}{A_3}u_2 = \varepsilon u_2 \tag{2.51}$$

The manner in which the cell center velocity is interpreted has a large affect on the overall outcome. Chose the cell centered velocity for volume 3 as given below:

$$u_T = \frac{u_2A_2 + u_3A_3}{2A_2} = \frac{1}{2}\varepsilon u_2 + \frac{1}{2}u_3 = \varepsilon u_2 \tag{2.52}$$

$$F_{out} = \rho u_T A_3 = \varepsilon\rho u_2 A_3 = \dot{m}_0 + \dot{m}_b \tag{2.53}$$

The F_{in} term remains the same as in the standard crossflow problem, given by Eq. 2.48, and the pressure drop between volumes 1 and 3 is the same as in the analytic solution for the standard T-junction, given by Eq. 2.50.

Applying impulse momentum on junction 3 and carrying out the algebra we arrive at the additional loss given by Eq. 2.58 and overall pressure drop.

$$F_{out} = F_{in} = \dot{m}_0 + \dot{m}_b \tag{2.54}$$

$$(\dot{m}_0 + \dot{m}_b)(u_3 - u_2) = (p_3 - p_4)A_3 \tag{2.55}$$

$$\frac{-(1-\varepsilon)(\dot{m}_0+\dot{m}_b)^2}{\rho A_2} = (p_3-p_4)\frac{A_2}{\varepsilon} \tag{2.56}$$

$$p_3-p_4 = \frac{1}{\rho A_2^2}\left[-(\varepsilon-\varepsilon^2)(\dot{m}_0+\dot{m}_b)^2\right] \tag{2.57}$$

$$p_3-p_4 = \frac{1}{\rho A_2^2}\left[-(\varepsilon-\varepsilon^2)(\dot{m}_0+\dot{m}_b)^2\right] \tag{2.58}$$

$$\Delta p = \frac{1}{\rho A_2^2}\left[2\dot{m}_0\dot{m}_b+\dot{m}_b^2-(\varepsilon-\varepsilon^2)(\dot{m}_0+\dot{m}_b)^2\right] \tag{2.59}$$

The last step is to show that the loss obtained by Eq. 2.58 is equivalent to that obtained via the Borda-Carnot loss coefficient. Assume a crossflow followed by an abrupt area change, situation depicted in Fig. 2.15.

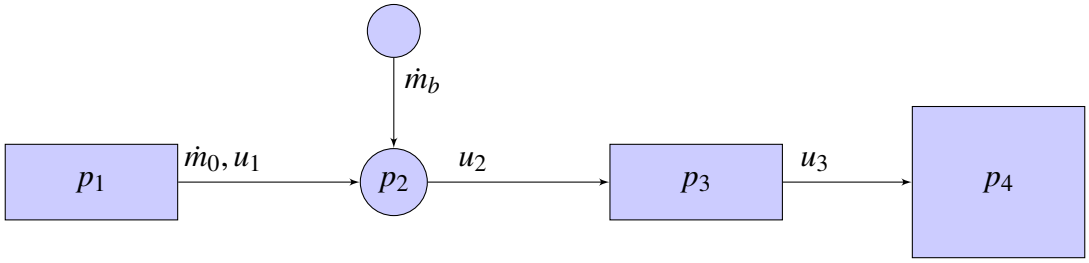

Figure 2.15: Diagrm of crossflow, followed by expansion

From an instantaneous energy balance about junction 3:

$$p_3+\frac{1}{2}\rho u_3^2 = p_4+\frac{1}{2}\rho u_4^2+K\frac{1}{2}\rho u_3^2 \tag{2.60}$$

With $K=(1-\varepsilon)^2$:

$$p_3-p_4 = \frac{1}{2}\rho u_3^2\left[\varepsilon^2-1+(1-\varepsilon)^2\right] \tag{2.61}$$

$$p_3-p_4 = \frac{1}{2\rho A_2^2}(\dot{m}_0+\dot{m}_b)^2(2\varepsilon^2-2\varepsilon) \tag{2.62}$$

Rearranging, one arrives at Eq. 2.58. Thus the standard upwind differencing at crossflow junctions captures the Borda-Carnot loss coefficient. Performing a similar analysis for a sudden contraction yields the same result, upwind differencing will not preserve the mechanical energy of the flow but applies the Borda-Carnot loss coefficient. The Borda-Carnot

loss coefficient, however, is not directly applicable to contractions. Looking at Table 2.1 the differences between the expansion (Borda-Carnot) and contraction loss coefficients is very small when the area ratio is greater than 0.5. Since the area changes between stacked blocks is small, the upwind treatment provides an accurate estimation of the pressure changes.

Table 2.1: Loss coefficients for flow through sudden area changes(data from [64])

A_1/A_2	K_{exp}	K_{cont}
0.0	1.00	0.50
0.1	0.81	0.46
0.2	0.64	0.41
0.3	0.49	0.36
0.4	0.36	0.30
0.5	0.25	0.24
0.6	0.16	0.18
0.7	0.09	0.12
0.8	0.04	0.06
0.9	0.01	0.02
1.0	0.00	0.00

2.3.2.5 Pressure Correction Equation

The pressure correction equation is obtained by introducing the momentum equations into the conservation of mass equation. The addition of special models to handle abrupt area changes and branching components do not impact the form of the pressure correction equation. Therefore a single general pressure correction equation can be obtained which is applied to all volumes within the computational domain. The derivation of the pressure correction equation begins with a generalized conservation of mass equation and conservation of momentum equations.

$$\frac{A\Delta z}{\Delta t}\rho + \sum_{oj}(\rho u A)_{oj} - \sum_{ij}(\rho u A)_{ij} + \sum_{j}(\rho v S\Delta z)_j = \frac{A\Delta z}{\Delta t}\rho^0 \tag{2.63}$$

$$a_u u = \sum_{oj} a_{u,oj}u_{oj} + \sum_{ij} a_{u,ij}u_{ij} + (p_{iv} - p_{ov})A + b_u \tag{2.64}$$

$$a_v v = (p_{iv} - p_{ov})A \tag{2.65}$$

Next, split the pressure and velocities into a guess value and a correction value, as shown below where the starred quantities represent the guessed value.

$$p = p^* + p'$$

$$u = u^* + u'$$

$$v = v^* + v' \tag{2.66}$$

Place the pressure and axial velocity into the axial momentum equation.

$$\begin{aligned} a_u(u^* + u') &= \sum_{oj} a_{u,oj}(u^*_{oj} + u'_{oj}) + \sum_{ij} a_{u,ij}(u^*_{ij} + u'_{ij}) \\ &+ \left[(p^*_{iv} + p'_{iv}) - (p^*_{ov} + p'_{ov})\right]A + b_u \end{aligned} \tag{2.67}$$

The guessed velocity field satisfies the guessed pressure field with the corresponding source. Therefore, the velocity correction equation reduces to Eq. 2.68.

$$a_u u' = \sum_{oj} a_{u,oj} u'_{oj} + \sum_{ij} a_{u,ij} u'_{ij} + (p'_{iv} - p'_{ov})A \tag{2.68}$$

Next, the fundamental simplifying step of the SIMPLE algorithm is performed. The velocity correction terms in the inlet and outlet junctions are dropped.

$$a_u u' = (p'_{iv} - p'_{ov})A \tag{2.69}$$

$$u' = d_u(p'_{iv} - p'_{ov}) \tag{2.70}$$

Similary for the lateral momentum equation

$$v' = d_v(p'_{iv} - p'_{ov}) \tag{2.71}$$

The final step is to expand the conservation of mass equation in terms of the guessed and corrected values, and then replace the velocity correction terms with the pressure correction terms using Eq. 2.70 and Eq. 2.71.

$$\begin{aligned}\frac{A\Delta z}{\Delta t}\rho &+ \sum_{oj}(\rho A)_{oj}(u^*_{oj}+u'_{oj}) - \sum_{ij}(\rho A)_{ij}(u^*_{ij}+u'_{ij}) \\ &+ \sum_{j}(\rho S\Delta z)(v^*_j+v'_j) = \frac{A\Delta z}{\Delta t}\rho^0 \end{aligned} \tag{2.72}$$

$$\begin{aligned}\sum_{oj}(\rho A)_{oj}u'_{oj} &- \sum_{ij}(\rho A)_{ij}u'_{ij} + \sum_{j}(\rho S\Delta z)v'_j \\ &= \frac{(\rho^0-\rho)A\Delta z}{\Delta t} + \sum_{ij}(\rho A)_{ij}u^*_{ij} \\ &- \sum_{oj}(\rho A)_{oj}u^*_{oj} - \sum_{j}(\rho S\Delta z)v^*_j \end{aligned} \tag{2.73}$$

$$\begin{aligned}p'\sum_{oj}(\rho Ad)_{oj} &- \sum_{oj}(\rho Ad)_{oj}p'_{ov} - \sum_{ij}(\rho Ad)_{ij}p'_{iv} + p'\sum_{ij}(\rho Ad)_{ij} \\ &+ p'\sum_{j}(\rho S\Delta z) - \sum_{j}(\rho S\Delta z)p'_{ov} \\ &= \frac{(\rho^0-\rho)A\Delta z}{\Delta t} + \sum_{ij}(\rho A)_{ij}u^*_{ij} \\ &- \sum_{oj}(\rho A)_{oj}u^*_{oj} - \sum_{j}(\rho S\Delta z)v^*_j \end{aligned} \tag{2.74}$$

The pressure correction equation is then simplified to Eq. 2.75

$$a_p p' = \sum_{ov} a_{p,ov}p'_{ov} + \sum_{iv} a_{p,iv}p'_{iv} + \sum_{j} a_{p,j}p'_{ov} + b_p \tag{2.75}$$

with,

$$a_{p,ov} = (\rho Ad)_{oj}$$

$$a_{p,iv} = (\rho Ad)_{ij}$$

$$a_{p,j} = (\rho S\Delta z d)_j$$

$$a_p = \sum_{ov} a_{p,ov} + \sum_{iv} a_{p,iv} + \sum_{j} a_{p,j}$$

$$b_p = \frac{(\rho^0 - \rho)A\Delta z}{\Delta t} + \sum_{ij} (\rho u^* A)_{ij} - \sum_{oj} (\rho u^* A)_{oj} - \sum_{j} (\rho v^* S \Delta z) \tag{2.76}$$

2.3.2.6 Implementation of Boundary Conditions

The user of the code will be capable of specifying fluid mass flow rates and thermodynamic conditions at appropriate locations within the model as a function of time. The ability to specify the mass flow rate is accomplished by using a single-junction and introducing information tables. The single-junction is similar to an individual junction within a subchannel, but the user has the ability to specify the mass flow rate through the junction as a function of time. Mass flow rate through the single-junction is obtained by linearly interpolating data from within the information table. The ability to specify thermodynamic conditions within the model is accomplished by introducing single-volumes and utilizing information tables. The single-volume is similar to an individual volume within a subchannel, but the pressure and temperature within the volume can be specified as a function of time. Pressure and temperature within the single-volume are obtained by linearly interpolating data from within the information table.

2.3.3 Constitutive Equations

2.3.3.1 Fluid Properties

The properties of helium are hardcoded into the code for convenience. In addition, the user has the option of specifying a constant property fluid. Material properties for Helium are obtained using equations from Petersen [65] (also available in KTA 3102.1 [66]). These equations are provided below for completeness and are valid for pressures ranging from 1 bar to 100 bar and from temperatures ranging from 293 K to 1773 K [66].

Density of Helium

$$\rho = 48.14 \frac{p}{T} \left(1 + 0.4446 \frac{p}{T^{1.2}}\right)^{-1} \tag{2.77}$$

with ρ in $\frac{kg}{m^3}$, p in bar, and T in Kelvin. The standard deviation in percent is:

$$\sigma = 0.03\sqrt{p} \tag{2.78}$$

Specific Heat of Helium

As helium is a monatomic gas, the specific heats are constant. The specific heats in $\frac{J}{kg-K}$ is:

$$c_p = 5195 \tag{2.79}$$

$$c_v = 3117 \tag{2.80}$$

The standard deviation in percent for the specific heat is:

$$\sigma = 0.05p^{(0.6-0.1\frac{T}{T_0})} \tag{2.81}$$

with p in bar, T in Kelvin, and $T_0 = 273.16\,K$

Dynamic Viscosity of Helium

$$\mu = 3.674x10^{-7}T^{0.7} \tag{2.82}$$

with μ in $Pa \cdot s$, and T in Kelvin. The standard deviation in percent is:

$$\sigma = 0.0015T \tag{2.83}$$

Thermal Conductivity of Helium

$$k = 2.682x10^{-3}(1 + 1.123x10^{-3}p)T^{0.71(1-2x10^{-4}p)} \tag{2.84}$$

with k in $\frac{W}{m \cdot K}$, p in bar, and T in Kelvin. The standard deviation in percent is:

$$\sigma = 0.0035T \tag{2.85}$$

2.3.3.2 Darcy Friction Factors

Darcy friction factors are utilized to calculate the major head loss in a turbulent flow. These friction factors are obtained using the formula from Churchill [67] provided below. Fig. 2.16 demonstrates the advantage the Churchill formulation has over the iterative Colebrook equation [68]. Churchill captures the Darcy friction factor over all flow regimes, including the laminar to turbulent transition.

$$f = 8\left[\left(\frac{8}{Re}\right)^{12} + \frac{1}{(A+B)^{3/2}}\right]^{1/12} \tag{2.86}$$

$$A = \left[2.457 \ln \frac{1}{\left(\frac{7}{Re}\right)^{0.9} + \frac{0.27\varepsilon}{D}}\right]^{16}$$

$$B = \left(\frac{37530}{Re}\right)^{16}$$

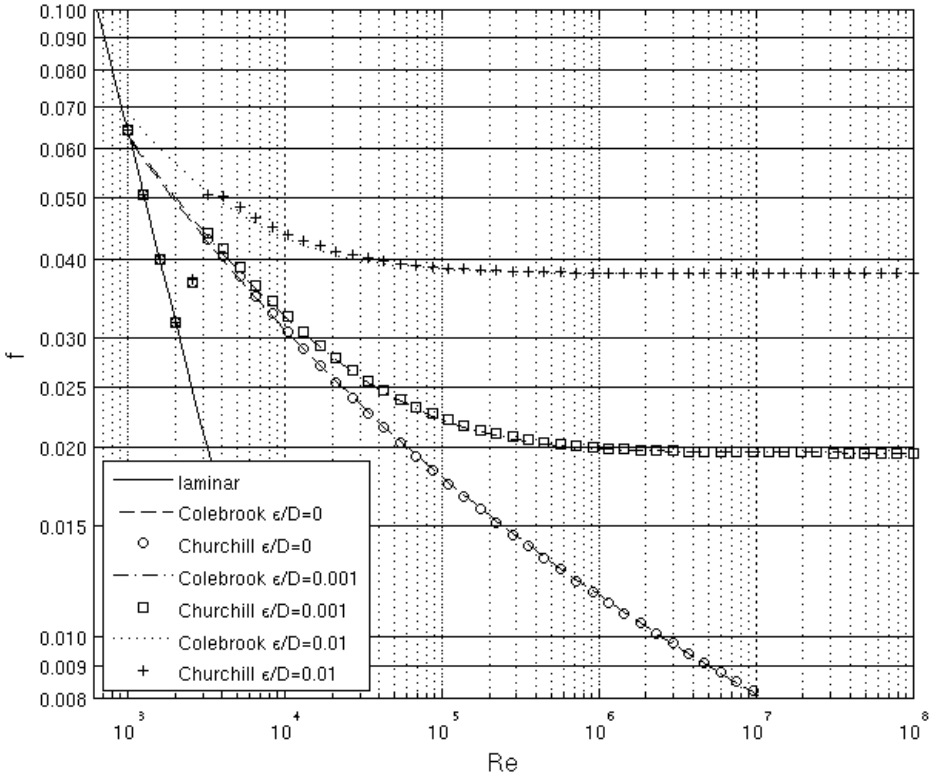

Figure 2.16: Moody friction factor chart obtained using Churchill and Colebrook equations

2.3.3.3 Gap Loss Coefficients

The primary gas loss model utilized in AGREE is the model provided by Kaburaki and Takizuka [69]. Kaburaki and Takizuka performed an experimental study of leakage flows between HTGR fuel blocks, and developed a correlation for the gap loss coefficient which can be manipulated to give the form in Eq. 2.87, where L_{gap} is the flat length of a hex block in meters, δ is the size of the gap in meters, and Re is the Reynolds number of the flow through the gap.

$$K_{gap} = 36L_{gap}^2\left(\frac{0.67}{\delta Re} + 3.13\right) \tag{2.87}$$

2.4 Verificiation Tests

Several verification calculations have been performed and can be grouped into three distinct sections. The first section consists of simple calculations of steady-state incompressible flow in a pipe, where exact analytic solutions exist. The results are compared against a hand calculation to verify the correction implementation of the body and friction forces. The second section consists of solutions for abrupt area changes with and without crossflow. These calculations are compared against hand calculations to verify the correct implementation of the special models. The third section is a multichannel transient of a flow reversal and is qualitative in nature. The results of the calculation are observed to verify that the transient solver produces results in physical behavior that is qualitatively correct.

2.4.1 1-D Pipe

A 1-D pipe problem is fabricated with the parameters given in Table 2.2, which result in a calculated Reynolds number of $Re = 10^7$, and an associated Darcy friction factor of $f = 0.00815$ for a smooth pipe. The resulting pressure profiles, shown in Fig. 2.17, are in agreement with the exact solution.

Table 2.2: 1-D pipe verification problem parameters

ρ	$1000\,\frac{kg}{m^3}$
u	$2\,m/s$
μ	$1.0x10^{-5}\,\frac{kg}{m \cdot s}$
p_{out}	$101.3\,kPa$
Length	$1\,m$
Diameter	$5\,cm$

2.4.2 Abrupt Area Change and Crossflow

The fabricated 1-D pipe problem is extended in the following sections to test the special models used to handle abrupt area changes and crossflow.

2.4.2.1 Abrupt Area Change

For the abrupt area change, the calculation parameters given in Table 2.2 are largely the same, with the exception that the pipe is lengthened and an expansion that doubles the pipe diameter is inserted into the middle of the original pipe. The results are shown for forward and reverse flows in Fig. 2.18 and Fig. 2.19 respectively and are in agreement with the

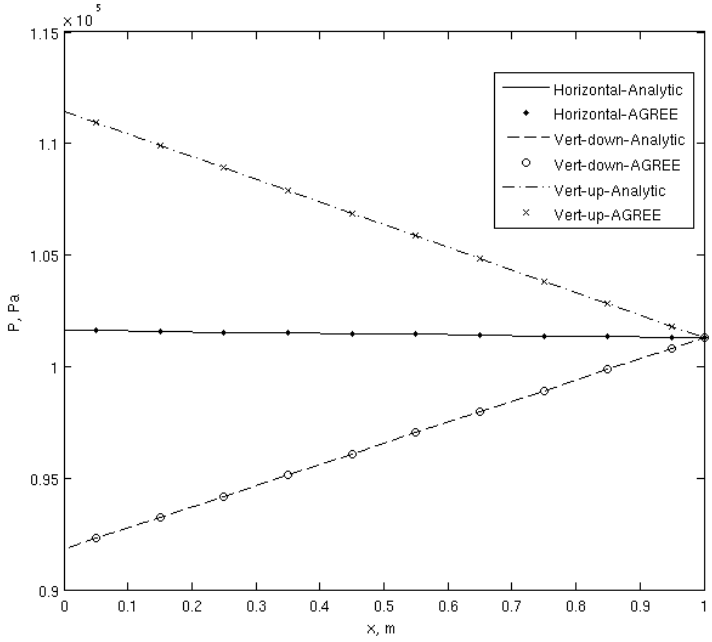

Figure 2.17: 1-D pipe verification results: pressure profile

exact solution. It is noted that two cases were run in AGREE. In AGREE-1, the abrupt area change is across two different sized channels. In AGREE-2, the abrupt area change occurs coincident with a zero volume node.

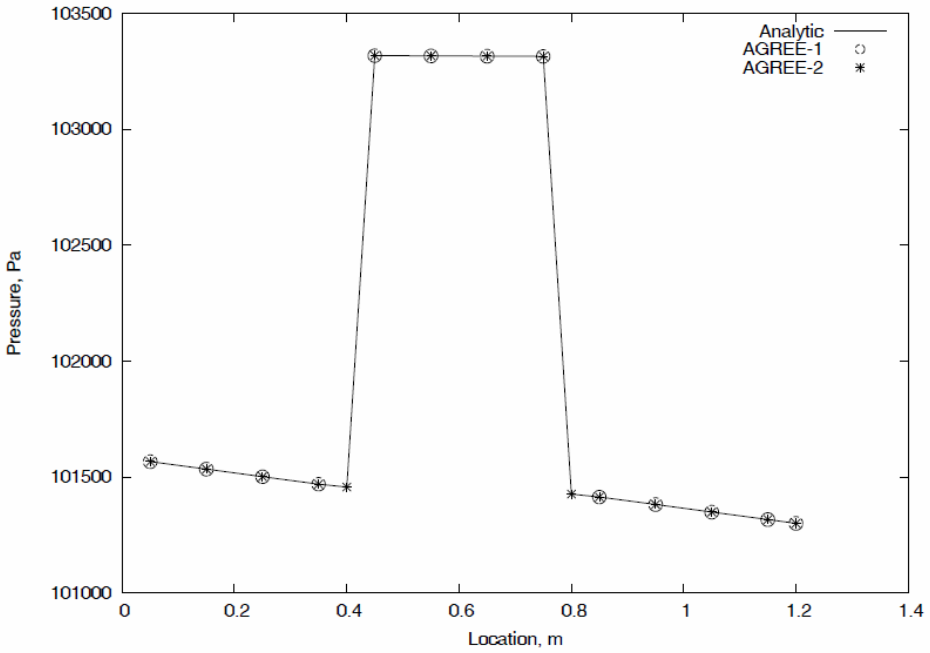

Figure 2.18: Verification calculation for abrupt area change model(forward)

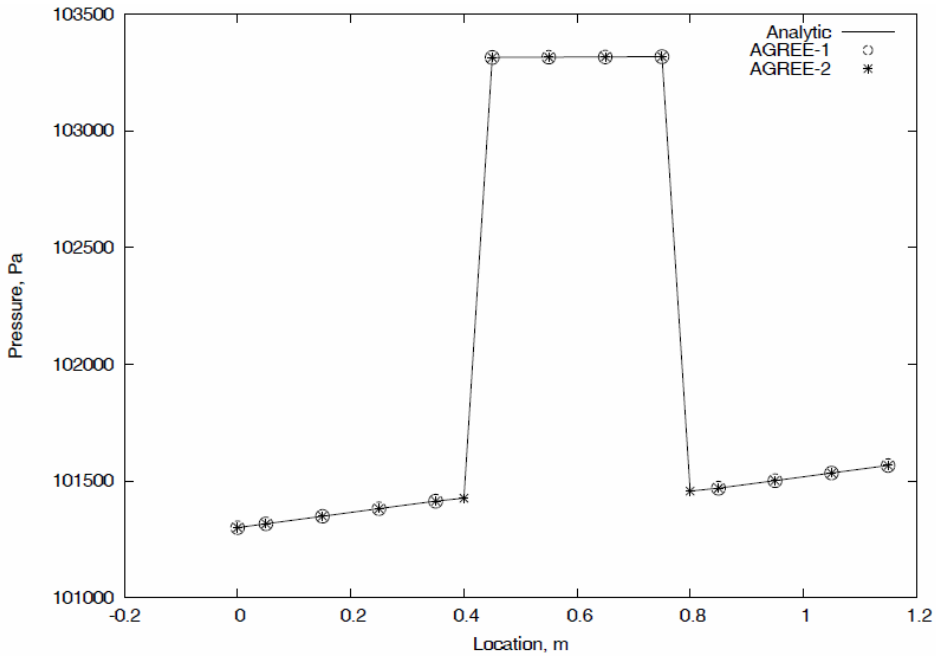

Figure 2.19: Verification calculation for abrupt area change model(reverse)

2.4.2.2 Crossflow

For the cases with cross flow, two identical channels are merged together. Three cases are tested: no area change; a contraction coincident with crossflow; and an expansion coincident with crossflow. The results are shown for forward and reverse flows in Fig. 2.20 and Fig. 2.21 respectively and are in agreement with the exact solution.

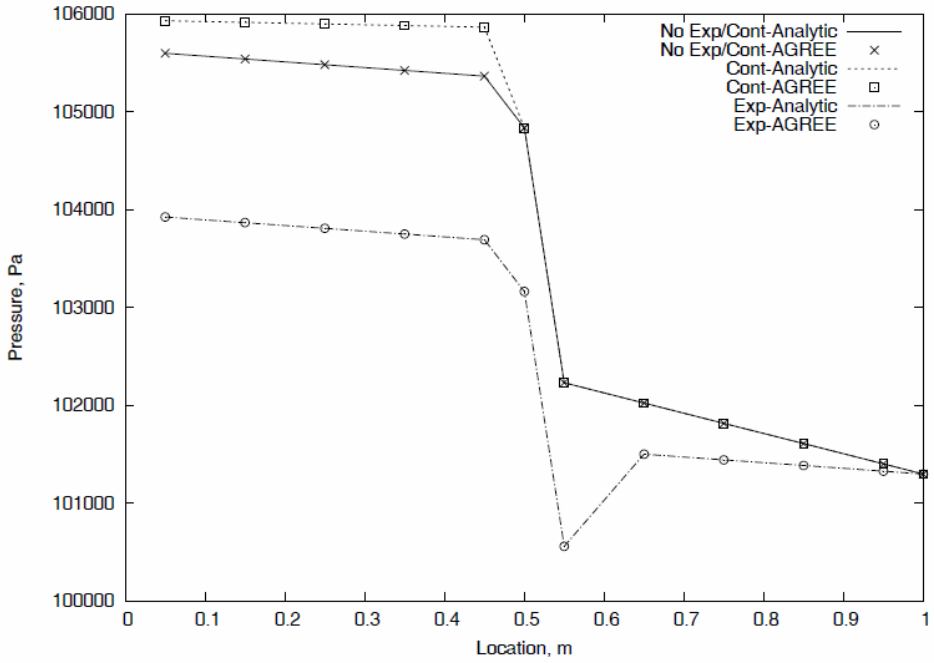

Figure 2.20: Verification of crossflow (forward)

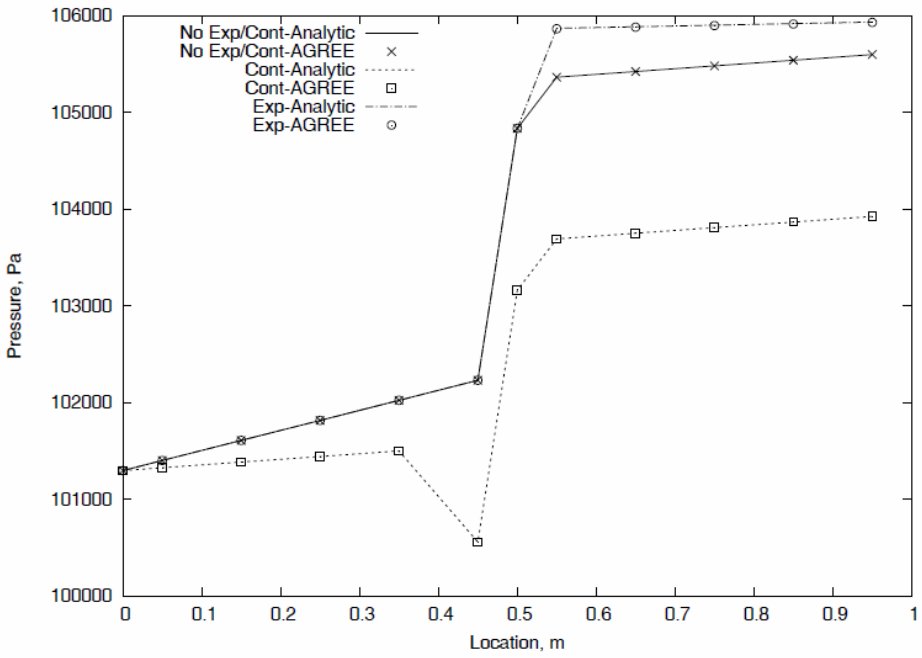

Figure 2.21: Verification of crossflow (reverse)

2.4.3 Flow Reversal Transient

In order to verify the proper behavior of the transient solver, a multichannel transient is fabricated where the steady-state solver is used in the forward direction and then the pressure boundary conditions are flipped and a transient is run in the reverse direction. The problem consists of six identical channels and is shown in Fig. 2.22 with the pressures in the inlet and outlet volumes, specified as a function of time, are shown in Fig. 2.23. The resulting pressure profiles, shown in Fig. 2.24, demonstrate that the achieved steady-state profile in the reverse direction is in agreement with the forward steady-state profile and the pressure wave propagation demonstrates physical behavior.

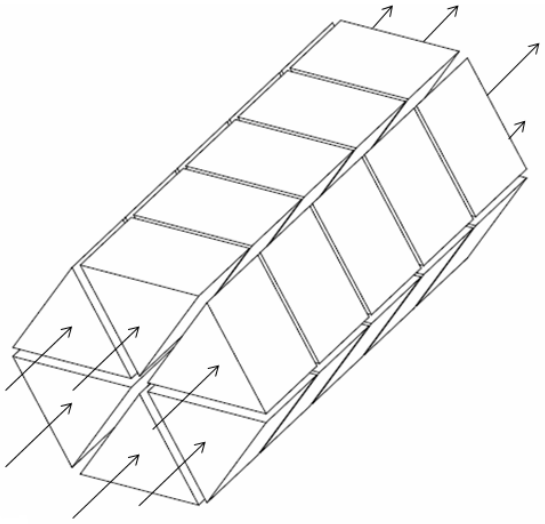

Figure 2.22: Flow reversal transient verification problem

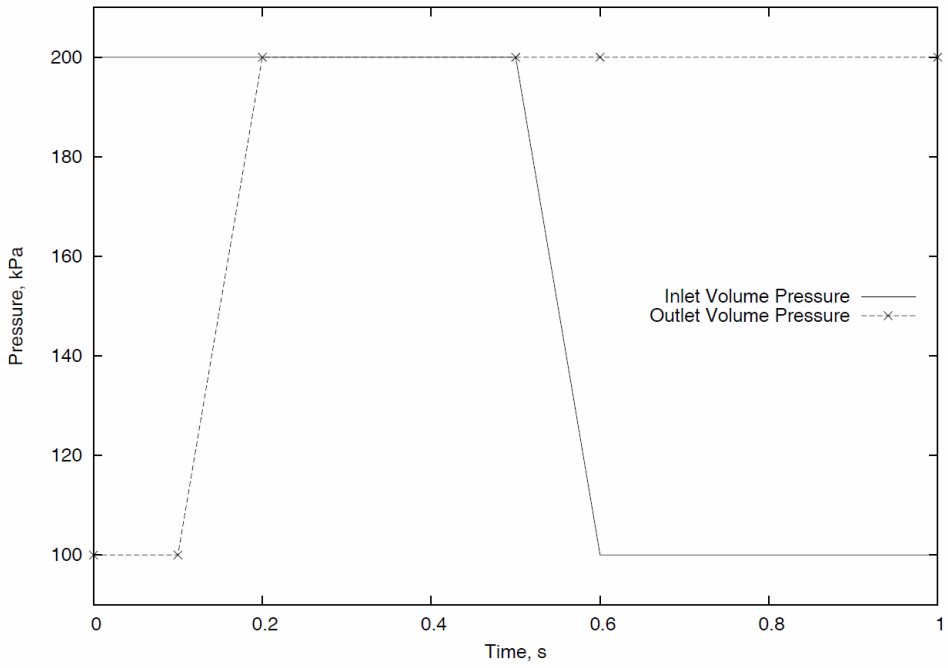

Figure 2.23: Inlet and outlet pressures for flow reversal transient

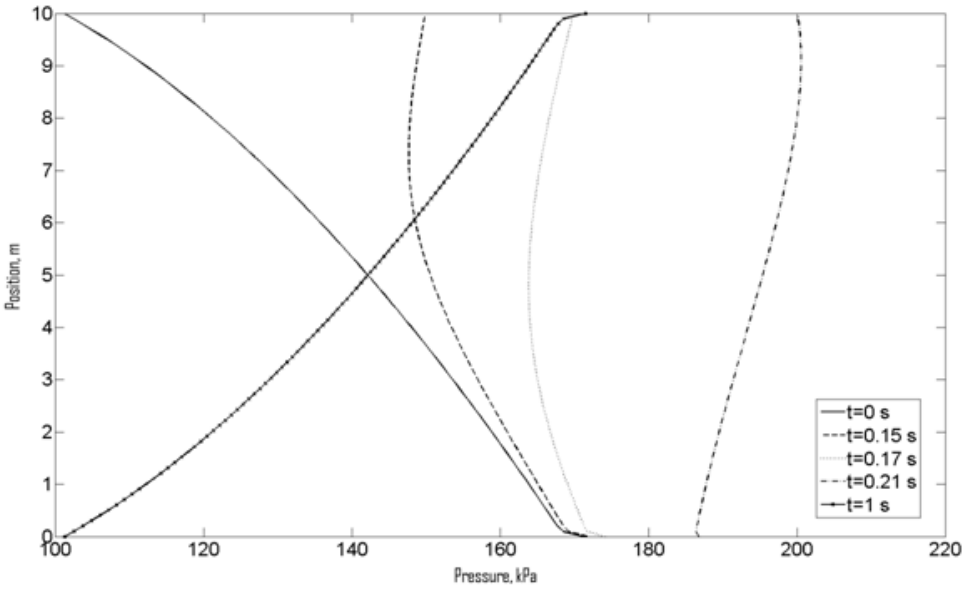

Figure 2.24: Results of reversal transient calculation

2.5 Validation Tests

The validation calculations are grouped into two sections. In the first section, a calculation of the bypass flow tests performed by Kaburaki and Takizuka [69] is performed and the resulting pressure profile is compared against the data published in the literature. In the second section, a much more comprehensive set of validation calculations are performed and compared against experimental data obtained from Seoul National University (SNU). The SNU results are also compared against other codes/methods for contrast.

2.5.1 Kaburaki and Takizuka

The calculation is performed for a bypass flow test performed by Kaburaki and Takizuka [69] and represents four full size HTTR fuel elements surrounded by a metal shroud that simulates a 1-mm bypass flow gap with a crossflow gap imposed between the 2nd and 3rd fuel element, see Fig. 2.25. To perform the calculation an initial analytic study was performed to obtain simulation parameters from the data.

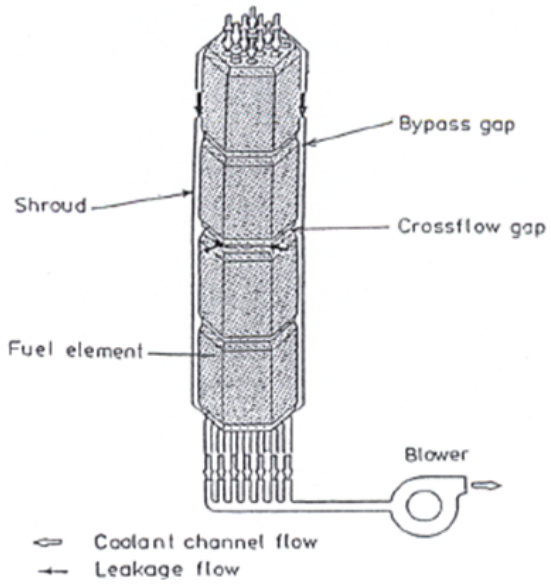

Figure 2.25: Bypass flow experiment of Kaburaki and Takisuka [69]

Kaburaki and Takizuka measured the mass flow rate to be 182 g/s. Using the measured mass flow rate and the pressure drop at the interface between the 3rd and 4th blocks, the form loss coefficient for the combined expansion/contraction is calculated to be approximately 0.3. The pressure drop at the entrance due to fluid acceleration and the entrance

loss coefficient is obtained utilizing the value of 9% for the bypass flow, which had been determined by Kaburaki and Takizuka using a flow network calculation. An entrance form loss coefficient of 0.4 is obtained from the calculation. In a manner similar to the original work of Kaburaki and Takizuka, the hydraulic diameter is adjusted to consider the effect of the insertion of the pressure tube. In combination with a friction factor obtained for a smooth pipe, a hydraulic diameter of 1.6 cm is found to produce a satisfactory slope for the pressure profile.

For the flow between the block and shroud, the pressure drop is obtained using the analytic solution for laminar flow between parallel plates given by Eq. 2.88, where u is the mean velocity of the fluid, l is the friction length, and t is the gap thickness. The Reynolds number in bypass flow channel has been calculated to be 1730.

$$\Delta p = \frac{12\mu u}{t^2} l \tag{2.88}$$

The results from the analysis with AGREE are shown in Fig. 2.26. A mass flow rate of 182 g/s with a bypass flow of 10.7% is calculated. The bypass flow over-predicts the 9% value stated by Kaburaki and Takizuka, which was obtained by a flow network calculation, by 1.7%. The data from Kaburaki and Takizuka does not include any information regarding uncertainty in the measurements; therefore, it is difficult to make statements regarding the accuracy of the calculation in regard the physical data. However, it can be observed that the pressure profile in the main coolant and bypass flow channels produced by the AGREE calculation demonstrate the same physical trends as observed in the experimental data. In particular, the large pressure drop attributed to the flow acceleration at the entrance to each flow channel is observed and appears to be correct in magnitude. The major friction losses within the flow channels appear to match the profiles well, where the Churchill correlation is used to obtain the friction factor within the turbulent regime found in the main coolant channel, and laminar flow is observed in the bypass channel. Stagnation in the bypass channel and the resulting flow acceleration that results from the merging crossflow into the main coolant channel is observed and appears to be correct in magnitude.

2.5.2 SNU Bypass Flow Tests

In order to understand the bypass flow behavior and to generate an experimental database for the validation of computer codes, a series of experiments were performed at Seoul National University (SNU) using atmospheric air [70–76]. The numerical calculations using the AGREE code are compared against other codes and with the measured data in this section. The bypass flow experiments at SNU are classified into the three phases discussed

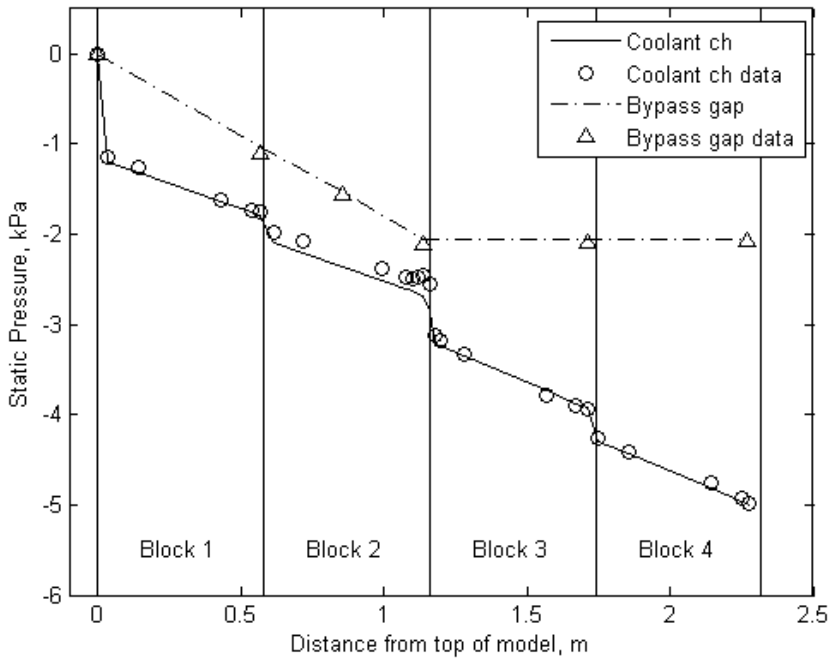

Figure 2.26: AGREE calculation of bypass flow experiment of Kaburaki and Takisuka

below.

It will be mentioned here that at the time these calculations were originally performed, not all of the features currently available in AGREE were present. The features that impact these calculations are the special models (see Section 2.3.2) that were implemented as a consequence of the phase III results, and the card based input structure that removes the input limitations discussed in some of the tests. The results presented for phase I reflect the current state of AGREE, but the results for phase II and phase III represent a version of the code that does not include the aforementioned code features.

2.5.2.1 SNU Bypass Flow Test - Phase I

Instead modeling the the entire prismatic core, the bypass flow phase I experiment at SNU focused on a triangular unit cell of the core. As shown in Fig. 2.27, the unit cell is a regular triangle section that is formed by connecting the center points of three hexagonal blocks in the core. The main phenomenon captured in the phase I experiment was the flow split between the coolant channel and the bypass gap. Three sizes of bypass gaps (i.e., 1, 3, 5 mm) were used to examine the effect. Cross flow was not considered in the phase I experiment.

The facility used in the phase I experiment is shown in Fig. 2.28. It is an open-loop facility. The working fluid was atmospheric air at room temperature. The total length and width of the experimental facility were 7.75 m and 1.40 m, respectively. The length of the test block was 79 cm, and the cross section of the test section was an equilateral triangle of 43 cm. 1/3 section of the triangle has 23 coolant holes in the case of fuel block. The test section and test blocks were made of acryl. The air flow rates were measured at the inlet of the blower and each flow measuring tube, which was installed at the downstream of the coolant channel flow of the individual test block. The bypass flow was determined by the subtraction of the coolant channel flow from the inlet flow. More detailed description of the phase I experiment is available in Refs. [70–72].

Among various block combinations considered in the experiment, F3 case having three fuel columns with different gap sizes and mass flow rates was selected for the present study since smaller uncertainties were expected in F3 case.

Table 2.3: Comparison of calculated and measured bypass flow fractions for SNU phase I experiment

Test Case	Gap size (mm)	Mass Flow-rate (kg/s)	Bypass Flow (%)				
			Experiment [72]	AGREE	GAMMA+ [38]	CFX [72]	STAR-CD [77]
G1F3W1	1	0.1801	1.19	0.94	0.33	0.41	0.32
G3F3W1	3	0.1863	4.75	5.67	5.62	4.29	-
G5F3W1	5	0.1911	10.99	11.03	11.03	10.31	10.57
G1F3W2	1	0.3736	1.39	1.11	0.63	0.64	0.51
G3F3W2	3	0.3843	4.89	5.88	5.50	4.99	-
G5F3W2	5	0.3878	10.46	11.18	11.38	10.35	9.46
G1F3W3	1	0.5560	1.22	1.16	0.92	0.77	0.61
G3F3W3	3	0.5700	4.46	6.00	5.69	5.26	-
G5F3W3	5	0.5802	10.70	11.29	11.60	10.31	10.08

Existing CFD calculations by SNU [72] and Argonne National Laboratory (ANL) [77] and GAMMA+ calculations [38] are available and are provided to show the relative accuracy of AGREE. CFX and STAR-CD are commercial computational fluid dynamics codes. GAMMA+ is a VHTR system code that models the reactor on a scale similar to AGREE [78–80]. The tabulated results, shown in Table 2.3, show that the results from AGREE compare well with experiment. The results for all codes do not demonstrate any clear bias when compared against experimental data, i.e. bypass flowrates are over-predicted for some cases and under-predicted for others. It is noted that the tabulated results make no statement in regards to uncertainty in experimental data or computation.

2.5.2.2 SNU Bypass Flow Test - Phase II

A schemcatic of the bypass flow phase II experiemnt is shown in Fig. 2.29. The layout of the phase II facility is similar to that of the phase I except the test section. The test section of the phase I experiment consisted of a single layer without any gaps. Therefore, multi-block effects such as cross-flow phenomenon or lateral flow around block periphery, could not be examined in the phase I experiment. In order to investigate such multi-block effects, multi-column and multi-layer test sections were fabricated in the phase II experiment. In other words, cross flow behavior between the bypass gap and the coolant channel as well as lateral flow behavior around the bypass gaps were the focus in the phase II experiment. The test section for the phase II experiment is shown in Fig. 2.30.

The phase II experiments utilized three types of test sections. The cross-sections of these test sections are shown in Fig. 2.31. Additionally, an acrylic test block and the coolant hole geometry are shown in Fig. 2.32 and Fig. 2.33 respectively.

Each test section represents different combinations of two types of test blocks (e.g., fuel and reflector type blocks). The test section of the experiment consists of three layers and 11 columns of acrylic test blocks. Each layer includes three hexagonal blocks in the middle row, on each side of which there are two pentagonal and rectangular blocks. The dimension of the test block was scaled down to one-third of the real block. The flat-to-flat width and height of the hexagonal test block were 120 mm and 264 mm, respectively. The bypass gap size was fixed to be 2 mm. Three cross flow gap sizes of 0, 1 mm, and 2 mm were tested. The inlet mass flow rate of the test section and outlet mass flow rate of each block column were measured to evaluate the bypass flow fraction. In contrast to the phase I experiment, the local pressure distribution was measured in the phase II along the bypass gap channel. As shown in Fig. 2.34, a total of 14 pressure taps were installed on the both side walls of the test section along the central bypass gap. More detailed descriptions of the phase II experiment are available in Refs. [71, 73].

Among various cases of the phase II experiment, six cases were considered for AGREE validation. The considered cases are summarized in Table 2.4. The geometry of the coolant holes and bypass gaps was modeled in detail. Five coolant holes in the pentagonal test block were modeled by four coolant holes to match the cross flow junctions. Fig. 2.35 shows the axial nodalization for the AGREE calculations. Due to the input limitations of AGREE at the time of the calculations, the region downstream of the coolant channels (which consists of the mixing chamber and the measuring tube) cannot be modeled. Therefore, the form loss factor was applied to consider the flow resistance after exiting the coolant channels of the test section. The form loss factor was adjusted by the case without the cross flow gap.

Fig. 2.36 through Fig. 2.41 show the results of the AGREE calculations for the phase

Table 2.4: Phase II experiments considered for AGREE validation

Test case	Test section (see Fig. 2.31)	Mass flow rate (kg/s)	Gap Size (mm)	Reference
F3CG0L	F3	0.4226	0	[71, 75, 81, 82]
F3CG0H	F3	0.5729	0	[71, 73, 75]
F3CG2L	F3	0.4179	2	[71, 75, 81, 82]
F3CG2H	F3	0.5628	2	[71, 73, 75]
F1CG0	F1	0.1783	0	[71, 75]
F1CG2	F1	0.1775	2	[71, 75, 81]

II experiment. The results are compared with the measured values. The existing CFX and GAMMA+ results are provided for the cases that are available in the literature.

Fig. 2.36 shows the AGREE result for the F3CG0L case. In order to obtain the best fit of the experimental data, the form loss factor at the outlet of the coolant channel was adjusted to be 4.5, which is utilized for all cases utilizing the F3 test section. With the same form loss factor, a good agreement is found for the F3CG0H case, results shown in Fig. 2.37, which has the flow rate increased 36%.

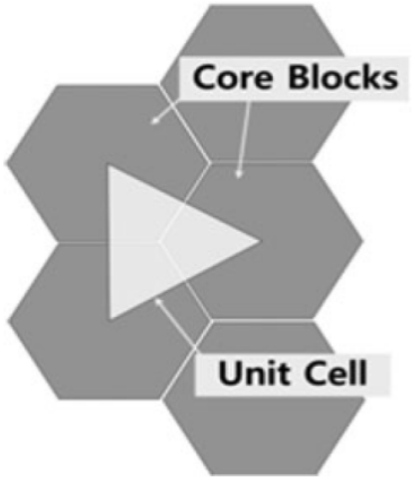

Figure 2.27: Triangular unit cell for phase I experiment [72]

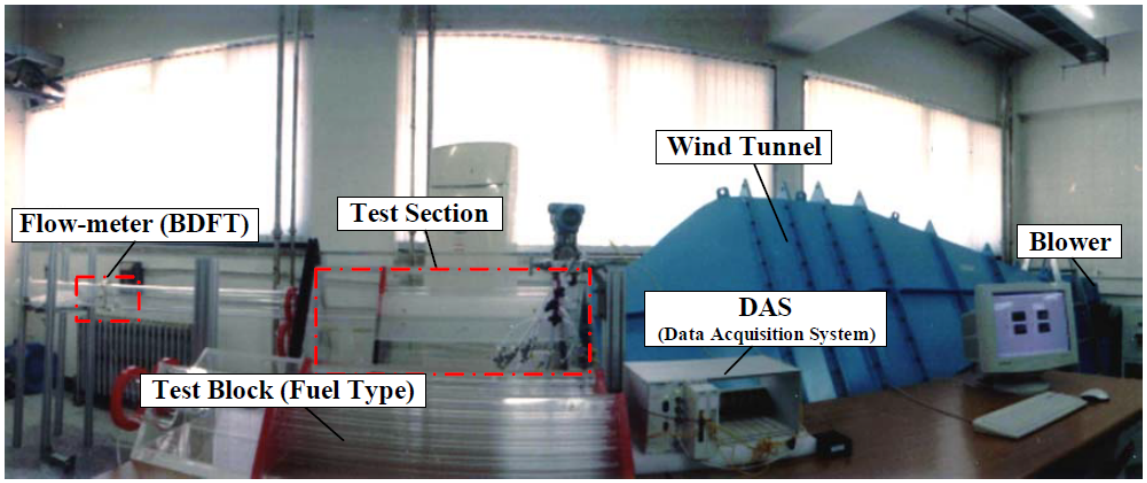

Figure 2.28: Experimental facility of bypass flow phase I experiment [70]

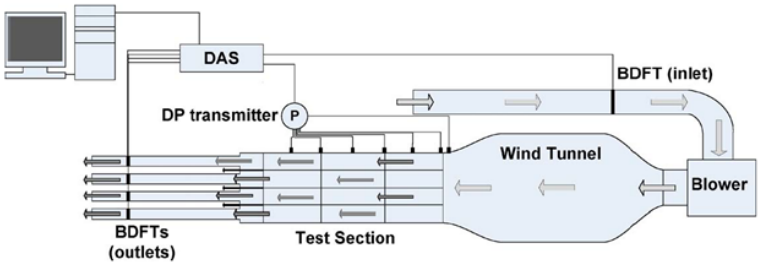

Figure 2.29: Schematic of phase II test facility

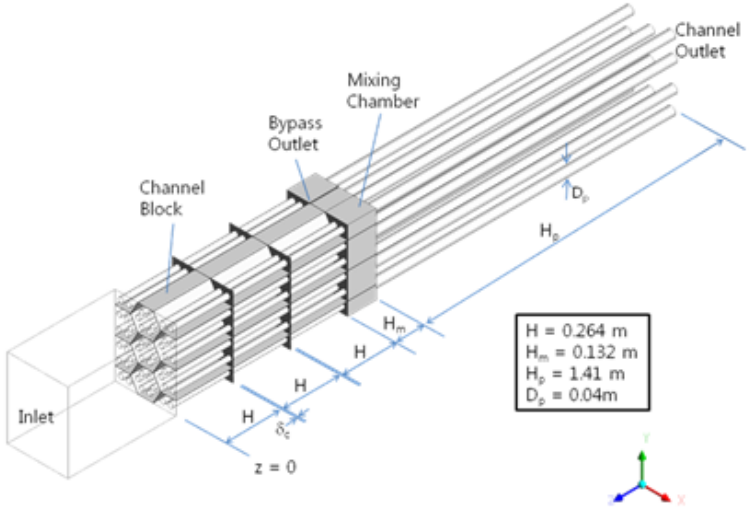

Figure 2.30: Test section of phase II experiment

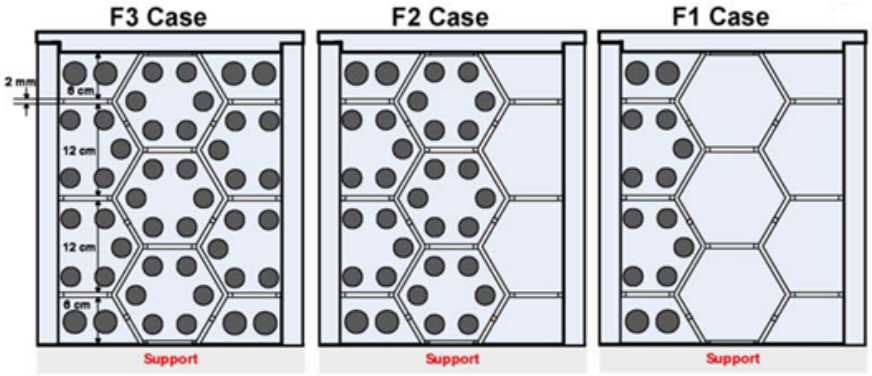

Figure 2.31: Cross-sectional view of the three types of test sections used in the phase II experiment [73]

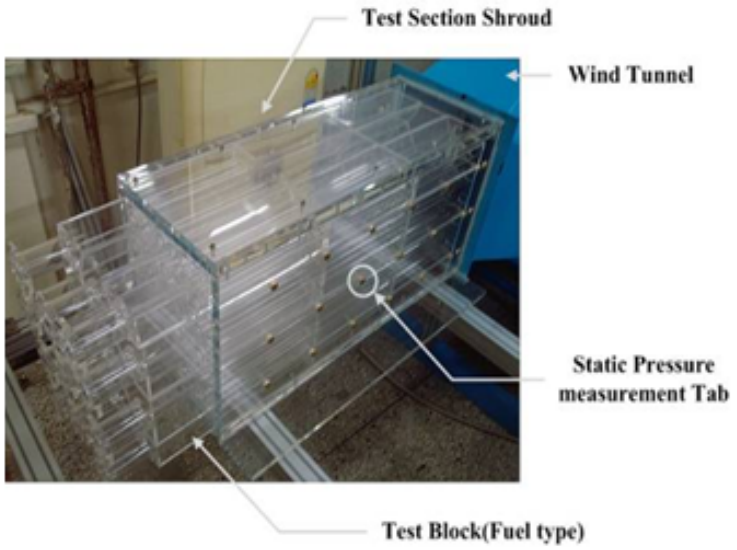

Figure 2.32: Photograph of a test block used in the phase II experiment [73]

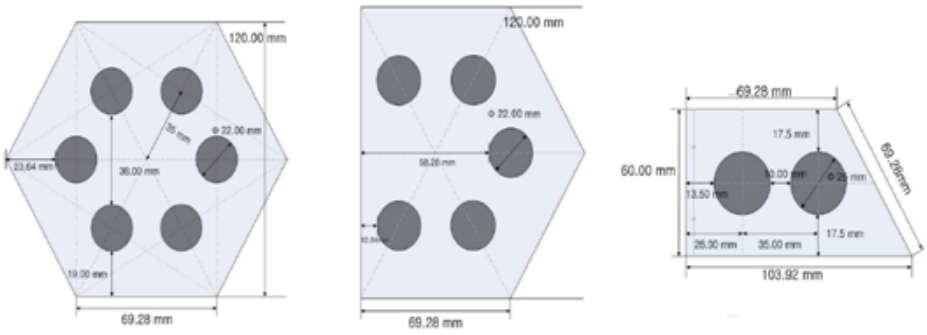

Figure 2.33: Geometry of coolant holes in fuel type test blocks of the phase II experiment [71]

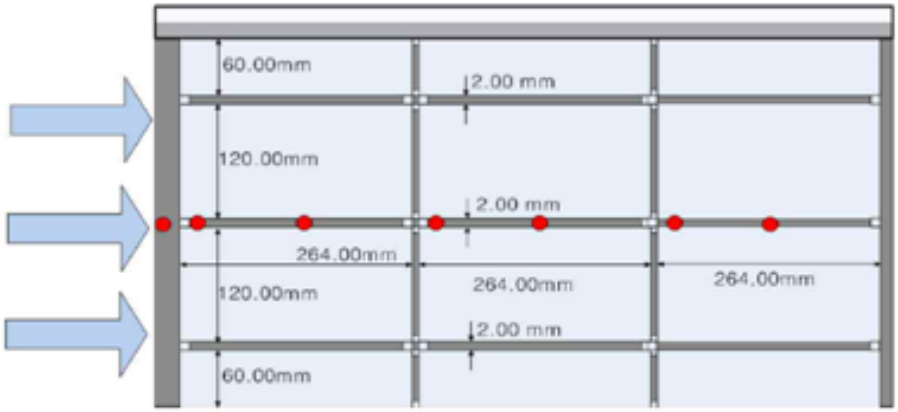

Figure 2.34: Location of pressure measurements for phase II experiment [73]

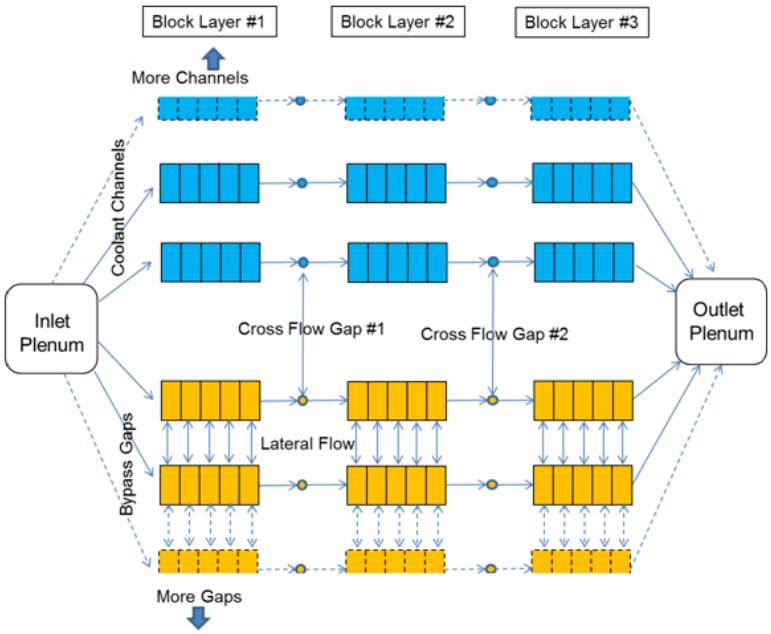

Figure 2.35: Nodalization of AGREE model for phase II experiment

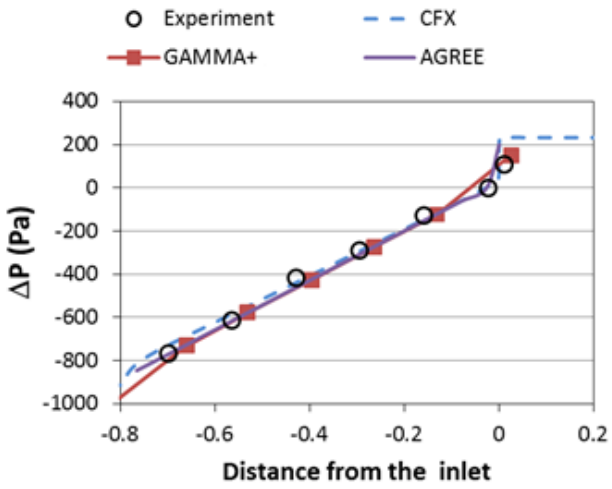

Figure 2.36: Calculated and measured pressure distributions along bypass gap for F3CG0L test case

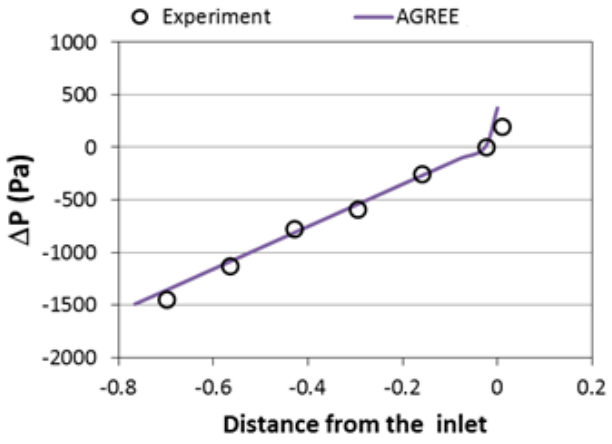

Figure 2.37: Calculated and measured pressure distributions along bypass gap for F3CG0H test case

Fig. 2.38 and Fig. 2.39 show the results of AGREE calculations for the F3CG2L and F3CG2H cases respectively. Excellent agreements can be seen in both figures.

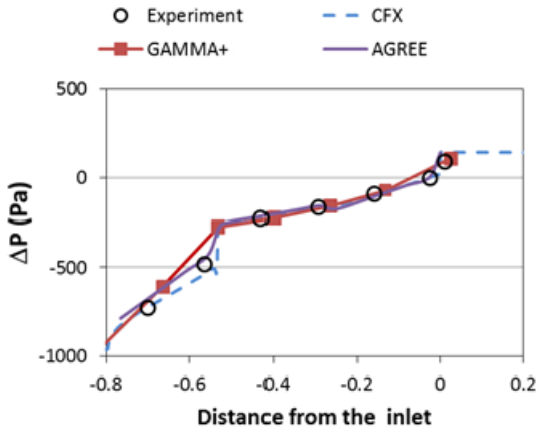

Figure 2.38: Calculated and measured pressure distributions along bypass gap for F3CG2L test case

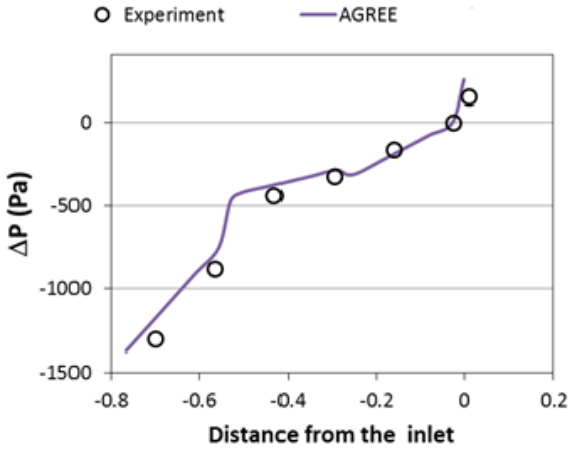

Figure 2.39: Calculated and measured pressure distributions along bypass gap for F3CG2H test case

Fig. 2.40 and Fig. 2.41 show the calculated and measured pressure distribution along the bypass gap for the F1CG0 and F1CG2 test cases respectively. For the cases utilizing the F1 test section, the form loss factor at the outlet of the coolant channel was adjusted to be 3.2. The figures show excellent agreement. The combined results from the phase II calculations indicate that AGREE can reliably simulate the flow behavior at the bypass and cross flow gaps.

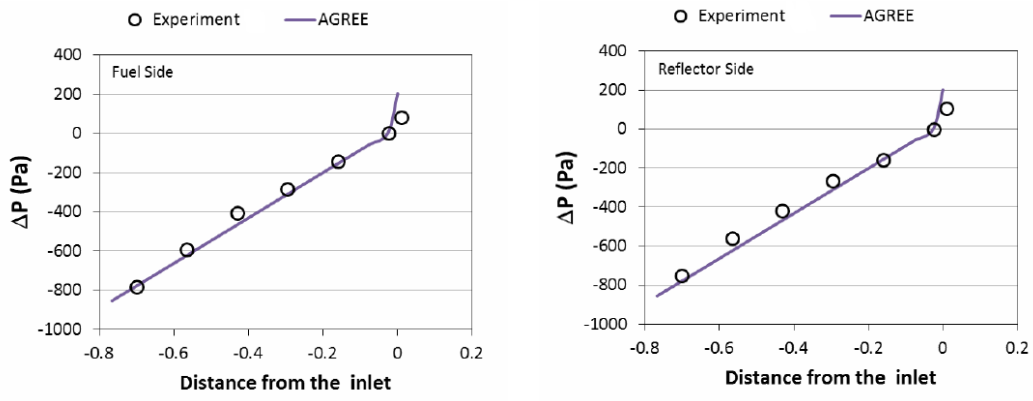

Fuel Side Reflector Side

Figure 2.40: Calculated and measured pressure distributions along bypass gap for F1CG0 test case

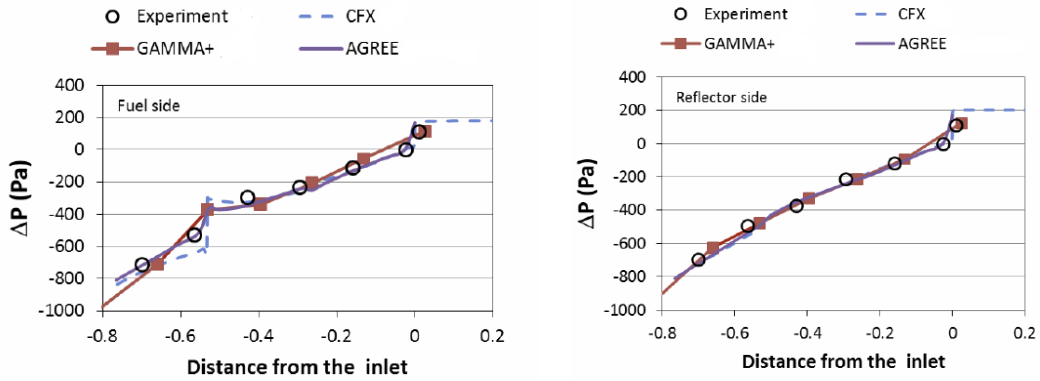

Fuel Side Reflector Side

Figure 2.41: Calculated and measured pressure distributions along bypass gap for F1CG2 test case

2.5.2.3 SNU Bypass Flow Test - Phase III

The main objective of the phase III experiment was to capture more realistic phenomena in a prismatic core. First, the vertical flow direction was selected in the phase III while the phase I and phase II had horizontal flows. The dimension of the test block was increased to a half scale in length of the real one. The number of the coolant holes in the fuel block was increased to 90. In addition, an axially non-uniform bypass gap profile was considered. Fig. 2.42 shows a schematic diagram of the test section of the phase III experimental apparatus.

A total of 28 test blocks were installed in the test section, seven columns radially and four layers axially. Among the seven columns of the test blocks, two columns were assigned for the reflector blocks as shown in Fig. 2.42. The flat-to-flat width and height of

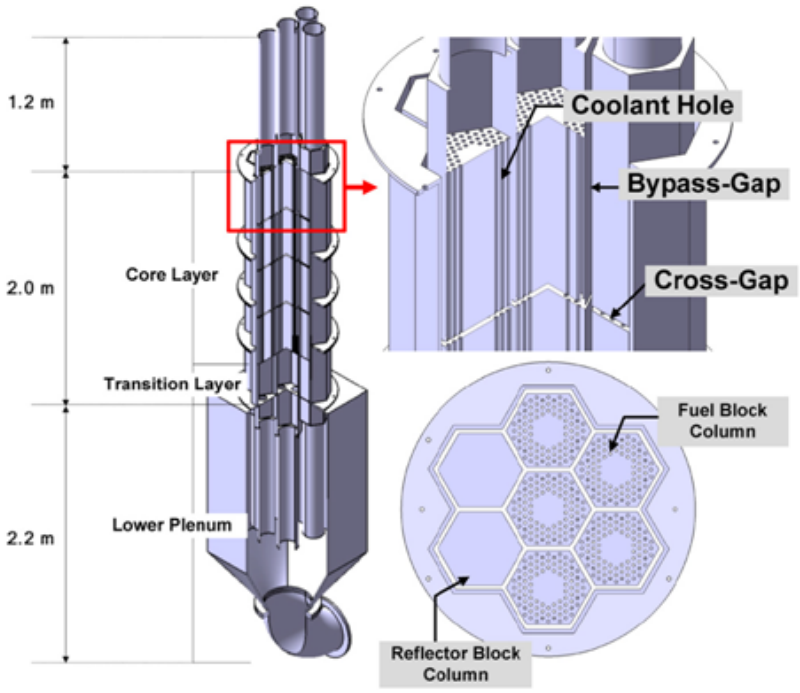

Figure 2.42: Schematic diagram of test section of the phase III experimental apparatus [76]

the test block are 18 *cm* and 40 *cm*, respectively. Four test blocks were stacked to form a single column. Transition blocks with the height of 40 *cm* were installed at the bottom of the stacked test blocks. Flow measuring pipes were installed at the top of the fuel columns and the bottom of the transition blocks to measure the inlet and outlet mass flow rates of each block column. Mass flow rate was measured by using an average Pitot tube flowmeter. Fig. 2.43 shows a detailed geometry of the fuel test block used in the Phase III experiment. There are 90 coolant holes within the fuel block. The central part of the fuel block, i.e., the hole within the guide tube was used for the path where the measurement wires were placed. The inner diameter of the coolant hole is 8 *mm*. Fig. 2.44 shows the location for the local pressure measurement. Measurement error of the pressure transmitter was reported to be 5% [76].

Fig. 2.45 shows the AGREE model built to simulate the phase III experiment. 90 coolant channels used in the fuel block of the experiment were modeled as 6 coolant channels in AGREE. The lateral flow between the bypass gaps as well as the cross flow between the coolant channel and the bypass gap were modeled in detail. Only the four stacks of the test blocks were modeled. The flow resistance through the measuring pipes and the transition blocks were modeled by the form losses which were obtained by the adjustment of the

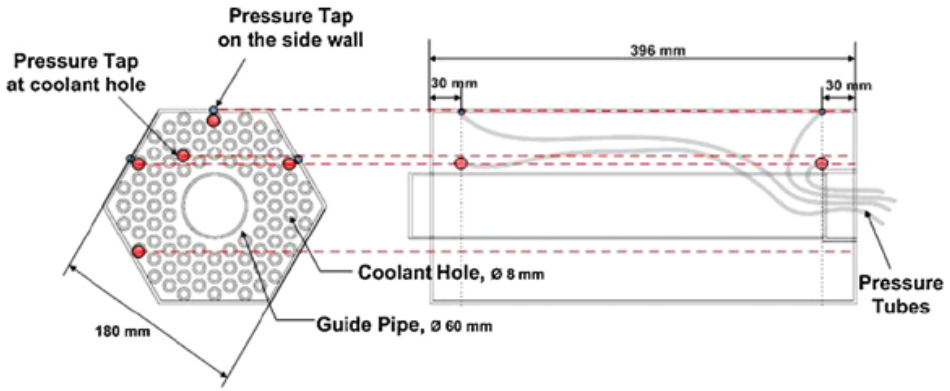

Figure 2.43: Geometry of fuel test block used in phase III experiment [76]

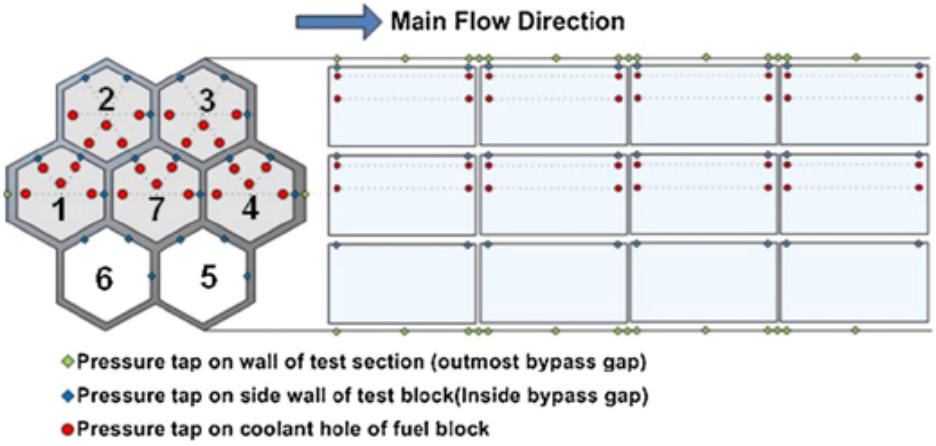

Figure 2.44: Location of pressure measurements for phase II experiment [76]

experimental data. Three cases were considered for the AGREE validation calculations. The parameters of these cases are provided in Table 2.5

Since the measuring pipes and the transition blocks were not considered in the AGREE model, form losses were applied at those positions to consider the flow resistance. Since all inlet and outlet positions were required form losses, a trial-and-error method was used to obtain the form loss factors. The experimental data without cross flow gaps (i.e., BG2CG0) were used for the adjustment. Fig. 2.46 and Fig. 2.47 show the calculated pressure distributions using the adjusted loss factors in the coolant and bypass channels respectively. Using the adjusted form loss factors based on the case of BG2CG0, the other two cases were analyzed with AGREE. The results are shown in Fig. 2.48 through Fig. 2.51.

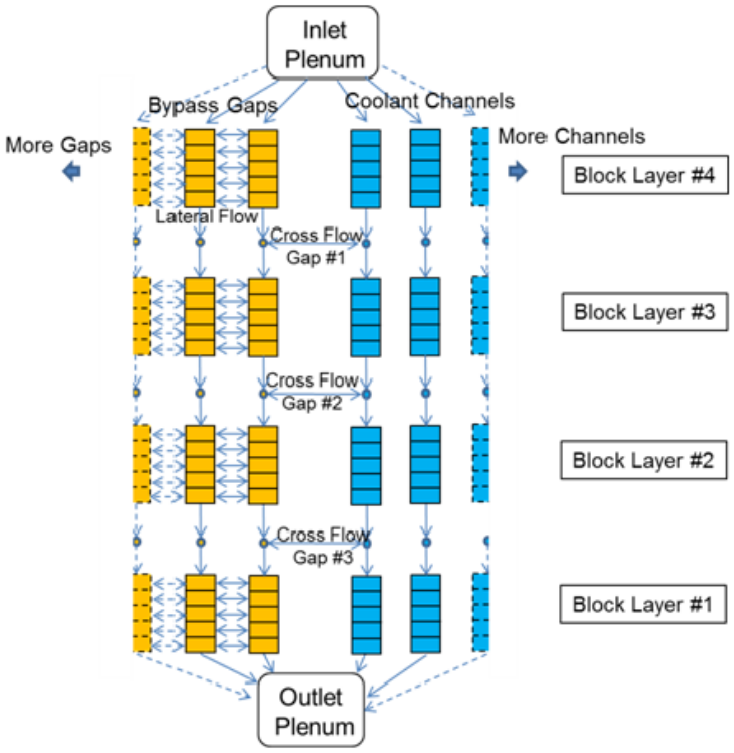

Figure 2.45: Axial nodaliztion of AGREE model for phase III experiment

Table 2.5: Phase III experiments considered for AGREE validation

Test case	Inlet mass flow rate (kg/s)	Bypass gap size (mm)	Cross flow gap size (mm)
BG2CG0	1.234	2	0
BG6242CG2	1.221	6,2,4,2 -axially varying from top	2
BG6242-0-CG2	1.109	6,2,4,2 -axially varying from top -bottom of bypass gaps blocked	2

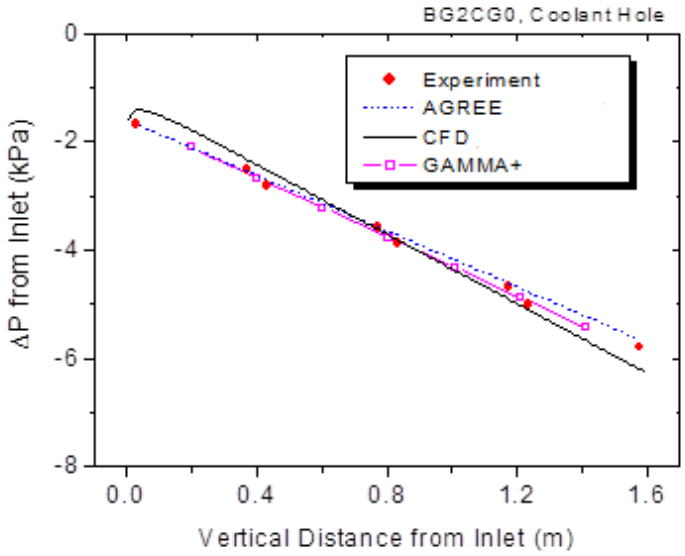

Figure 2.46: Calculated and measured pressure distributions along the coolant channel for BG2CG0 test case

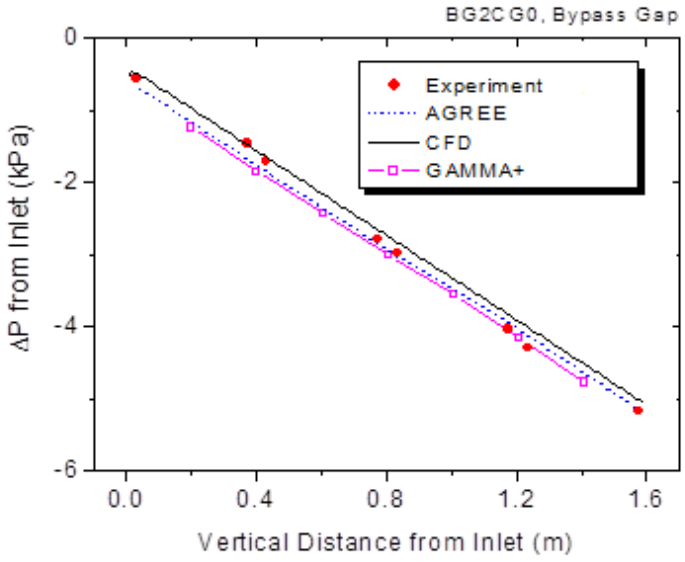

Figure 2.47: Calculated and measured pressure distributions along bypass gap for BG2CG0 test case

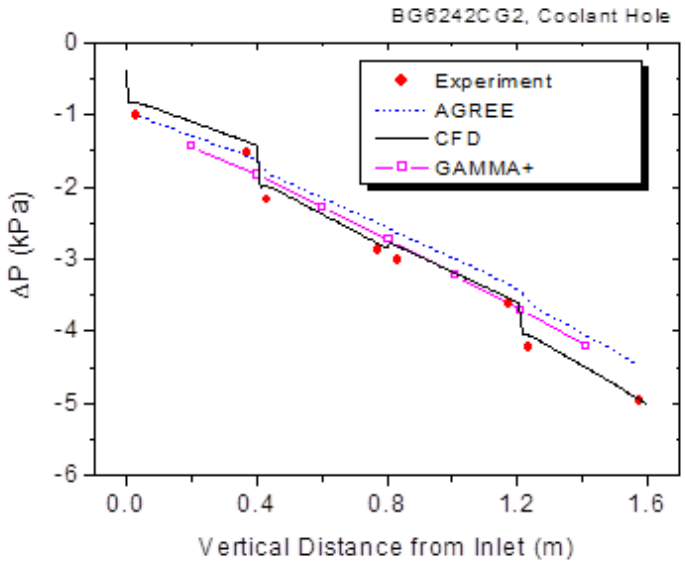

Figure 2.48: Calculated and measured pressure distributions along the coolant channel for test case BG6242CG2

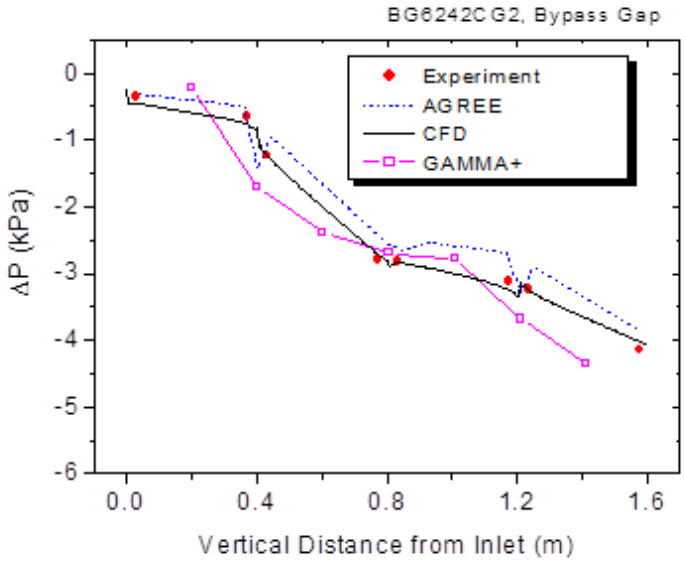

Figure 2.49: Calculated and measured pressure distributions along bypass gap for test case BG6242CG2

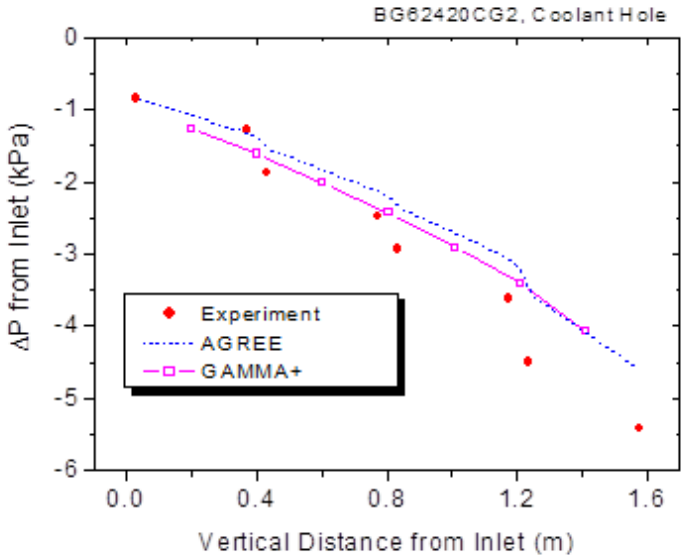

Figure 2.50: Calculated and measured pressure distributions along the coolant channel for test case BG6242-0-CG2

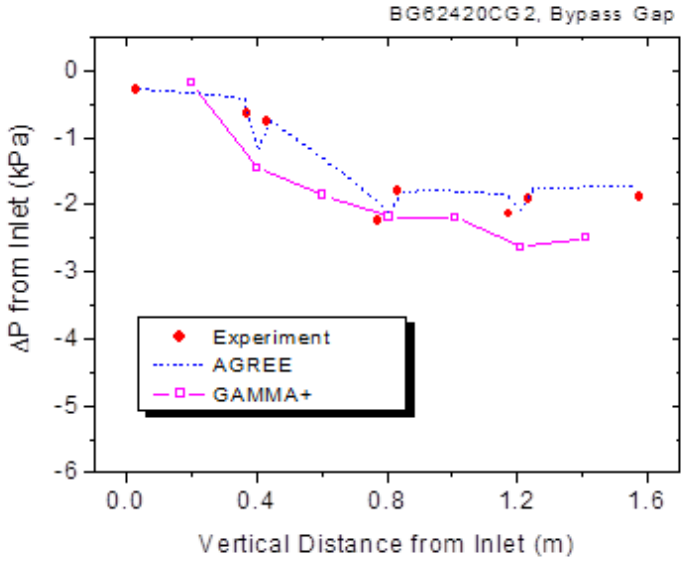

Figure 2.51: Calculated and measured pressure distributions along bypass gap for BG6242-0-CG2 test case

CHAPTER 3

The Adjoint System

3.1 Introduction

The implementation of the adjoint into a system code is motivated by the utility provided by the adjoint solution. Uses of the adjoint solution include efficient determination of sensitivity derivatives, design optimization, correction of numerical estimates of SRQs, input parameter correction, and error propagation. Sensitivity derivatives, obtained from system calculations, can be used in the design of experiments, e.g. a designer can efficiently test consistency of the sensitivities of a scaled down experiment to the original system. Likewise, the sensitivities can be used to optimize system design and improve stability. In regards to solution accuracy, the use of the adjoint solution to correct numerical estimates has been shown to produce estimates of SRQs that are proportional to the product of the errors in the primal and adjoint solutions [83]. Using data from integral experiments, consistent adjustment of input parameters has been conducted with the aid of the adjoint solution [84–86].

This chapter will focus on the details regarding the adjoint system. It begins by introducing adjoints as an efficient means for determining sensitivity derivatives and discussing various properties of the adjoint solution in Section 3.2. An effective adjoint based surrogate is derived in Section 3.3. As a means of clarification, an illustrative example is provided in Section 3.4.

3.2 Properties of Adjoints

3.2.1 Methods of Obtaining Sensitivity Derivatives

The problem of interest is the following. Consider a computational problem, where the solution state is given by Eq. 3.1, where R represents the residual in the calculation, U is

the state vector that contains the primary variables (e.g. velocities, pressures, temperatures, etc.), and μ is the vector of input parameters (e.g. boundary conditions, thermal-fluid properties, geometries, etc.). Next, consider a system response quantity $J(U)$. The problem, outlined in Eq. 3.2, is to calculate how changes in the input parameters affect the SRQ, i.e. sensitivity derivatives.

$$R(U,\mu) = 0 \tag{3.1}$$

$$\underbrace{\mu}_{\text{inputs} \in \mathbb{R}^m} \rightarrow \underbrace{R(U,\mu) = 0}_{N \text{ equations}} \rightarrow \underbrace{U}_{\text{state} \in \mathbb{R}^N} \rightarrow \underbrace{J(U)}_{\text{output (scalar)}} \tag{3.2}$$

There are three well known methods for obtaining sensitivity derivatives. These methods: finite differences, tangent-linear, and adjoint approaches are discussed below.

3.2.1.1 Finite Differences

The finite differencing approach is the most straight-forward method for obtaining sensitivity derivatives and follows directly from the definition. The finite difference formula, given by Eq. 3.3, is the simplest means of approximating the sensitivity derivative as it can use the solver as a black box. Thus, finite-differences are naturally non-intrusive. However, this approach suffers from serious drawbacks. One problem is that it is not obvious how to choose an appropriate value for $\Delta\mu_i$. If $\Delta\mu_i$ is chosen to be too large, the finite difference will not approximate the limit value, but if too small, numerical precision will destroy the accuracy of the approximation. A more serious problem, however, is that this approximation requires one functional evaluation for each degree of freedom in the parameter space. When each functional evaluation requires an expensive calculation, this approach quickly becomes impractical, and a more intelligent algorithm is required. However, due to its simplicity, the finite difference approach is an effective method for the verification of alternative approaches.

$$\frac{dJ}{d\mu_i} \approx \frac{J\big(U(\mu_i + \Delta\mu_i)\big) - J\big(U(\mu_i)\big)}{\Delta\mu_i} \tag{3.3}$$

3.2.1.2 Tangent Linear

The tangent linear approach begins by differentiating the SRQ with respect to input parameter μ_i as shown in Eq. 3.4.

$$\frac{dJ}{d\mu_i} = \frac{\partial J}{\partial U}\frac{dU}{d\mu_i} + \frac{\partial J}{\partial \mu_i} \tag{3.4}$$

In Eq. 3.4, $\partial J/\partial U$ and $\partial J/\partial \mu_i$ are generally trivial calculations that can be performed by hand, but $dU/d\mu_i$ remains unknown. To resolve this issue, we differentiate Eq. 3.1 and rearrange to obtain the tangent linear equation associated with the system, given by Eq. 3.5. In the tangent linear equation $\partial R/\partial U$ is a square matrix that needs to be inverted in order to determine $dU/d\mu_i$, which is needed to calculate the sensitivity derivative. Thus, a matrix "inversion" is required for each input parameter.

$$\frac{\partial R}{\partial U}\frac{dU}{d\mu_i} = -\frac{\partial R}{\partial \mu_i} \tag{3.5}$$

One advantage of the tangent linear equation is that it is always linear (in the case of a linear partial differential equation, $\partial R/\partial U$ is trivial). Thus, this calculation is generally straightforward. The main drawback to the tangent linear approach occurs if the parameter space is large, requiring a large number of matrix "inversions". As this situation is the norm for the situations encountered with system codes, an alternative approach is utilized.

3.2.1.3 Adjoint

The adjoint approach can be seen as an extension of the tangent linear aproach. First, rewrite Eq. 3.5 as Eq. 3.6 and place into Eq. 3.4 to yield Eq. 3.7.

$$\frac{dU}{d\mu_i} = -\left(\frac{\partial R}{\partial U}\right)^{-1}\frac{\partial R}{\partial \mu_i} \tag{3.6}$$

$$\frac{dJ}{d\mu_i} = -\frac{\partial J}{\partial U}\left(\frac{\partial R}{\partial U}\right)^{-1}\frac{\partial R}{\partial \mu_i} + \frac{\partial J}{\partial \mu_i} \tag{3.7}$$

Eq. 3.7 motivates the definition of a new variable, the adjoint, defined by Eq. 3.8. Rearranging, we arrive at the adjoint equation given by Eq. 3.9. Placing the definition of the adjoint into Eq. 3.7 we obtain the adjoint based sensitivity derivative given by Eq. 3.10.

$$\Psi^T = -\frac{\partial J}{\partial U}\left(\frac{\partial R}{\partial U}\right)^{-1} \tag{3.8}$$

$$\left(\frac{\partial R}{\partial U}\right)^T \Psi = -\left(\frac{\partial J}{\partial U}\right)^T \tag{3.9}$$

$$\frac{dJ}{d\mu_i} = \Psi^T\frac{\partial R}{\partial \mu_i} + \frac{\partial J}{\partial \mu_i} \tag{3.10}$$

Observing Eq. 3.9, it is clear that the adjoint solution is independent of the number of input parameters. Thus, only one matrix "inversion" is required per SRQ. The remaining calculations to determine the sensitivity derivatives are inexpensive dot products (BLAS 1 operations), one per parameter. When the parameter space is large, the adjoint approach is the clear choice for obtaining sensitivity derivatives.

3.2.2 Physical Interpretation of the Adjoint

Consider the case where we are interested in quantifying the impact of a source term perturbation on the SRQ. This situation is shown in Eq. 3.11 and Eq. 3.12. Multiplying Eq. 3.12 by the adjoint and rearranging we gain insight into the meaning of the adjoint, as represented by Eq. 3.13. The adjoint is a weighting function that determines how much a change in the source affects a change in the SRQ, i.e. it can be viewed as an importance function [87] (the minus sign is merely an artifact of the definition given by Eq. 3.8).

$$R(U,\mu) = AU - f = 0 \rightarrow A(U+\delta U) = f + \delta f \tag{3.11}$$

$$A\delta U = \delta f \tag{3.12}$$

$$\Psi^T \delta f = \Psi^T A \delta U = (A^T \Psi)\delta U = -\left(\frac{\partial J}{\partial U}\right)^T \delta U = -\delta J$$

$$\delta J = -\Psi^T \delta f \tag{3.13}$$

3.2.2.1 Lagrange Viewpoint

An alternative approach to gaining insight into the meaning of the adjoint can be obtained using the Lagrange multiplier technique from multivariate calculus (used for constrained optimization) [88]. Start by setting up an augmented function, given by Eq. 3.14, and differentiate. Choosing the Lagrange multiplier to satisfy the adjoint equation, given by Eq. 3.16, we obtain an expression for the derivative of the augmented function given by Eq. 3.17. Comparing Eq. 3.17 with Eq. 3.10, we can see the similarities between adjoints and Lagrange multipliers. Thus, insights previously obtained from working with Lagrange multipliers are analogous to the adjoint solution.

$$\mathscr{L}(U,\mu,\lambda) = J(U(\mu)) - \lambda^T R(U,\mu) \tag{3.14}$$

$$d\mathscr{L} = \Big(\frac{\partial J}{\partial U} - \lambda^T \frac{\partial R}{\partial U}\Big) dU + \Big(\frac{\partial J}{\partial \mu} - \lambda^T \frac{\partial R}{\partial \mu}\Big) d\mu \tag{3.15}$$

$$\Big(\frac{\partial R}{\partial U}\Big)^T \lambda = \Big(\frac{\partial J}{\partial U}\Big)^T \tag{3.16}$$

$$\frac{d\mathscr{L}}{d\mu} = \frac{\partial J}{\partial \mu} - \lambda^T \frac{\partial R}{\partial \mu} \tag{3.17}$$

3.2.3 Continuous vs. Discrete

Up to this point, the adjoint discussion has focused on the discrete approach. In the discrete approach, one works directly with the discretized algebraic equations. The alternative is the continuous approach, where one obtains the adjoint form of the field equations, and then discretizes the adjoint field equations. To clarify, consider the 1-D convection-diffusion operator given by Eq. 3.18.

$$Lu = \frac{du}{dx} - D\frac{d^2u}{dx^2} \tag{3.18}$$

with boundary conditions,

$$u(0) = u(1) = 0$$

Taking the inner product of Lu with the adjoint Ψ,

$$\begin{aligned}
\langle \Psi, Lu \rangle &= \int_0^1 \Psi \Big(\frac{du}{dx} - D\frac{d^2u}{dx^2}\Big) dx \\
&= \Big[\Psi u\Big]_0^1 - \int_0^1 u\frac{d\Psi}{dx}dx - \Big[D\Psi\frac{du}{dx}\Big]_0^1 + \int_0^1 \frac{du}{dx}\frac{d\Psi}{dx}dx \\
&= \int_0^1 u\Big(-\frac{d\Psi}{dx} - D\frac{d^2\Psi}{dx^2}\Big)dx + \Big[\Psi u - D\Psi\frac{du}{dx} + Du\frac{d\Psi}{dx}\Big]_0^1
\end{aligned}$$

Applying the boundary conditions,

$$\langle \Psi, Lu \rangle = \langle u, L^*\Psi \rangle = \int_0^1 u\Big(-\frac{d\Psi}{dx} - D\frac{d^2\Psi}{dx^2}\Big)dx$$

This leads to the adjoint of the convection-diffusion operator given by Eq. 3.19.

$$L^*\Psi = -\frac{d\Psi}{dx} - D\frac{d^2\Psi}{dx^2} \tag{3.19}$$

with boundary conditions,

$$\Psi(0) = \Psi(1) = 0$$

This same procedure is used to obtain the adjoint operators for any field equation. Some of these operators are shown in Table 3.1 [88]. Observing these operators, one can see the change in sign associated with the first order derivatives (all odd order derivatives have a change in sign). This change of sign implies a reversal in the direction of information propagation, which will be discussed in the following section.

This section has discussed the continuous adjoint approach, which provides excellent insight into the field equations. However, the discrete adjoint approach has more popularity in the CFD community and is utilized in AGREE because of the following reasons. First, the discrete approach produces the exact gradient of the SRQ with respect to the discretized primal solution. A more pragmatic argument for the discrete adjoint approach is simplicity. When utilizing the discrete approach, one does not need to be concerned about proper treatment of adjoint boundary conditions or discretization of the adjoint equations as all of this information is obtained from primal system.

Table 3.1: Operators and their adjoints

Operator	Adjoint
$\frac{du}{dx} - D\frac{d^2u}{dx^2}$	$-\frac{d\Psi}{dx} - D\frac{d^2\Psi}{dx^2}$
$\nabla \cdot (k\nabla u)$	$\nabla \cdot (k\nabla \Psi)$
$\frac{du}{dt} + \frac{du}{dx}$	$-\frac{d\Psi}{dt} - \frac{d\Psi}{dx}$

3.2.4 Information Propagation

In discussing the continuous approach to the adjoint problem, it was shown that the first order derivatives have a change in sign which in indicates a reversal in the direction of information propagation. This means the convection direction is reversed and time needs to be marched backwards. The discrete approach provides a direct way to see this. Consider an upwind differenced convection equation given by Eq. 3.20 and Eq. 3.21, where the subscript n refers to the spatial location and the superscript p refers to the time step.

$$\frac{\partial u}{\partial t} + c\frac{\partial u}{\partial x} = 0 \tag{3.20}$$

$$\frac{u_n^p - u_n^{p-1}}{\Delta t} + c\frac{u_n^p - u_{n-1}^p}{\Delta x} = 0 \tag{3.21}$$

Combining all time steps and spatial nodes, we can write the system of equations as a block matrix given by Eq. 3.22. The matrix in Eq. 3.22 is a lower triangular block matrix indicating that information from earlier times is required to solve the system at later times, i.e. information is propagating forward in time. Likewise, matrix B is lower triangular indicating that information propagates downstream.

$$R(U) = \begin{pmatrix} I & & & \\ A & B & & \\ & \ddots & \ddots & \\ & & A & B \end{pmatrix} \begin{pmatrix} u^0 \\ u^1 \\ \vdots \\ u^P \end{pmatrix} - \begin{pmatrix} b^0 \\ b^1 \\ \vdots \\ b^P \end{pmatrix} = 0 \tag{3.22}$$

with,

$$A = \begin{pmatrix} 0 & & & \\ & -\frac{1}{\Delta t} & & \\ & & \ddots & \\ & & & -\frac{1}{\Delta t} \end{pmatrix} \qquad B = \begin{pmatrix} 1 & & & \\ -\frac{c}{\Delta x} & \left(\frac{1}{\Delta t} + \frac{c}{\Delta x}\right) & & \\ & \ddots & \ddots & \\ & & -\frac{c}{\Delta x} & \left(\frac{1}{\Delta t} + \frac{c}{\Delta x}\right) \end{pmatrix}$$

Differentiating and transposing $R(U)$ from Eq. 3.22 we arrive at Eq. 3.23.

$$\left(\frac{\partial R}{\partial U}\right)^T = \begin{pmatrix} I & A & & \\ & B^T & \ddots & \\ & & \ddots & A \\ & & & B^T \end{pmatrix} \tag{3.23}$$

with,

$$B^T = \begin{pmatrix} 1 & -\frac{c}{\Delta x} & & \\ & \left(\frac{1}{\Delta t} + \frac{c}{\Delta x}\right) & \ddots & \\ & & \ddots & -\frac{c}{\Delta x} \\ & & & \left(\frac{1}{\Delta t} + \frac{c}{\Delta x}\right) \end{pmatrix}$$

The matrix in Eq. 3.23 is an upper triangular block matrix indicating that information from later times is required to solve the system at earlier times, i.e. information is now propagating backward in time. Likewise, matrix B^T is upper triangular indicating that information propagates upstream.

3.3 Adjoint Corrected Surroagate

The adjoint solution has been demonstrated as a useful tool for improving the accuracy of an estimation to a SRQ. Following the work of Pierce and Giles [83], Ghate and Giles demonstrated a method for obtaining a surrogate with a leading error term of third order [89] that requires the solution of both the tangent-linear equation and the adjoint equation. The following alternative derivation begins with a Taylor series for the system quantities in terms of the input parameters:

$$U(\mu) = U(\mu_0) + \frac{dU}{d\mu}\Big|_{\mu_0} \delta\mu + O(\|\delta\mu\|^2) \tag{3.24}$$

Define the linear extrapolated system state:

$$U^* = U(\mu_0) + \frac{dU}{d\mu}\Big|_{\mu_0} \delta\mu \tag{3.25}$$

The next step is to perform a Taylor series for the SRQ about U^*. In this step the key point is that the direct effects of the input parameters, μ, on the SRQ, J, are handled directly as this is computationally inexpensive. Recalculating the system resonse, however, is expensive. Thus the system response is estimated via a first order Taylor series.

$$J(U,\mu) = J(U^*,\mu) + \frac{\partial J}{\partial U}\Big|_{U^*} (U - U^*) + O(\|U - U^*\|^2) \tag{3.26}$$

The problem we encounter is that we do not know the value of the partial derivative at U^*. From Eq. 3.9:

$$J(U,\mu) = J(U^*,\mu) - \left(\Psi^T \frac{\partial R}{\partial U}\right)_{U^*} (U - U^*) + O(\|U - U^*\|^2) \tag{3.27}$$

Take the adjoint solution from the unperturbed system as the adjoint is not known at the extrapolated state:

$$J(U,\mu) = J(U^*,\mu) - \left(\left(\Psi_0^T + \delta\Psi^T\right) \frac{\partial R}{\partial U}\right)_{U^*} (U - U^*) + O(\|U - U^*\|^2) \tag{3.28}$$

$$J(U,\mu) = J(U^*,\mu) - \Psi_0^T \frac{\partial R}{\partial U}\Big|_{U^*} (U - U^*) + O(\|U - U^*\|^2, \|\delta\Psi\|\|U - U^*\|) \tag{3.29}$$

Again, the Jacobian is not known at the extrapolated system state, so expand the system equations in a Taylor series about U^* and use the result to eliminate the Jacobian

in Eq. 3.29:

$$R(U,\mu) = R(U^*,\mu) + \frac{\partial R}{\partial U}\Big|_{U^*}(U-U^*) + O(\|U-U^*\|^2) \tag{3.30}$$

$$J(U,\mu) = J(U^*,\mu) + \Psi_0^T R(U^*,\mu) + O(\|U-U^*\|^2, \|\delta\Psi\|\|U-U^*\|) \tag{3.31}$$

Finally, reintroduce the linear extrapolated system state. From Eq. 3.24 and Eq. 3.25 we can see that $\|U-U^*\|$ varies as $\|\delta\mu\|^2$. The resulting approximation is provided in Eq. 3.32 and demonstrates a leading error term of third order. The approximation requires the solution of the tangent linear equation, Eq. 3.5, in order to form the linear extrapolated system state U^*. All of the information to solve the tangent linear equations are obtained during the calculation of the sensitivity derivatives. Thus, building this surrogate is a relatively inexpensive process.

$$J(U,\mu) = J(U^*,\mu) + \Psi_0^T R(U^*,\mu) + O(\|\delta\mu\|^4, \|\delta\Psi\|\|\delta\mu\|^2) \tag{3.32}$$

3.4 Illustrative Example of Adjoint Solution

This section will present a detailed adjoint implementation for a one-dimensional heat conduction problem. In addition to providing the sensitivities a surrogate utilizing a single data point, produced using inputs taken at their mean values, is obtained to demonstrate the efficacy of an adjoint corrected surrogate that is accurate to a leading error of third order.

3.4.1 The Primal System

The problem considered is a one-dimensional heat conduction problem with uniform heat generation and radiative heat transfer at one face and an insulated boundary condition on the other, as illustrated by Eq. 3.33

$$k\frac{d^2T}{dx^2} = q \qquad x \in [0,L] \tag{3.33}$$

$$\frac{dT}{dx}\Big|_{x=0} = 0 \qquad -k\frac{dT}{dx}\Big|_{x=L} = \varepsilon\sigma(T^4(L) - T_\infty^4)$$

Utilizing linear finite elements, the discretization of Eq. 3.33 results in the system of equations shown in Eq. 3.34, where $h_{rad} = \varepsilon\sigma\left(T_N^2 + T_\infty^2\right)\left(T_N + T_\infty\right)$ and $\Delta x = \frac{L}{N-1}$.

$$R(T,\mu) = \begin{pmatrix} \frac{kT_1}{\Delta x} - \frac{kT_2}{\Delta x} - \frac{q\Delta x}{2} \\ -\frac{kT_1}{\Delta x} + 2\frac{kT_2}{\Delta x} - \frac{kT_3}{\Delta x} - q\Delta x \\ \vdots \\ -\frac{kT_{N-2}}{\Delta x} + 2\frac{kT_{N-1}}{\Delta x} - \frac{kT_N}{\Delta x} - q\Delta x \\ -\frac{kT_{N-1}}{\Delta x} + \left(\frac{k}{\Delta x} + h_{rad}\right)T_N - h_{rad}T_\infty - \frac{q\Delta x}{2} \end{pmatrix} = 0 \tag{3.34}$$

In the system, there are five parameters that are treated as normal random variables: the slab size has a standard deviation that is 30% of its mean value, the heat generation has a standard deviation that is 3% of its mean value, and the remaining parameters have standard deviations that vary by 10% of their mean values. These parameters and their distributions are given in Table 3.2.

Table 3.2: Example problem input parameters

	Parameter	mean	std. dev.
L	Dimension, m	0.05	0.015
q	Heat Geneneration, W/m^3	$7.2x10^4$	$2.16x10^3$
T_∞	Ambient Temperature, K	300.0	30.0
k	Thermal Conductivity, $W/m-K$	0.3	0.03
ε	Emissivity	0.5	0.05

3.4.2 The Adjoint System

In setting up the adjoint system we will be focusing on the peak temperature as the SRQ of interest, i.e. $J(T) = \max(T)$. The system Jacobian is given by Eq. 3.35.

$$\frac{\partial R}{\partial T} = \begin{pmatrix} \frac{k}{\Delta x} & -\frac{k}{\Delta x} & & & \\ -\frac{k}{\Delta x} & \frac{2k}{\Delta x} & -\frac{k}{\Delta x} & & \\ & \ddots & \ddots & \ddots & \\ & & -\frac{k}{\Delta x} & \frac{2k}{\Delta x} & -\frac{k}{\Delta x} \\ & & & -\frac{k}{\Delta x} & \left(\frac{k}{\Delta x} + 4\varepsilon\sigma T_N^3\right) \end{pmatrix} \tag{3.35}$$

As the SRQ is a specific point, each component of the $\partial J \partial T$ vector is given by Eq. 3.36.

$$\frac{\partial J}{\partial T_j} = \begin{cases} 1, & T_j = \|T\|_\infty \\ 0, & \text{otherwise} \end{cases} \tag{3.36}$$

Utilizing Eq. 3.35 and Eq. 3.36, the adjoint, Ψ, is calculated in Eq. 3.37. The resulting temperature profile and adjoint profile corresponding to $J(T)$ is shown in Fig. 3.1.

$$\left(\frac{\partial R}{\partial T}\right)^T \Psi = -\left(\frac{\partial J}{\partial T}\right)^T \tag{3.37}$$

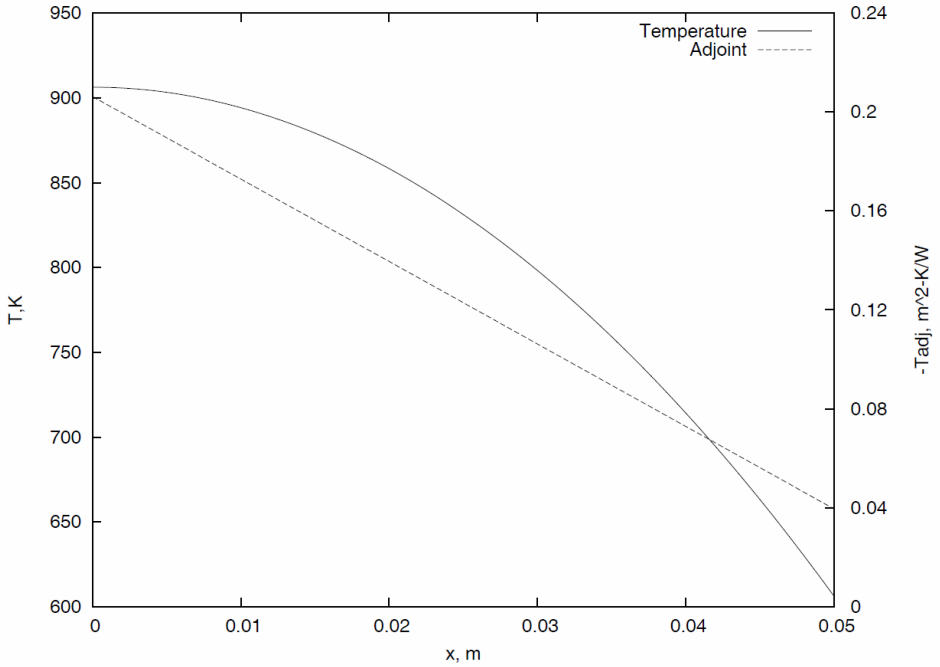

Figure 3.1: Temperature profile and adjoint for 1-D FEM example

3.4.3 Sensitivity Derivatives

To obtain sensitivity derivatives, we must obtain partial derivatives of the system equations with respect to each parameter. Note that the direct effect, $\partial J/\partial \mu_i$, vanishes for all input parameters.

$$\frac{\partial R}{\partial L} = \frac{1}{N-1}\begin{pmatrix} \frac{k}{\Delta x^2}(-T_1+T_2)-\frac{q}{2} \\ \frac{k}{\Delta x^2}(T_1-2T_2+T_3)-q \\ \vdots \\ \frac{k}{\Delta x^2}(T_{N-2}-2T_{N-1}+T_N)-q \\ \frac{k}{\Delta x^2}(T_{N-1}-T_N)-\frac{q}{2} \end{pmatrix} \tag{3.38}$$

$$\frac{\partial R}{\partial q} = \begin{pmatrix} \frac{-\Delta x}{2} & -\Delta x & \dots & -\Delta x & \frac{-\Delta x}{2} \end{pmatrix}^T \tag{3.39}$$

$$\frac{\partial R}{\partial T_\infty} = \begin{pmatrix} 0 & \dots & 0 & -4\varepsilon\sigma T_\infty^3 \end{pmatrix}^T \tag{3.40}$$

$$\frac{\partial R}{\partial k} = \begin{pmatrix} \frac{1}{\Delta x}(T_1 - T_2) \\ \frac{1}{\Delta x}(-T_1 + 2T_2 - T_3) \\ \vdots \\ \frac{1}{\Delta x}(-T_{N-2} + 2T_{N-1} - T_N) \\ \frac{1}{\Delta x}(-T_{N-1} + T_N) \end{pmatrix} \tag{3.41}$$

$$\frac{\partial R}{\partial \varepsilon} = \begin{pmatrix} 0 & \dots & 0 & \sigma\left(T_N^4 - T_\infty^4\right) \end{pmatrix}^T \tag{3.42}$$

Utilizing the adjoint solution, and the solutions to Eq. 3.38 through Eq. 3.42, we obtain the sensitivity derivatives using Eq. 3.10. These values are shown in Table 3.3.

Table 3.3: Sensitivity derivatives for example problem

μ	$\frac{dJ}{d\mu}$	$\frac{(dJ)/J}{(d\mu)/\mu}$
L	14849.4839	0.81928272
q	0.00614547	0.48824789
T_∞	0.12117430	0.04011291
k	-1000.0000	-0.33103483
ε	-284.9484	-0.15721307

3.4.3.1 Verification of Sensitivity Derivatives

An effective means of verifying the sensitivity derivatives, and hence verifying the adjoint solution is through the use of finite differences. Table 3.4 shows that the results from finite differences approach the exact sensitivity derivatives, obtained with the adjoint solution, with first order accuracy.

Table 3.4: Verification of adjoint solution

δL	δT_{max}	$\frac{\delta T_{max}}{\delta L}$	$\frac{(\delta T_{max})/T_{max}}{(\delta L)/L}$	$\frac{(\delta T_{max})/T_{max}}{(\delta L)/L}$ - $\left(\frac{(dJ)/J}{(dL)/L}\right)_{adj}$
0.00005000	0.74272400	14854.4799	0.81955836	0.00027564
0.00000500	0.07424992	14849.9834	0.81931028	0.00002756
0.00000050	0.00742477	14849.5338	0.81928547	0.00000275
0.00000005	0.00074248	14849.5058	0.81928392	0.00000120
δq	δT_{max}	$\frac{\delta T_{max}}{\delta q}$	$\frac{(\delta T_{max})/T_{max}}{(\delta q)/q}$	$\frac{(\delta T_{max})/T_{max}}{(\delta q)/q}$ - $\left(\frac{(dJ)/J}{(dq)/q}\right)_{adj}$
72.000	0.44242400	0.00614478	0.48819250	-0.00005539
7.200	0.04424692	0.00614541	0.48824235	-0.00000554
0.720	0.00442474	0.00614547	0.48824734	-0.00000055
0.072	0.00044247	0.00614547	0.48824783	-0.00000006
δT_∞	δT_{max}	$\frac{\delta T_{max}}{\delta T_\infty}$	$\frac{(\delta T_{max})/T_{max}}{(\delta T_\infty)/T_\infty}$	$\frac{(\delta T_{max})/T_{max}}{(\delta T_\infty)/T_\infty}$ - $\left(\frac{(dJ)/J}{(dT_\infty)/T_\infty}\right)_{adj}$
0.3000	0.03640358	0.12134525	0.04016950	0.00005659
0.0300	0.00363574	0.12119139	0.04011857	0.00000566
0.0030	0.00036353	0.12117601	0.04011348	0.00000057
0.0003	0.00003635	0.12117446	0.04011297	0.00000006
δk	δT_{max}	$\frac{\delta T_{max}}{\delta k}$	$\frac{(\delta T_{max})/T_{max}}{(\delta k)/k}$	$\frac{(\delta T_{max})/T_{max}}{(\delta k)/k}$ - $\left(\frac{(dJ)/J}{(dk)/k}\right)_{adj}$
0.0003000	-0.29970030	-999.00099900	-0.33070412	0.00033071
0.0000300	-0.02999700	-999.90000980	-0.33100172	0.00003311
0.0000030	-0.00299997	-999.99010300	-0.33103155	0.00000328
0.0000003	-0.00030000	-999.99785331	-0.33103411	0.00000072
$\delta \varepsilon$	δT_{max}	$\frac{\delta T_{max}}{\delta \varepsilon}$	$\frac{(\delta T_{max})/T_{max}}{(\delta \varepsilon)/\varepsilon}$	$\frac{(\delta T_{max})/T_{max}}{(\delta \varepsilon)/\varepsilon}$ - $\left(\frac{(dJ)/J}{(d\varepsilon)/\varepsilon}\right)_{adj}$
0.0005000	-0.14238201	-284.76402505	-0.15711135	0.00010172
0.0000500	-0.01424650	-284.92993740	-0.15720289	0.00001018
0.0000050	-0.00142473	-284.94654079	-0.15721205	0.00000102
0.0000005	-0.00014247	-284.94820006	-0.15721296	0.00000011

3.4.4 Uncertainty Quantification

The performance of the adjoint based surrogate, described in Section 3.3, is measured against brute force Monte-Carlo. The surrogate is built using Eq. 3.35 and Eq. 3.38 through Eq. 3.42. Utilizing the parameters given in Table 3.2, 100,000 cases are run using a 100 node model. The The Intel MKL Vector Statistical Library (VSL) is used to generate the random numbers. PDFs for the input parameters are shown in Fig. 3.2 and shows that the random number generator produces the expected distributions.

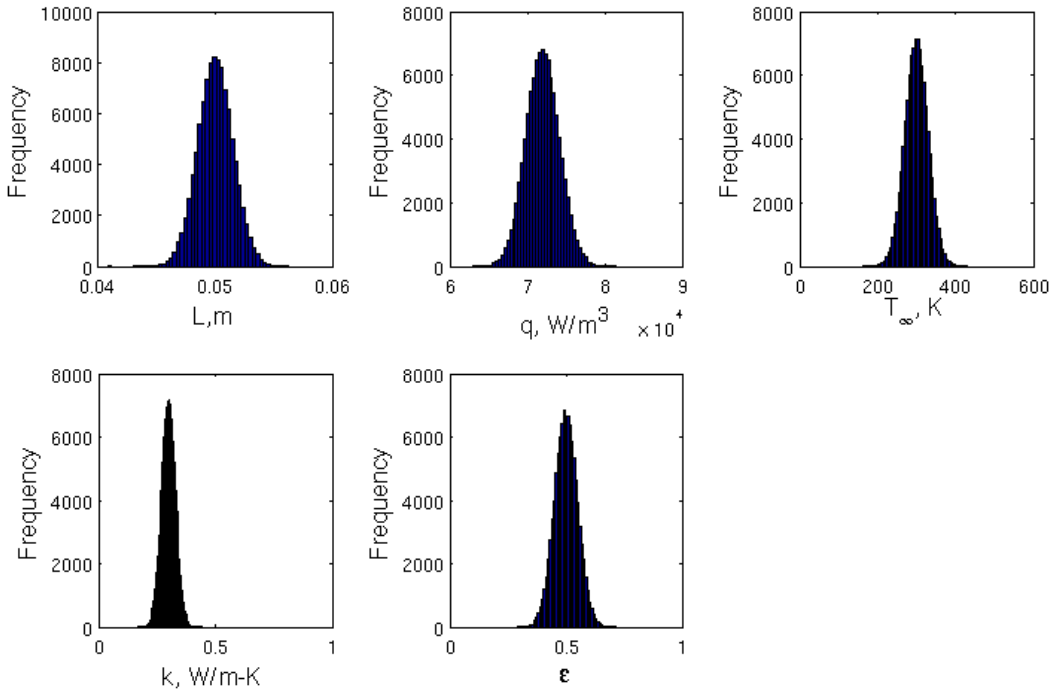

Figure 3.2: Input parameter PDFs for example problem

The results from the calculations are shown in Fig. 3.3 and Table 3.5. Fig. 3.3 shows that the surrogate reproduces the PDF well, with differences appearing at the tails of the distribution. Looking at the resulting values in Table 3.5, the surrogate appears to slightly under-predict the true mean, but is in agreement with the peak temperature obtained by using mean parameter values.

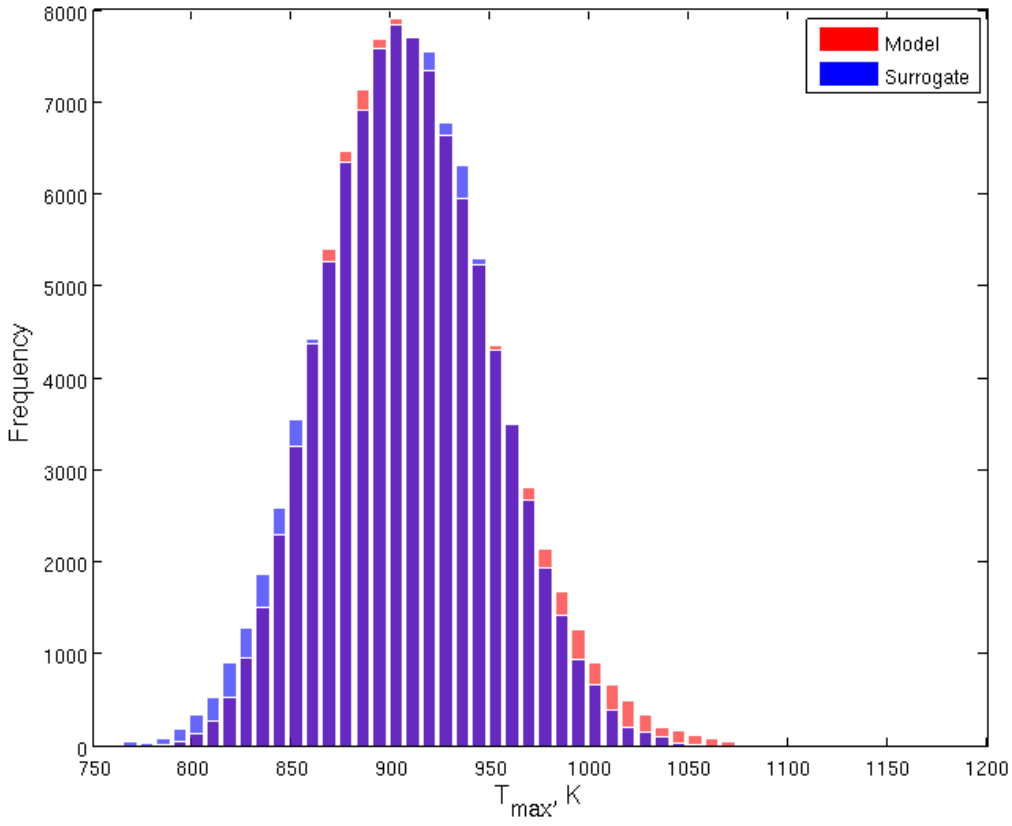

Figure 3.3: Model and surrogate produced PDFs for example problem

Table 3.5: Output from example UQ problem

	mean(T_{max}), K	std. dev., K	Run-time, s
Model	910.9573	43.5512	15,076
Surrogate	906.5864	42.2997	20
Base	906.2491	-	-

Overall, the quality of information produced by the surrogate is a good representation of the uncertainty present in the model, however, using only a single point in building the surrogate does not capture extremes of the distribution and more points should be utilized.

The results demonstrate significant speed-up of the sampling process. The cases were run on a 300 GHz Intel Core CPU desktop computer with 8.0 GB of RAM. The run-time required to solve the primal and adjoint equations, build the surrogate, and run 100,000 samples on the surrogate was approximately 20 seconds. This is over two orders of magnitude faster than sampling the true function.

3.5 Combining Multiple Surrogate Functions

The previous example demonstrated that using only the mean input parameter values when building the surrogate may not be sufficient. This situation can be exacerbated in scenarios where the SRQ has a spatial or temporal dependence, e.g. perturbing the input parameters may change the location or time at which the peak temperature is observed. To cope with such a scenario and to increase the accuracy, multiple surrogate functions can be combined.

The method for combining multiple surrogate functions is to first produce several surrogates via a Latin hypercube sampling [90], then select the surrogate that maps to nearest SRQ. A sensitivity weighted distance function, given by Eq. 3.43 where the subscript i refers to the input parameter and j refers to a specific surrogate, accomplishes this. This method is explored in detail in the following chapter which investigates multiple aspects of the High Temperature Test Reactor (HTTR).

$$d_j = \Big[\sum_i \Big(\frac{dJ}{d\mu_{i,j}}(\mu_i - \mu_{i,j})\Big)^2\Big]^{1/2} \tag{3.43}$$

CHAPTER 4

Adjoint Implementation

4.1 Introduction

This chapter ties the thesis together by discussing the details of the adjoint implementation into a larger system code, namely AGREE, and is broken up into two sections. First, the steps for the implementation are discussed, then the adjoint and adjoint corrected surrogate are used to investigate various aspects of the HTTR. The cases consist of the bypass flow test of Kaburaki and Takizuka [69], the HENDEL facility heat transfer experiment [91], and a model of the HTTR itself.

4.2 Modifications to AGREE

The formation of the adjoint, as outlined in Ch. 3, requires the formation of the Jacobian. The formation of the Jacobian is the step in the process that required the most amount of code development. As the Jacobian is based on a residual vector produced by the system of equations, the solution algorithm needs to be investigated.

The original solution algorithm in AGREE utilized the segregated SIMPLE algorithm of Patankar [45], which is shown in Fig. 4.1. In this algorithm the primary variables constitute the velcoity field, the pressure field, and the temperature fields for both the solid and fluid. For the construction of the coupled system of equations, and hence the Jacobian, the system of equations is arranged as in Eq. 4.1, where the system state is given by Eq. 4.2. Note that the system state variables remain the same, but the pressure correction equation from the SIMPLE algorithm is replaced by the original continuity equation.

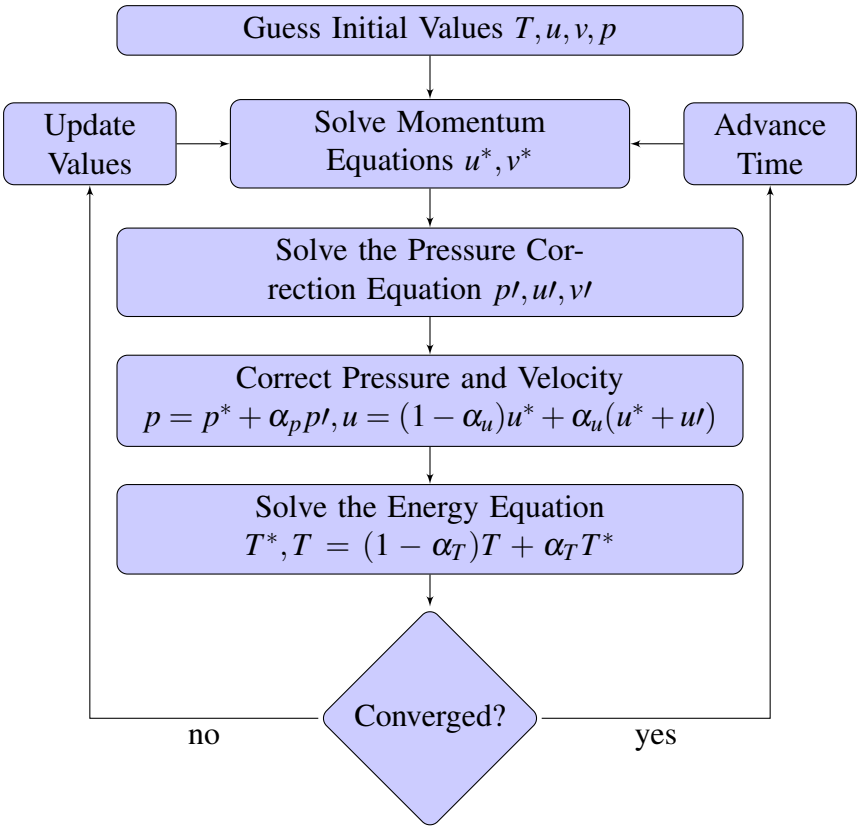

Figure 4.1: SIMPLE algorithm for AGREE solver/pre-conditioner

$$R(U,\mu) = \begin{bmatrix} \begin{bmatrix} \vdots \\ \text{momentum} \\ \vdots \end{bmatrix} \\ \begin{bmatrix} \vdots \\ \text{continuity} \\ \vdots \end{bmatrix} \\ \begin{bmatrix} \vdots \\ \text{solid energy} \\ \vdots \end{bmatrix} \\ \begin{bmatrix} \vdots \\ \text{fluid energy} \\ \vdots \end{bmatrix} \end{bmatrix} = 0 \tag{4.1}$$

$$U^T = \left[u_1 \dots u_L, v_1 \dots v_M, p_1 \dots p_N, T_{s,1} \dots T_{s,P}, T_{f,1} \dots T_{f,N}\right]^T \tag{4.2}$$

In setting up the Jacobian there are some tools that are available to perform automatic differentiation such as ADIFOR [92] and Tapenade [93]. Automatic differentiation is an active area of research and due to the lack of familiarity with these tools, it was decided that the most efficient method was hand differentiation of the code. In performing the hand differentiation it is required that derivatives of all the constitutive relationships with respect to the system state variables (i.e. the field velocities, pressures, and temperatures) be available. Most of these derivatives are trivial, however, the major friction loss term and the branching model, described in Chapter 2, have been given special attention in the appendices. Verification of the Jacobian matrix was completed by performing a term by term inspection via finite differencing.

With the Jacobian matrix obtained, the efficiency of the solver can be improved by utilizing the Newton-Raphson method for solving non-linear systems [94]. It it known that the Newton method requires preconditioning. For this preconditioning, the SIMPLE algorithm is retained as a physics-based preconditioner. Since the SIMPLE algorithm updates the solution with continuity-satisfying pressure fields, the velocity field tends to converge quickly [45]. The pressure field, however, lags behind due to the neglected terms in the pressure correction equation. It is the treatment of these neglected terms where the SIMPLEC and SIMPLER can make improvements in convergence [46]. Coupling the SIMPLE algorithm with a Newton solver, however, produces a very good pair as only a few SIMPLE iterations (approximately ten) are sufficient to precondition the system. This system is then

converged with only a few Newton iterations. A comparison of the preconditioned coupled solver against the segregated SIMPLE solver is provided in Table 4.1 which demonstrates roughly a factor of 5 speedup for the coupled Newton solver. All cases were iterated down to the default (10^{-9}) residuals and utilized the default under-relaxation factors selected for the SIMPLE algorithm ($\alpha_{u,v} = 0.5$, $\alpha_p = 0.2$, $\alpha_T = 0.5$).

The remaining modifications are specific to each SRQ that is to be investigated and will be handled in the sections that follow.

Table 4.1: Preconditioned Newton-Raphson vs SIMPLE algorithm

Case	Size	Solver	Precond It.	Sol. It.	time (s)
KT	1,546	SIMPLE	-	111	0.53
		Newton	5	2	0.16
HENDEL	11,110	SIMPLE	-	92	11.1
		Newton	10	3	2.1
HTTR	72,780	SIMPLE	-	82	145.7
		Newton	10	4	33.8

4.3 Kaburaki and Takizuka

The bypass flow test facility of Kaburaki and Takizuka is one of the fluids validation cases presented in Chapter 2. In this section the test is used to demonstrate the UQ and sensitivity analysis features added to the AGREE code.

4.3.1 Bypass Flow SRQ

The SRQ of interest for this test is the bypass flow, or the percentage of the total flow that does not enter the main coolant channels in the test apparatus. This quantity is expressed by Eq. 4.3, where W refers to the mass-flow rate. The components of the vector $\frac{dJ}{dU}$ are derived as follows, where the subscripts b and c refer to junctions connecting bypass flow-paths and main coolant flow-paths, respectively, and the subscripts iv and ov refer to inlet and outlet volumes of the respective junctions. In the equations below, the quantities $\frac{d\rho}{d\rho_{iv,ov}}$ are obtained using the extrapolated densities discussed in Chapter 2 and the property derivatives, $\frac{d\rho}{dp}$ and $\frac{d\rho}{dT}$, are obtained from the equations of state.

$$J = \frac{W_{bypass}}{W_{bypass} + W_{cool}} \tag{4.3}$$

$$\frac{dJ}{dW_{bypass}} = \frac{J}{W_{bypass}} - \frac{J}{W_{bypass} + W_{cool}} \tag{4.4}$$

$$\frac{dJ}{dW_{cool}} = \frac{J}{W_{cool}} \tag{4.5}$$

$$\frac{dW}{du} = \rho A \tag{4.6}$$

$$\frac{dW}{d\rho} = uA \tag{4.7}$$

$$\boxed{\frac{dJ}{du_c} = \frac{dJ}{dW_{cool}} \frac{dW_{cool}}{du_c}} \tag{4.8}$$

$$\boxed{\frac{dJ}{du_b} = \frac{dJ}{dW_{bypass}} \frac{dW_{bypass}}{du_b}} \tag{4.9}$$

$$\boxed{\frac{dJ}{dp_{iv}} = \sum_c \frac{dJ}{dW_{cool}} \frac{dW_{cool}}{d\rho} \frac{d\rho}{d\rho_{iv}} \left(\frac{d\rho}{dp}\right)_{iv} + \sum_b \frac{dJ}{dW_{bypass}} \frac{dW_{bypass}}{d\rho} \frac{d\rho}{d\rho_{iv}} \left(\frac{d\rho}{dp}\right)_{iv}} \tag{4.10}$$

$$\boxed{\frac{dJ}{dT_{iv}} = \sum_c \frac{dJ}{dW_{cool}} \frac{dW_{cool}}{d\rho} \frac{d\rho}{d\rho_{iv}} \left(\frac{d\rho}{dT}\right)_{iv} + \sum_b \frac{dJ}{dW_{bypass}} \frac{dW_{bypass}}{d\rho} \frac{d\rho}{d\rho_{iv}} \left(\frac{d\rho}{dT}\right)_{iv}} \tag{4.11}$$

$$\boxed{\frac{dJ}{dp_{ov}} = \sum_c \frac{dJ}{dW_{cool}} \frac{dW_{cool}}{d\rho} \frac{d\rho}{d\rho_{ov}} \left(\frac{d\rho}{dp}\right)_{ov} + \sum_b \frac{dJ}{dW_{bypass}} \frac{dW_{bypass}}{d\rho} \frac{d\rho}{d\rho_{ov}} \left(\frac{d\rho}{dp}\right)_{ov}} \tag{4.12}$$

$$\boxed{\frac{dJ}{dT_{ov}} = \sum_c \frac{dJ}{dW_{cool}} \frac{dW_{cool}}{d\rho} \frac{d\rho}{d\rho_{ov}} \left(\frac{d\rho}{dT}\right)_{ov} + \sum_b \frac{dJ}{dW_{bypass}} \frac{dW_{bypass}}{d\rho} \frac{d\rho}{d\rho_{ov}} \left(\frac{d\rho}{dT}\right)_{ov}} \tag{4.13}$$

4.3.2 Sensitivity Analysis and Adjoint Verification

For the analysis of the Kaburaki and Takizuka experiment the boundary conditions, junction form loss coefficients, and crossflow gap loss coefficient and width are investigated for their impact on bypass flow. For this study, the experiment is modeled using 1/6 symmetry. The input parameters and their associated sensitivities are provided in Table 4.2 , where the input parameters have been ordered in terms of the largest impact on bypass flow to the smallest.

Table 4.2: Input parameters and sensitivities for the Kaburaki and Takizuka bypass flow test

SRQ, J				
BYPASS	10.73%			
Input Parameters, μ				
ID	Description	Value	$\frac{dJ}{d\mu}$	$\frac{dJ/J}{d\mu/\mu}$
J1-W	Inlet Mass-flow Rate BC	0.030333 kg/s	1.7976E+00	5.0807E-01
G1-W	Crossflow Gap Width	0.001 m	2.7989E+01	2.6080E-01
G1-K	Crossflow Gap Loss Coef.	3.702262	-3.9650E-03	-1.3678E-01
ATMTC1-K	Junction Loss Coef.	0.5	2.0948E-02	9.7594E-02
C1TC2-K	Junction Loss Coef.	0.3	2.1026E-02	5.8775E-02
C2TN1-K	Junction Loss Coef.	0.15	2.1077E-02	2.9459E-02
EXC-P	Outlet Pressure BC	96320.0 Pa	-1.7740E-08	-1.5921E-02
ATMTB1-K	Junction Loss Coef.	0.5	-2.7560E-03	-1.2840E-02
C3TC4-K	Junction Loss Coef.	0.3	-1.8447E-05	-5.1567E-05
N1TC3-K	Junction Loss Coef.	0.15	-1.8356E-05	-2.5656E-05

In order to verify the correct implementation of the adjoint solution, the sensitivity derivatives are obtained via a finite difference and compared against the values obtained via the adjoint solution. Assuming the adjoint based sensitivity derivatives to be exact, the finite differenced sensitivity derivatives, shown in Table 4.3, demonstrate the expected first order accuracy.

Table 4.3: Verification of adjoint based sensitivity derivatives in bypass flow experiment

ID	Value, μ	Bypass Flow, J	$\frac{\Delta J}{\Delta \mu}$	Error
J1-W	0.0333663	0.11152	1.3846E+00	-3.4576E-01
	0.0306363	0.10784	1.7170E+00	-1.3348E-02
	0.0303633	0.10737	1.7291E+00	-1.2767E-03
G1-W	0.00200	0.12028	1.2964E+01	-1.6025E+01
	0.00110	0.10995	2.6262E+01	-2.7269E+00
	0.00101	0.10761	2.8697E+01	-2.9168E-01
G1-K	7.491030	0.09538	-3.1520E-03	7.6301E-04
	4.077635	0.10588	-3.8210E-03	9.4046E-05
	3.739761	0.10717	-3.9054E-03	9.6127E-06
ATMTC1-K	0.750	0.11237	2.0223E-02	-4.6120E-04
	0.550	0.10835	2.0596E-02	-8.7994E-05
	0.505	0.10742	2.0675E-02	-8.7461E-06
C1TC2-K	0.6	0.11337	2.0186E-02	-5.7552E-04
	0.33	0.10794	2.0707E-02	-5.3847E-05
	0.303	0.10738	2.0756E-02	-5.3669E-06
C2TN1-K	0.3	0.11040	2.0548E-02	-2.6375E-04
	0.165	0.10763	2.0786E-02	-2.5700E-05
	0.1515	0.10735	2.0809E-02	-2.5653E-06
EXC-P	105952.0	0.10717	-1.5376E-08	2.1406E-09
	97283.2	0.10730	-1.7279E-08	2.3682E-10
	96416.32	0.10732	-1.7492E-08	2.3934E-11
ATMTB1-K	0.75	0.10665	-2.6906E-03	3.0608E-05
	0.55	0.10718	-2.7150E-03	6.1790E-06
	0.505	0.10731	-2.7206E-03	6.1920E-07
C3TC4-K	0.6	0.10731	-1.8104E-05	1.1109E-07
	0.33	0.10732	-1.8204E-05	1.1170E-08
	0.303	0.10732	-1.8214E-05	1.1176E-09
N1TC3-K	0.3	0.10732	-1.8056E-05	6.8647E-08
	0.165	0.10732	-1.8118E-05	6.8911E-09
	0.1515	0.10732	-1.8124E-05	6.8928E-10

4.3.3 Surrogate Verification and UQ

The surrogate implementation is verified by comparing the surrogate predicted values against the values determined by the code. Table 4.4 shows the expected third order accuracy predicted by the derivation in Ch. 3. As the sensitivity derivatives for C3TC4-K (coolant channel 3 to coolant channel 4 form loss coefficinet) and N1TC3-K (node 1 to coolant channel 3 form loss coefficient) are negligable, i.e. a 10% change in these values results in a change in bypass flow that is $\sim 1E-6$, these sensitivity derivatives are not included in the surrogate verification or UQ evaluation.

Table 4.4: Verification of third order accuracy for surrogate

ID	Value, μ	Bypass, J	Lin. Int.	Error	Surrogate	Error
J1-W	0.0333663	0.11152	0.1126	1.05E-03	0.1112	-3.06E-04
	0.0306363	0.10784	0.1078	4.05E-06	0.1078	8.93E-09
	0.0303633	0.10737	0.1074	3.87E-08	0.1074	1.24E-11
G1-W	0.00200	0.12028	0.1363	1.60E-02	0.0867	-3.35E-02
	0.00110	0.10995	0.1102	2.73E-04	0.1099	-3.04E-05
	0.00101	0.10761	0.1076	2.92E-06	0.1076	-3.14E-08
G1-K	7.491030	0.09538	0.0925	-2.89E-03	0.0960	5.80E-04
	4.077635	0.10588	0.1058	-3.53E-05	0.1059	7.70E-07
	3.739761	0.10717	0.1072	-3.60E-07	0.1072	7.87E-10
ATMTC1-K	0.750000	0.11237	0.1125	1.15E-04	0.1124	-4.39E-06
	0.550000	0.10835	0.1084	4.40E-06	0.1083	-2.82E-08
	0.505000	0.10742	0.1074	4.37E-08	0.1074	-2.74E-11
C1TC2-K	0.6	0.11337	0.1135	1.73E-04	0.1134	-8.45E-06
	0.33	0.10794	0.1079	1.62E-06	0.1079	-6.17E-09
	0.303	0.10738	0.1074	1.61E-08	0.1074	-6.08E-12
C2TN1-K	0.3	0.11040	0.1104	3.96E-05	0.1104	-7.93E-07
	0.165	0.10763	0.1076	3.86E-07	0.1076	-7.02E-10
	0.1515	0.10735	0.1074	3.85E-09	0.1074	-7.02E-13
EXC-P	105952	0.10717	0.1072	-2.06E-05	0.1072	4.38E-05
	97283.2	0.10730	0.1073	-2.28E-07	0.1073	4.44E-08
	96416.32	0.10732	0.1073	-2.31E-09	0.1073	4.44E-11
ATMTB1-K	0.75	0.10665	0.1066	-7.65E-06	0.1066	7.72E-08
	0.55	0.10718	0.1072	-3.09E-07	0.1072	6.23E-10
	0.505	0.10731	0.1073	-3.10E-09	0.1073	6.20E-13

For the UQ evaluation, the input parameters are sampled over the ranges given in Table 4.5. The ranges are chosen conservatively as the purpose of the UQ evaluation is a demonstration of the method. Thus a larger input range results in a more challenging calculation for the surrogate. Furthermore, details regarding uncertainties in the gap geometry and many of the form loss coefficients are known with little certainty or have been obtained by fitting data from the experiment.

Table 4.5: Input values and range for bypass flow UQ

ID	uncertainty	lower bounds	upper bounds
J1-W	$\pm 4\%$	$0.02912\,kg/s$	$0.031546\,kg/s$
ATMTC1-K	± 0.1	0.4	0.6
C1TC2-K	± 0.1	0.2	0.4
C2TN1-K	± 0.05	0.1	0.2
ATMTB1-K	± 0.1	0.4	0.6
G1-K	$\pm 50\%$	1.851	5.553
G1-W	$\pm 0.0005\,m$	$0.0005\,m$	$0.0015\,m$
EXC-P	$\pm 4\%$	$92467.2\,Pa$	$100172.8\,Pa$

To build the surrogate, DAKOTA is used to run 100 cases utilizing Latin-Hypercube sampling. The associated adjoint, residual, and sensitivity information from the 100 cases are stored in a surrogate library. The value of 100 was chosen as it is approximately the number of the runs that one would perform in a Wilks' based UQ evaluation. The range of the sensitivity derivatives are shown in Fig. 4.2 and demonstrate that the local sensitivty derivatives can vary substantially over input space. The order of magnitude, however, remains relatively constant. With the surroage library built, 50,000 cases are run in an effort to exhaustively sample the input space. As the Kaburaki and Takizuka test case runs quickly, both the true function and the surrogate are sampled and compared against each other in Table 4.6 and Fig. 4.3. From the results it is apparent that even with a conservative range placed on the inputs, the surroage captures the PDF of the true function as well as range of all possible outcomes. Due to the epistemic nature of the uncertainty, this analysis can only state that the bypass flowrate is $9.75\% \pm 2.65\%$.

Table 4.6: Kaburaki and Takizuka UQ, bypass flow true function and surroage

	Sample Size	Processors	Total Wall Clock, s	Min. Val.	Max. Val
True Func.	50,000	8	7882	7.08475%	12.41725%
Surrogate	50,000	8	1965	7.08542%	12.41736%

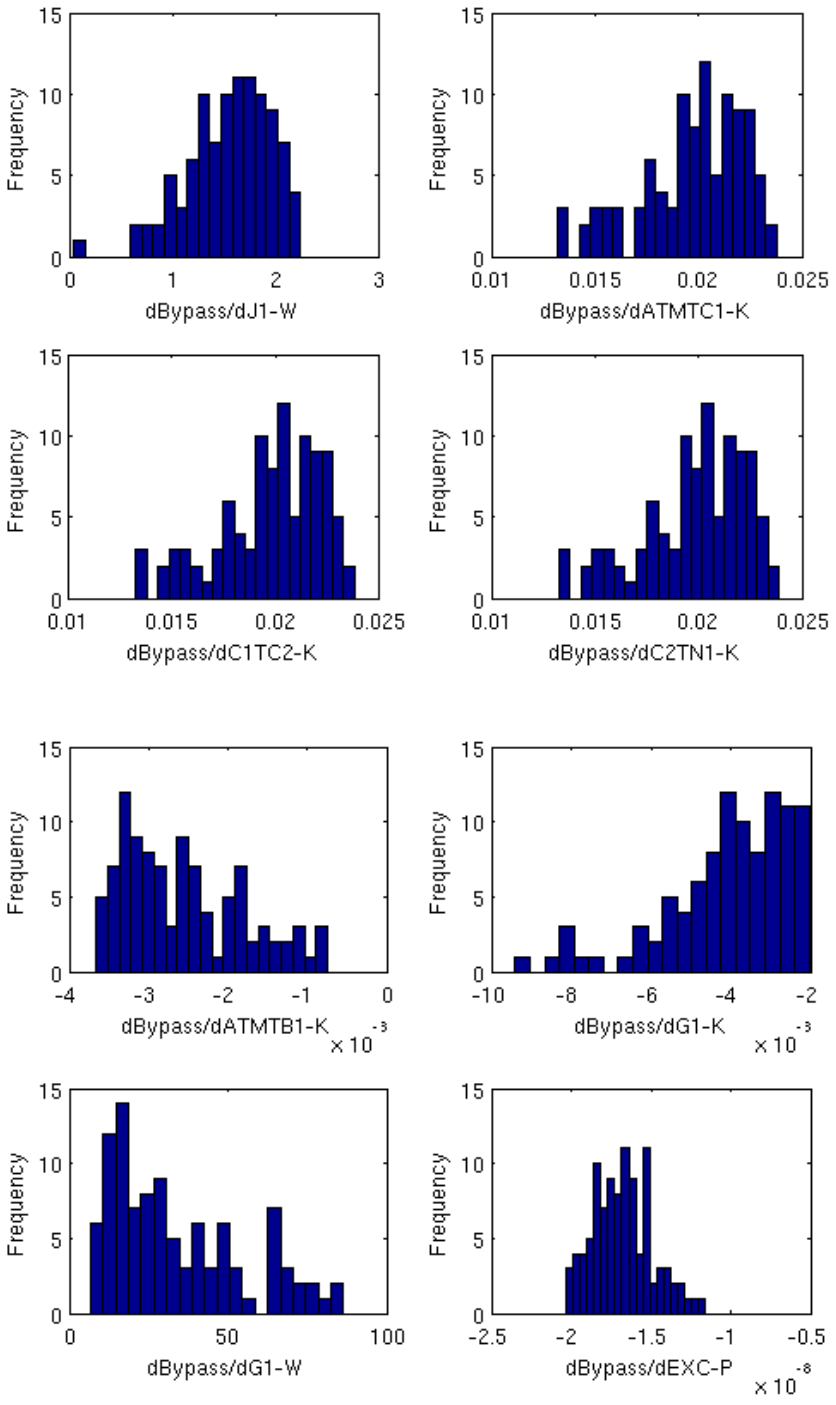

Figure 4.2: Distribution of sensitivity derivatives used in surrogate for Kaburaki and Takizuka test

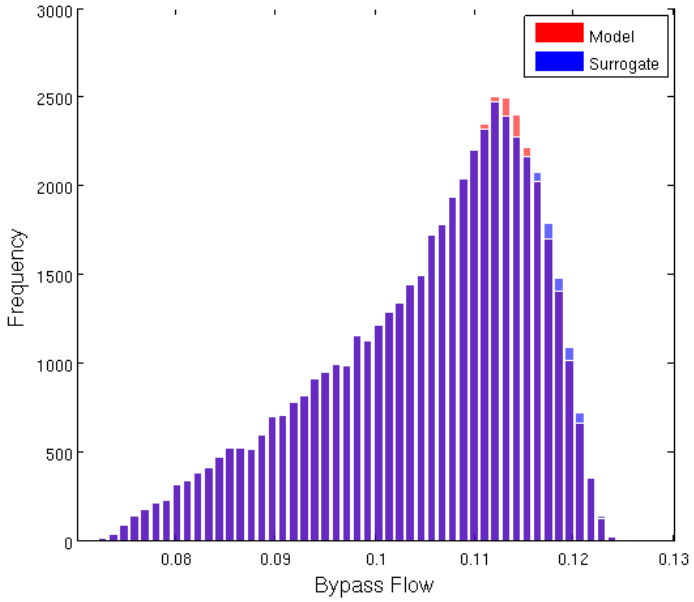

Figure 4.3: Histogram of bypass flow for Kaburaki and Takizuka test

4.4 HENDEL Heat Transfer Experiment

HENDEL (Helium Engineering Demonstration Loop) was constructed for large scale tests to support the design of the HTTR components, such as pin-in-hole fuel column, and has been used to validate the heat transfer modeling in AGREE [39]. The dimensions of the graphite block are the same as those used for the HTTR with electrically heated rods used to simulate the fuel. Seven graphite blocks are stacked to simulate the active core of the HTTR with a crossflow gap introduced between blocks 3 and 4, see Fig. 4.4. Similar to the Kaburaki and Takizuka bypass flow test, the bypass flowpath is sealed at the bottom. The AGREE prediction of bypass flow for the HENDEL facility is compared against experimental data in Table 4.7, and temperature profiles for HENDEL test 2311 are provided in Fig. 4.5. These results demonstrate the accuracy of the modeling in the AGREE code. The remainder of this section will investigate the impact of the input parameters on the average macroscopic core temperature and the peak temperature observed within the core.

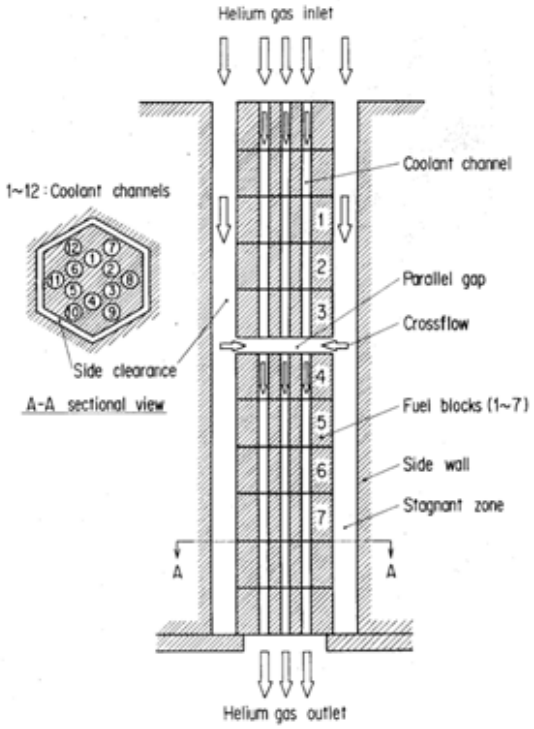

Figure 4.4: HENDEL multi-channel test with crossflow

Table 4.7: AGREE prediction of bypass flow in HENDEL facility with comparison to experimental data

Test	Re at Cool Channel Inlet	Exp.	AGREE
2308	3240	56.0%	56.0%
2311	2280	56.1%	54.5%
2314	1110	57.5%	55.3%
2317	4440	56.4%	56.8%

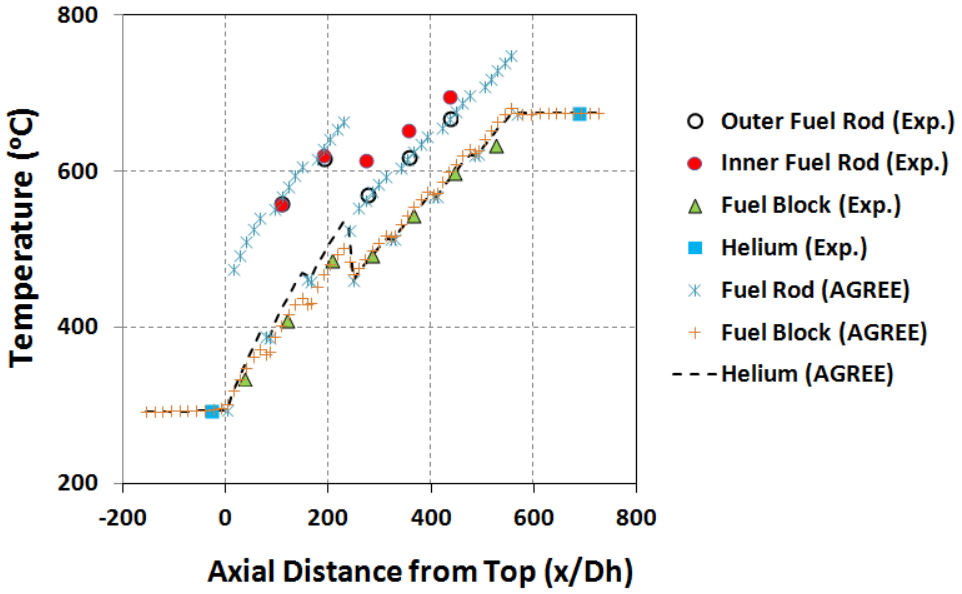

Figure 4.5: AGREE prediction of temperature profile for HENDEL test 2311 with comparison to experimental data

4.4.1 Average Macroscopic Temperature SRQ

The average macroscopic temperature is selected a SRQ as this is representative of the total amount of thermal energy stored within the core. This quantity is expressed by Eq. 4.14. For the cases investigated in this thesis the solid density is invariant and the components of the $\frac{dJ}{dU}$ vector simplify to Eq. 4.15. The sensitivites of the average macroscopic temperature are stated in Table 4.8 where they have been arranged in order of significance. Adjoint verification is provided in Appendix C. It is noted that the crossflow gap parameters have negligable impact on the average core temperature.

$$T_{MAC} = \frac{\sum_i \rho_i T V_i}{\sum_i \rho_i V_i} \tag{4.14}$$

$$\frac{T_{MAC}}{dU_i} = \frac{\rho_i V_i}{\sum_i \rho_i V_i} \tag{4.15}$$

Table 4.8: Input parameters and sensitivities for HENDEL test 2311, average macroscopic temperature

SRQ, J				
T_{MAC}	719.40 K			
Input Parameters, μ				
ID	Description	Value	$\frac{dJ}{d\mu}$	$\frac{dJ/J}{d\mu/\mu}$
$T_{BC,in}$	Inlet Temperature BC	573.35 K	1.0088E+00	8.04E-01
W_{in}	Inlet mass flow rate	0.20 kg/s	-7.3740E+02	-2.05E-01
h_G	Gnielinski HTC (Avg.)	697.23 $\frac{W}{m^2-K}$	-3.0134E-03	-2.92E-03
h_{J-90}	JAEA-90 HTC (Avg.)	576.24 $\frac{W}{m^2-K}$	-2.6827E-03	-2.15E-03
$k_{graphite}$	Block Th-Cond. (Avg.)	51.09 $\frac{W}{m-k}$	-2.1683E-02	-1.54E-03
GB-W	Crossflow Gap Width	0.002 m	3.0717E+02	8.54E-04
GB-K	Crossflow Gap Loss Coef.	3.410	-9.0080E-02	-4.27E-04
P_{out}	Outlet Pressure BC	2.0E6 Pa	-2.4059E-09	-6.69E-06
k_{heat}	Heater Rod Th-Cond.	10.0 $\frac{W}{m-l}$	6.7666E-05	9.4058E-07

For the UQ evaluation, the significant input parameters are sampled over the ranges given in Table 4.9. To build the surrogate, DAKOTA is used to run 100 cases utilizing Latin-Hypercube sampling. The associated adjoint, residual, and sensitivity information from the 100 cases are stored in a surrogate library. The range of the sensitivity derivatives are shown in Fig. 4.6. With the surroage library built, 50,000 cases are run in an effort to exhaustively sample the input space. The output, provided in Fig. 4.7, demonstrates a relatively flat distribution. Due to the epistemic nature of the uncertainty, this analysis can only state that the average macroscopic temperature is $719.7 \pm 23.3\,K$ (3.2% uncertainty).

Table 4.9: Input values and range for HENDEL test 2311, average macroscopic temperature

ID	uncertainty	lower bounds	upper bounds
$k_{graphite}$	$\pm 10\%$	$-5.1\frac{W}{mK}$ bias	$+5.1\frac{W}{mK}$ bias
$T_{BC,in}$	$\pm 3\%$	$-17.2\,K$ bias	$+17.2\,K$ bias
h_{J-90}	$\pm 12\%$	$-70.0\frac{W}{m^2K}$ bias	$+70.0\frac{W}{m^2K}$ bias
h_G	$\pm 12\%$	$-84.0\frac{W}{m^2K}$ bias	$+84.0\frac{W}{m^2K}$ bias
W_{in}	$\pm 4\%$	$0.192\,kg/s$	$0.208\,kg/s$

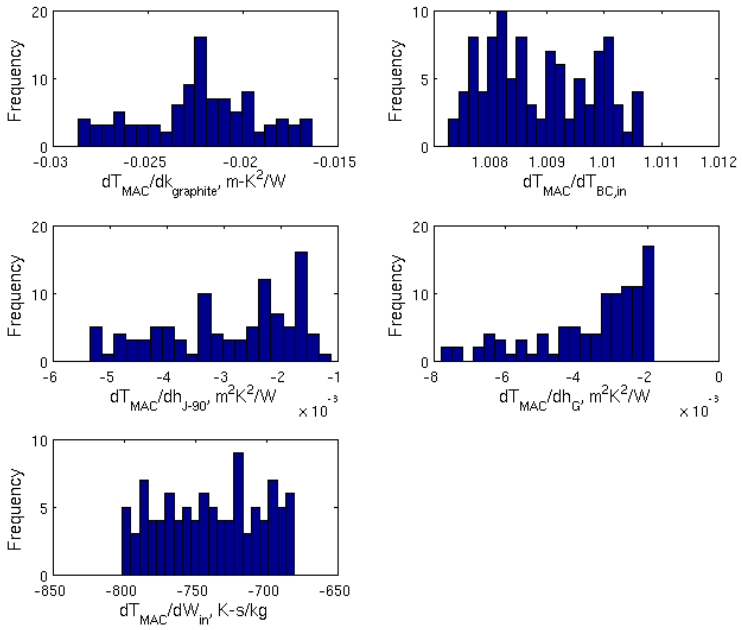

Figure 4.6: Distribution of sensitivity derivatives used in surrogate for HENDEL test 2311 average macroscopic temperature

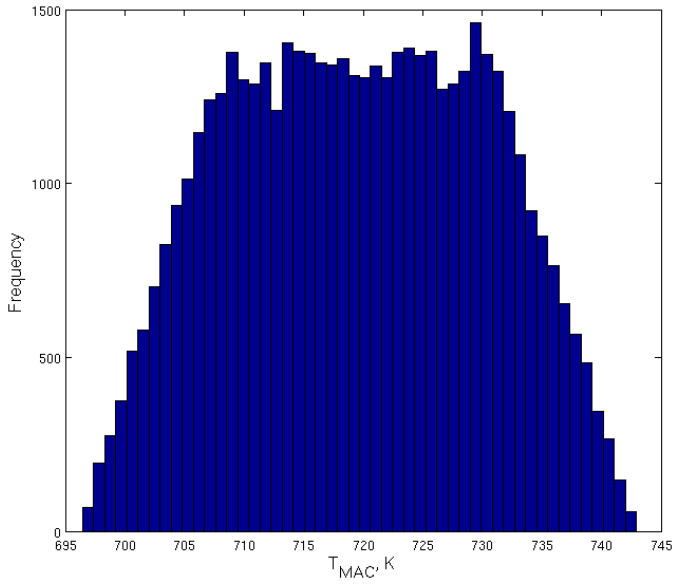

Figure 4.7: Histogram of average macroscopic temperature from HENDEL test 2311

4.4.2 Peak Temperature

The peak temperature is selected a SRQ as this quantity is critical in ensuring the integrity of the fuel. As this quantity represented as a single point, the $\frac{dJ}{dU}$ vector is trivial and is given by Eq. 4.16. The sensitivites of the average macroscopic temperature are stated in Table 4.8 where they have been arranged in order of significance. Adjoint verification is provided in Appendix C. It is noted that the crossflow gap parameters have negligable impact on the peak temperature.

$$\frac{dT_{MAX}}{\partial T_i} = \begin{cases} 1, & T_i = \|T\|_\infty \\ 0, & \text{otherwise} \end{cases} \tag{4.16}$$

Table 4.10: Input parameters and sensitivities for HENDEL test 2311, peak temperature

SRQ, J				
T_{MAX}	980.59 K			
Input Parameters, μ				
ID	Description	Value	$\frac{dJ}{d\mu}$	$\frac{dJ/J}{d\mu/\mu}$
$T_{BC,in}$	Inlet Temperature BC	573.35 K	9.7383E-01	5.69E-01
W_{in}	Inlet mass flow rate	0.200 kg/s	-1.5638E+03	-3.19E-01
k_{heat}	Heater Rod Th-Cond.	10.0 $\frac{W}{m-l}$	-6.2161E+00	-6.34E-02
h_{J-90}	JAEA-90 HTC (Avg.)	576.24 $\frac{W}{m^2-K}$	-5.4526E-02	-3.20E-02
$k_{graphite}$	Block Th-Cond. (Avg.)	51.09 $\frac{W}{m-k}$	-2.1168E-01	-1.10E-02
h_G	Gnielinski HTC (Avg.)	697.23 $\frac{W}{m^2-K}$	-2.9028E-04	-2.06E-04
$P_{BC,out}$	Outlet Pressure BC	2.0E6 Pa	-3.9527E-08	-8.06E-05
GB-W	Crossflow Gap Width	0.002 m	-5.1085E-01	-1.04E-06
GB-K	Crossflow Gap Loss Coef.	3.410	1.4981E-04	5.21E-07

For the UQ evaluation, the significant input parameters are sampled over the ranges given in Table 4.11. To build the surrogate, DAKOTA is used to run 100 cases utilizing Latin-Hypercube sampling. The associated adjoint, residual, and sensitivity information from the 100 cases are stored in a surrogate library. The range of the sensitivity derivatives are shown in Fig. 4.8. With the surroage library built, 50,000 cases are run in an effort to exhaustively sample the input space. The output, provided in Fig. 4.9, demonstrates a relatively normal distribution. Due to the epistemic nature of the uncertainty, this analysis can only state that the peak temperature is $982.7 \pm 37.5\,K$ (3.8% uncertainty).

Table 4.11: Input values and range for HENDEL test 2311, peak temperature

ID	uncertainty	lower bounds	upper bounds
$T_{BC,in}$	$\pm 3\%$	$-17.2\,K$ bias	$+17.2\,K$ bias
W_{in}	$\pm 4\%$	$0.192\,kg/s$	$0.208\,kg/s$
k_{heat}	$\pm 10\%$	$-1.0\frac{W}{mK}$ bias	$1.0\frac{W}{mK}$ bias
h_{J-90}	$\pm 12\%$	$-70.0\,\frac{W}{m^2K}$ bias	$+70.0\,\frac{W}{m^2K}$ bias
$k_{graphite}$	$\pm 10\%$	$-5.1\frac{W}{mK}$ bias	$+5.1\frac{W}{mK}$ bias

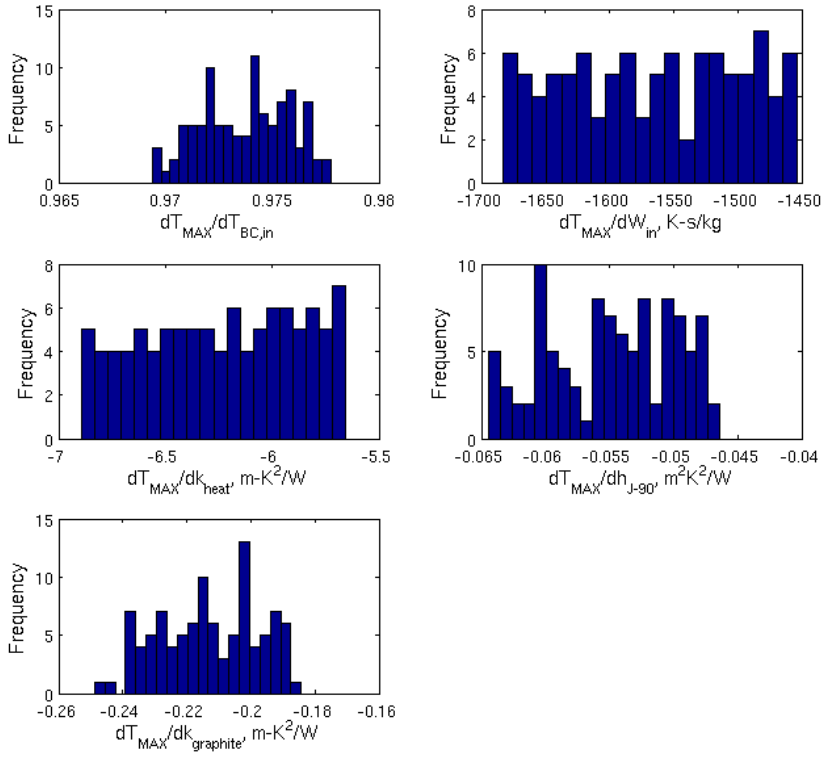

Figure 4.8: Distribution of sensitivity derivatives used in surrogate for HENDEL test 2311 peak temperature

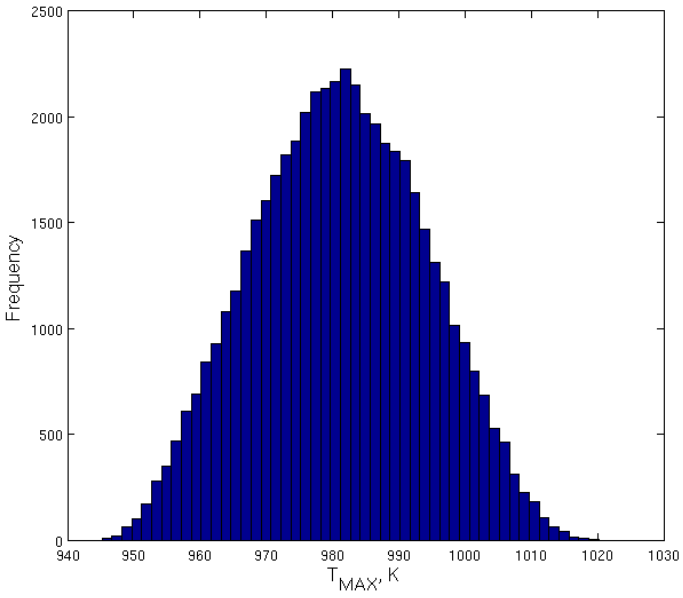

Figure 4.9: Histogram of peak temperature from HENDEL test 2311

4.5 High Temperature Test Reactor

The Hight Temperature Test Reactor (HTTR) in Japan was built to demonstrate the safety characteristics of the prismatic modular reactor (PMR). A simplified AGREE model has been built to support the analysis of the HTTR for the Loss of Forced Circulation accident (LOFC). The AGREE model is shown in Fig. 4.10 and Fig. 4.11. The model used in this analysis consists of only the core and inlet/outlet plentums, and there is no modeling of the bypass flow/crossflow paths. In this section, the input parameters are investigated for their impact on steady-state average macroscopic core temperature and peak temperature.

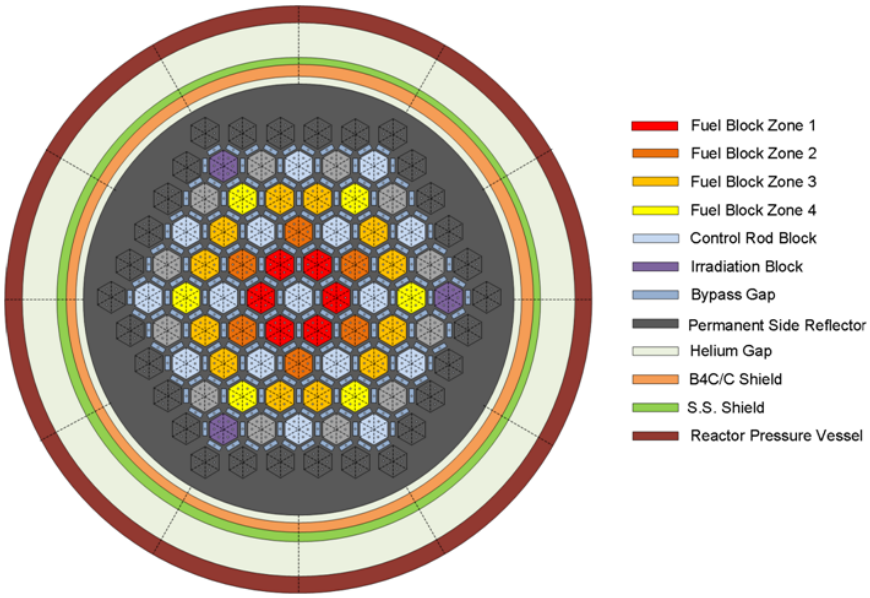

Figure 4.10: AGREE model of HTTR, top view

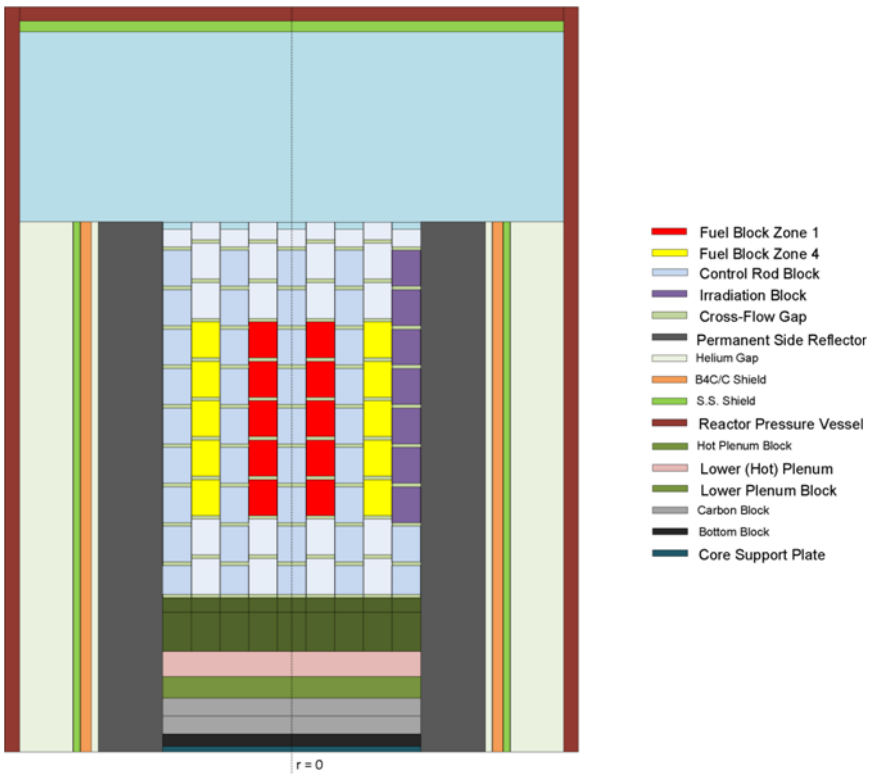

Figure 4.11: AGREE model of HTTR, side view

4.5.1 Average Macroscopic Temperature

The sensitivites of the average macroscopic temperature are stated in Table 4.12 where they have been arranged in order of significance. Adjoint verification is provided in Appendix C. It is clear from the values that the average macroscopic core temperature is dominated by the inlet boundary conditions, temperature and mass flow rate.

For the UQ evaluation, the significant input parameters are sampled over the ranges given in Table 4.13. To build the surrogate, DAKOTA is used to run 100 cases utilizing Latin-Hypercube sampling. The associated adjoint, residual, and sensitivity information from the 100 cases are stored in a surrogate library. The range of the sensitivity derivatives are shown in Fig. 4.12. With the surroage library built, 50,000 cases are run in an effort to exhaustively sample the input space. The output, provided in Fig. 4.13, demonstrates a relatively flat distribution. Due to the epistemic nature of the uncertainty, this analysis can only state that the average macroscopic temperature is $524.8 \pm 16.5\,K$ (3.1% uncertainty).

Table 4.12: Input parameters and sensitivities for HTTR test, average macroscopic temperature

SRQ, J				
T_{MAC}	524.46 K			
Input Parameters, μ				
ID	Description	Value	$\frac{dJ}{d\mu}$	$\frac{dJ/J}{d\mu/\mu}$
$T_{BC,in}$	Inlet Temperature BC	453.15 K	1.0025E+00	8.66E-01
W_{in}	Inlet mass flow rate	12.40 kg/s	-5.8587E+00	-1.39E-01
h_{J-87}	JAEA-87 HTC (Avg.)	788.5 $\frac{W}{m^2K}$	-1.6268E-03	-2.45E-03
ε	Emissivity	0.8	1.2133E+00	1.85E-03
k_{PGX}	PGX Graph. Th-Cond.	102.74 $\frac{W}{mK}$	4.5887E-03	8.99E-04
k_{IG-110}	IG-110 Grph. Th-Cond.	32.66 $\frac{W}{mK}$	3.8197E-03	2.38E-04
h_G	Gnielinski HTC (Avg.)	950.9 $\frac{W}{m^2K}$	2.2151E-05	4.02E-05
$P_{BC,out}$	Outlet Pressure BC	2.78E+06 Pa	-1.3973E-10	-7.41E-07
k_{fuel}	Fuel Compact Th-Cond.	18.0 $\frac{W}{mK}$	3.0568E-08	1.05E-09

Table 4.13: Input values and range for the HTTR test, average macroscopic temperature

ID	uncertainty	lower bounds	upper bounds
$T_{BC,in}$	$\pm 3\%$	$439.5\,K$	$466.7\,K$
W_{in}	$\pm 4\%$	$11.9\,kg/s$	$12.9\,kg/s$
h_{J-87}	$\pm 12\%$	$-95.0\,\frac{W}{m^2K}$ bias	$+95.0\,\frac{W}{m^2K}$ bias
ε	$\pm 10\%$	- 0.08 bias	+0.08 bias

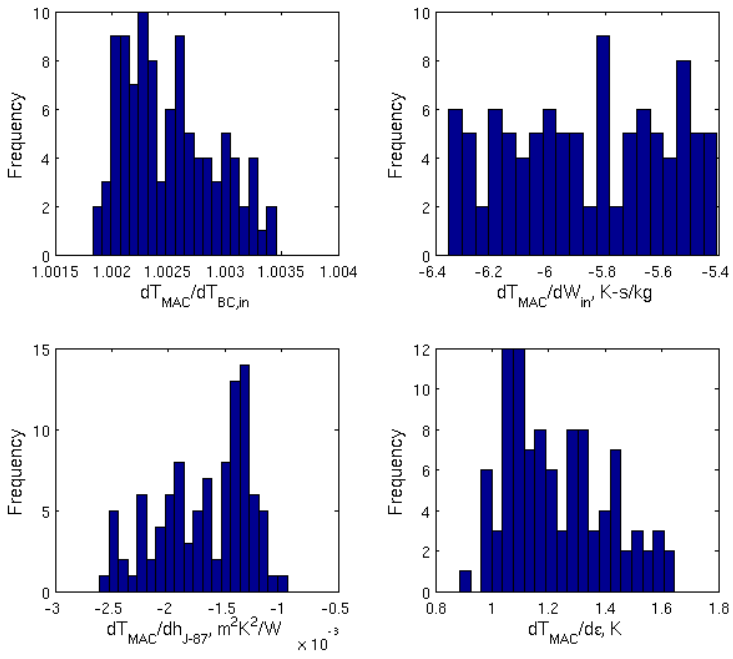

Figure 4.12: Distribution of sensitivity derivatives used in surrogate for HTTR test average macroscopic temperature

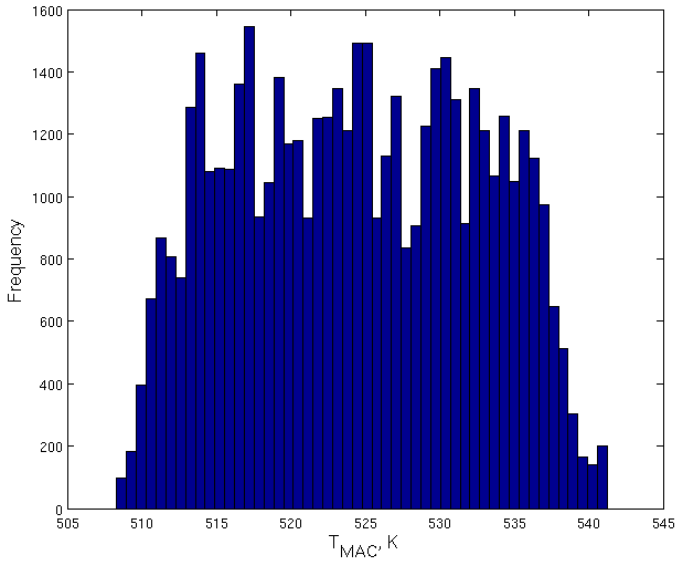

Figure 4.13: Histogram of average macroscopic temperature from HTTR test

4.5.2 Peak Temperature

The sensitivites of the peak temperature are stated in Table 4.14 where they have been arranged in order of significance. Adjoint verification is provided in Appendix C. Similar to the average macroscopic core temperature, the peak temperature is dominated by the inlet boundary conditions. The JAEA-87 heat transfer coefficient, and fuel compact thermal conductivity, however, demonstrate greater significance than was observed for the average macroscopic temperature.

Table 4.14: Input parameters and sensitivities for HTTR test, peak temperature

SRQ, J				
T_{MAX}	680.51 K			
Input Parameters, μ				
ID	Description	Value	$\frac{dJ}{d\mu}$	$\frac{dJ/J}{d\mu/\mu}$
$T_{BC,in}$	Inlet Temperature BC	453.15 K	9.4263E-01	6.28E-01
W_{in}	Inlet mass flow rate	12.4 kg/s	-1.3270E+01	-2.42E-01
h_{J-87}	JAEA-87 HTC (Avg.)	788.5 $\frac{W}{m^2K}$	-3.9752E-02	-4.61E-02
k_{fuel}	Fuel Compact Th-Cond.	18.0 $\frac{W}{mK}$	-5.0883E-01	-1.35E-02
ε	Emissivity	0.8	-5.6768E+00	-6.67E-03
k_{IG-110}	IG-110 Grph. Th-Cond. (Avg.)	32.6560 $\frac{W}{mK}$	-1.2413E-01	-5.96E-03
k_{PGX}	PGX Grph. Th-Cond. (Avg.)	102.74 $\frac{W}{mK}$	6.2889E-03	9.50E-04
$P_{BC,out}$	Outlet Pressure BC	2.78E+06 Pa	-2.5839E-08	-1.06E-04
h_G	Gnielinski HTC (Avg.)	950.9 $\frac{W}{m^2K}$	5.3303E-06	7.45E-06

For the UQ evaluation, the significant input parameters are sampled over the ranges given in Table 4.15. To build the surrogate, DAKOTA is used to run 100 cases utilizing Latin-Hypercube sampling. The associated adjoint, residual, and sensitivity information from the 100 cases are stored in a surrogate library. The range of the sensitivity derivatives are shown in Fig. 4.14. With the surroage library built, 50,000 cases are run in an effort to exhaustively sample the input space. The output, provided in Fig. 4.15, demonstrates a relatively normal distribution. Due to the epistemic nature of the uncertainty, this analysis can only state that the peak temperature is $682.4 \pm 23.1\,K$ (3.4% uncertainty).

Table 4.15: Input values and range for the HTTR test, peak temperature

ID	uncertainty	lower bounds	upper bounds
$T_{BC,in}$	$\pm 3\%$	$439.5\,K$	$466.7\,K$
W_{in}	$\pm 4\%$	$11.9\,kg/s$	$12.9\,kg/s$
h_{J-87}	$\pm 12\%$	$-95.0\,\frac{W}{m^2K}$ bias	$+95.0\,\frac{W}{m^2K}$ bias
k_{fuel}	$\pm 10\%$	$-1.8\,\frac{W}{mK}$ bias	$+1.8\,\frac{W}{mK}$ bias
ε	$\pm 10\%$	-0.08 bias	+0.08 bias
k_{IG-110}	$\pm 10\%$	$-3.2\,\frac{W}{mK}$ bias	$+3.2\,\frac{W}{mK}$ bias

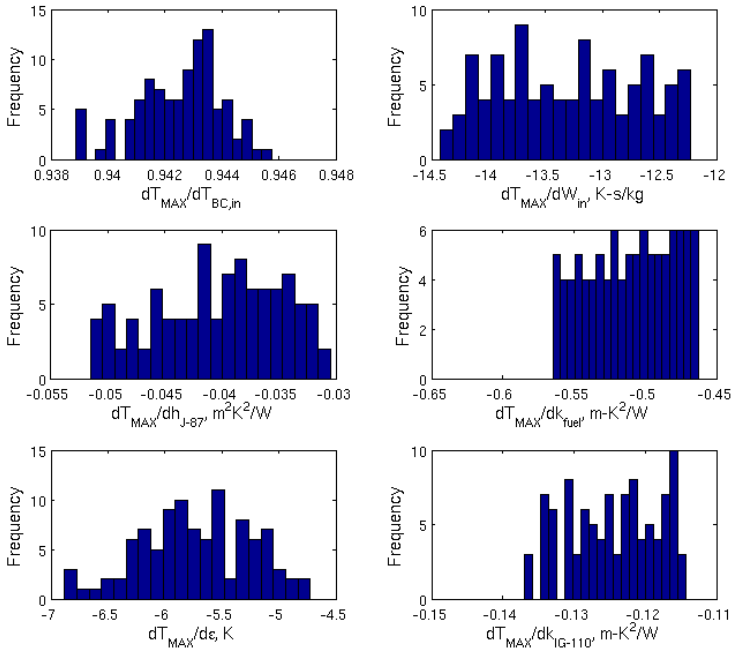

Figure 4.14: Distribution of sensitivity derivatives used in surrogate for HTTR peak temperature

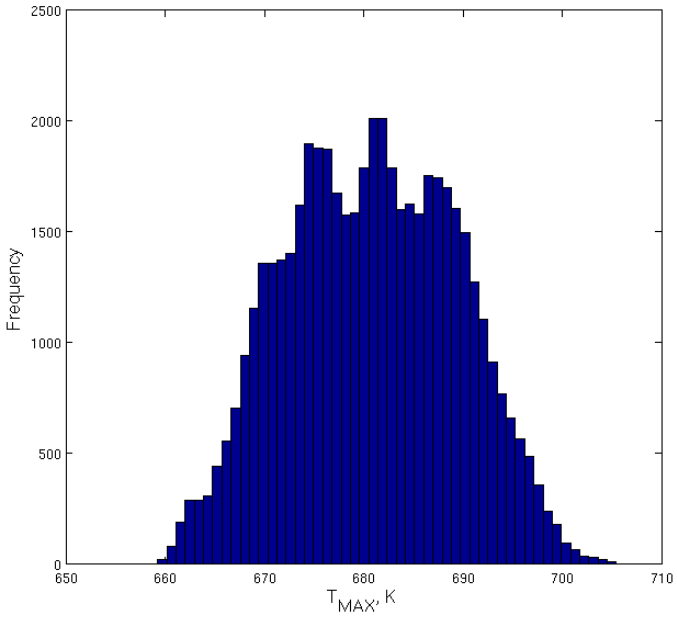

Figure 4.15: Histogram of peak temperature for HTTR test

CHAPTER 5

Conclusions, Future Research, and Lessons Learned

5.1 Conclusions

As stated in the introduction, this thesis set out to make four contributions. First was the development, verification, and validation of the AGREE thermal-fluids code. The requirements for the AGREE code and mathematical models were laid out in Ch. 2. Successful predictions of multiple flow experiments, including the JAEA bypass flow experiment, several experiments conducted as Seoul National University, and the JAEA HENDEL facility, demonstrates the ability of AGREE predict the flow field with fidelity and accuracy.

The second contribution was a generalized and simple method for the implementation of the adjoint solution into large system codes. The adjoint theory was discussed in Ch. 3 and details regarding the implementation into AGREE was discussed in Ch. 4. Successful implementation was demonstrated by running several cases related to the HTTR facility in Japan and comparing the sensitivity derivatives with those obtained via finite differencing.

The third contribution was the identification and quantification of the factors impacting bypass flow and core temperatures in the NGNP. In the analysis of the Kaburaki and Takizuka bypass flow test, the gap geometry and associated form loss coefficient were demonstrated to have significant impact on the bypass flow/crossflow. However, in the investigation of the HENDEL facility for average macroscopic core temperature and peak temperature observed within the core, gap geometry and the associated form loss coefficient were demonstrated to be insignificant (normalized sensitivity derivatives of magnitudes less than 0.001). Additionally, the thermal-conductivity of graphite in the blocks in the both the HENDEL facility and in the HTTR facility showed relatively low significance (normalized sensitivity derivatives of magnitudes typically less than 0.01) when compared with the boundary conditions (normalized sensitivity derivatives on the order of 1). It can be argued that these results are test (and HTTR) specific or that the SRQs selected are not

representative of all the important phenomena. Regarding the bypass flow, however, the importance in its modeling lies primarily on its impact on the core temperatures and the associated feedback on core reactivity. The sensitivity analysis for the HENDEL facility show that the factors impacting crossflow have little impact on the average and peak core temperatures. Thus bringing into question whether large expenditures to closely investigate the gap geometry and crossflow characteristics are warranted.

The fourth contribution was the development and study in the use of adjoint corrected approximations as a surrogate in nuclear thermal-fluids codes. In Ch. 3 an adjoint correct surrogate was derived that has a leading error term of third order. Using a surrogate produced about a single point, taken at the mean, a simple test problem demonstrated the local accuracy of the method. A method was shown for combining several of these locally accuracy surrogates. By building a surrogate library and then selecting the appropriate surrogate to sample at run-time, a collection of surrogates can be built whose accuracy is limited to the number of points placed in the surrogate library. The accuracy of the method is demonstrated on the bypass flow test of Kaburaki and Takizuka, where the surrogate library contains 100 samples, and then 50,000 cases are run using both the surroage and the true function. The surrogate reproduced the PDF of the true function with negligable discrepancy and captured the bounding (minimum and maximum) values. The method was further demonstrated by performing an exhaustive UQ evaluation for the non-trivial HENDEL and HTTR experiments.

The adjoint method, as presented here, provides much utility to the user of the code. The adjoint solution can be utilized to enhance existing UQ capabilities or to produce an accurate surrogate in order to perform exhaustive Monte-Carlo sampling on the input parameter space. The main drawback of the adjoint method lies in its intrusiveness, i.e. it requires substantial modification of the source code. Thus, it may require expert knowledge of the primal system to implement successfully.

5.2 Future Research

This thesis implemented the adjoint method into the AGREE code, but was limited to steady-state thermal-fluids analyses. There are three recommendations for extending this work. The first recommendation is to extend the adjoint to include transient analyses. The major difficulty encountered here, as highlighted in Ch. 3 is that the adjoint solution needs to be marched backwards in time. As the system of equations is non-linear, access to the solution field variables from the forward system needs to be available. The second recommendation, which follows the first recommendation and would extend the work contained

in this thesis and in the work of a previous thesis [95], is to extend the adjoint method for a coupled code, i.e. thermal-hydraulics and neutronics. Such an implementation would be a significant aid in quantifying reactor safety margins for scenarios involving strong coupling between neutronics and thermal-hydrualics. The final recommendation would be to utilize the adjoint to investigate the sensitivities in two-phase flow modeling, drift-flux and/or the two-fluid model. The number of constitutive relationships utilized in two-phase flow is significant and the the uncertainty of these relationships can be large. The adjoint implementation would provide guidance on the impact of these relationships and highlight where further experimental investigation would be most beneficial.

5.3 Lessons Learned

This final section discusses the major obstacles encountered during the research process in the hopes of providing guidance to future researchers engaging in similar work. The major obstacles encountered during this work, that were perhaps avoidable, relate to software development and access to quality experimental data.

Studies related to software development in scientific computing have revealed that 90% or more scientists engaged in software development are primarily self-taught, and therefore lack exposure to basic software development practices [96]. In the early stages of the AGREE code development many recommended software development practices were not utilized. This resulted in much of the code needed to be re-written at different stages in order to interface with different modules (e.g. coupling the fluids and solid energy equations, Jacobian implementation), which cost months of development time. It is highly recommended that future code developers invest time to learn the basic software development practices (e.g. writing maintainable code, using version control and issue trackers, code reviews, unit testing and task automation, and planning for mistakes) before embarking on what will likely become a large project.

A second recommendation regarding software development is to utilize established libraries early in the process. During the process of implementing the adjoint method into AGREE, a large amount of time was spent performing and verifying the Jacobian of the coupled system. The choice to hand differentiate, instead of using a code differentiation tool such as ADIFOR [92] or TAPENADE [93], was made due to unfamilirity with these codes and their assocatied data structure requirements. Hand differentiating ones own code is not particularly difficult, but performing the same process on code and data structures that are unfamiliar can be a time consuming and frustrating process. The Portable, Extensible Toolkit for Scientific Computation (PETSc) [97] has a library of data structures and

algorithms that operate on those data structures, such as non-linear system solvers, that would place code developers on the same page. Additionally, the the PETSc package interfaces directly with ADIFOR and has built in finite differencing for the development of the Jacobain for the coupled system.

The last recommendation is to have a code development effort be tightly coupled to an experimental program. Early development of the AGREE code relied on data available in literature and by benchmarking with other codes. Much of the experimental data used in the validation of the AGREE code proved difficult to acquire and/or understand due to language barriers. As experimental data and code development are vital to one another, it is important to have an effective mechanism for information transfer between experimentalists and their code developing colleagues.

APPENDIX A

Derivative of the Loss Term

In calculating the Jacobian, the derivative of the loss term in the momentum equation needs special attention due to a complication that results from the Darcy friction factor term. This appendix shows how the Churchill correlation is modified to provide the necessary derivative. Starting with the major loss term:

$$loss = \frac{1}{2} f \frac{l}{D} \rho |u| A \tag{A.1}$$

$$\frac{dloss}{d\rho} = \frac{1}{2} f \frac{l}{D} |u| A + \frac{1}{2} \frac{df}{d\rho} \frac{l}{D} \rho |u| A \tag{A.2}$$

Next, place the derivative in terms of the Reynolds number:

$$\frac{df}{d\rho} = \frac{df}{dRe} \frac{dRe}{d\rho} = \frac{df}{dRe} \frac{|u|D}{\mu} \tag{A.3}$$

$$\frac{dloss}{d\rho} = \frac{1}{2} f \frac{l}{D} |u| A + \frac{1}{2} \frac{df}{dRe} \frac{l}{D} \frac{\rho |u| A}{\mu} |u| A \tag{A.4}$$

$$\frac{dloss}{d\rho} = \frac{1}{2} f \frac{l}{D} |u| A \left[1 + \frac{Re}{f} \frac{df}{dRe} \right] \tag{A.5}$$

Performing the same operation for a derivative with respect to $|u|$ produces a similar result. The key point is that a normalized derivative of the friction factor with respect to the Reynolds number is required.

$$\frac{dloss}{d|u|} = \frac{1}{2} f \frac{l}{D} \rho A \left[1 + \frac{Re}{f} \frac{df}{dRe} \right] \tag{A.6}$$

The algorithm to compute the friction factor and its normalized derivative follows:

$$L = \left(\frac{8}{Re}\right)^1 2 \tag{A.7}$$

$$E = \left(\frac{7}{Re}\right)^{0.9} + 0.27\frac{\varepsilon}{D} \tag{A.8}$$

$$D = -2.457 \log E \tag{A.9}$$

$$A = D^1 6 \tag{A.10}$$

$$B = \left(\frac{37530}{Re}\right)^1 6 \tag{A.11}$$

$$T = (A+B)^{-3/2} \tag{A.12}$$

$$\boxed{f = 8(L+T)^{1/12}} \tag{A.13}$$

$$\frac{dL}{dRe} = -12\frac{L}{Re} \tag{A.14}$$

$$\frac{dA}{dD} = 16\frac{A}{D} \tag{A.15}$$

$$\frac{dD}{dE} = \frac{-2.457}{E} \tag{A.16}$$

$$\frac{dE}{dRe} = -0.9\frac{E - 0.27\frac{\varepsilon}{D}}{Re} \tag{A.17}$$

$$\frac{dA}{dRe} = \frac{dA}{dD}\frac{dD}{dE}\frac{dE}{dRe} \tag{A.18}$$

$$\frac{dB}{dRe} = -16\frac{B}{Re} \tag{A.19}$$

$$\frac{dT}{dRe} = -1.5\left(\frac{dA}{dRe} + \frac{dB}{dRe}\right)\frac{T}{A+B} \tag{A.20}$$

$$\boxed{\frac{Re}{f}\frac{df}{dRe} = Re\frac{\frac{dL}{dRe} + \frac{dT}{dRe}}{12(L+T)}} \tag{A.21}$$

APPENDIX B

Differentiation of the Abrupt Area Change Model

In calculating the Jacobian, the derivative of the abrupt area change (expansion and contraction) model used in the momentum equation needs special attention. This appendix shows how this type of junction is differentiationed with respect to the field variables. The differentation is demonstrated for a contraction. The process for the expansion is completely analogous.

The expression to be differentiated is given by Eq. B.1, where W refers to the mass flow rate, and the subscripts j and iv refer to the junction index and the inlet volume respectively.

$$Cont = \frac{1}{2}(1-\varepsilon^2)W_j \tag{B.1}$$

with,

$$\varepsilon = \frac{A}{A_{eff}} \tag{B.2}$$

$$A_{eff} = \frac{|W_j|}{W_{iv}}A_{iv} \tag{B.3}$$

Find the derivatives w.r.t W_j and W_{iv}.

$$\frac{\partial Cont}{\partial W_j} = \frac{1}{2}(1-\varepsilon^2) + \frac{\partial Cont}{\partial \varepsilon}\frac{\partial \varepsilon}{\partial W_j} \tag{B.4}$$

$$\frac{\partial Cont}{\partial W_j} = \frac{1}{2}(1-\varepsilon^2) + \frac{\partial Cont}{\partial \varepsilon}\frac{\partial \varepsilon}{\partial A_{eff}}\frac{\partial A_{eff}}{\partial |W_j|}\frac{d|W_j|}{dW_j} \tag{B.5}$$

$$\frac{\partial Cont}{\partial W_j} = \frac{1}{2}(1-\varepsilon^2) - \varepsilon W_j \frac{-\varepsilon}{A_{eff}}\frac{A_{eff}}{|W_j|}\frac{|W_j|}{W_j} \tag{B.6}$$

$$\boxed{\frac{\partial Cont}{\partial W_j} = \frac{1}{2}(1+\varepsilon^2)} \tag{B.7}$$

$$\frac{\partial Cont}{\partial W_{iv}} = \frac{\partial Cont}{\partial \varepsilon}\frac{\partial \varepsilon}{\partial A_{eff}}\frac{\partial A_{eff}}{\partial |W_{iv}|}\frac{d|W_{iv}|}{dW_{iv}} \tag{B.8}$$

$$\frac{\partial Cont}{\partial W_{iv}} = -\varepsilon W_j \frac{-\varepsilon}{A_{eff}}\frac{-A_{eff}}{|W_{iv}|}\frac{|W_{iv}|}{W_{iv}} \tag{B.9}$$

$$\boxed{\frac{\partial Cont}{\partial W_{iv}} = -\varepsilon^2 \frac{W_j}{W_{iv}}} \tag{B.10}$$

Next, find the derivatives of W_{iv} and W_j w.r.t. the field variables. The derivatives of the junction density w.r.t. the inlet and outlet volume densities are obatined using the interpolation formulas presented in Chap. 2.

$$W_{iv} = \frac{\rho_{iv}}{2}\Big[\sum_{in} uA + \sum_{out} uA\Big] \tag{B.11}$$

$$\frac{\partial W_{iv}}{\partial u_i} = \frac{1}{2}\rho_{iv}A_i \tag{B.12}$$

$$\frac{\partial W_{iv}}{\partial \rho_{iv}} = \frac{W_{iv}}{\rho_{iv}} \tag{B.13}$$

$$W_j = \rho u A \tag{B.14}$$

$$\frac{\partial W_j}{\partial u} = \rho A \tag{B.15}$$

$$\frac{\partial W_j}{\partial \rho_{iv}} = uA\frac{\partial \rho}{\partial \rho_{iv}} \tag{B.16}$$

$$\frac{\partial W_j}{\partial \rho_{ov}} = uA\frac{\partial \rho}{\partial \rho_{ov}} \tag{B.17}$$

Finally, bring all the terms together. In the equation below, the $i \neq j$ subscript refers to additional outlet junctions from the inlet volume.

$$\boxed{\frac{\partial Cont}{\partial u_{i\neq j}} = \frac{\partial Cont}{\partial W_{iv}}\frac{\partial W_{iv}}{\partial u_i}} \tag{B.18}$$

$$\boxed{\frac{\partial Cont}{\partial u} = \frac{\partial Cont}{\partial W_j}\frac{\partial W_j}{\partial u} + \frac{\partial Cont}{\partial W_{iv}}\frac{\partial W_{iv}}{\partial u}} \tag{B.19}$$

$$\boxed{\frac{\partial Cont}{\partial p_{iv}} = \left[\frac{\partial Cont}{\partial W_j}\frac{\partial W_j}{\partial \rho_{iv}} + \frac{\partial Cont}{\partial W_{iv}}\frac{\partial W_{iv}}{\partial \rho_{iv}}\right]\left(\frac{\partial \rho}{\partial p}\right)_{iv}} \tag{B.20}$$

$$\boxed{\frac{\partial Cont}{\partial T_{iv}} = \left[\frac{\partial Cont}{\partial W_j}\frac{\partial W_j}{\partial \rho_{iv}} + \frac{\partial Cont}{\partial W_{iv}}\frac{\partial W_{iv}}{\partial \rho_{iv}}\right]\left(\frac{\partial \rho}{\partial T}\right)_{iv}} \tag{B.21}$$

$$\boxed{\frac{\partial Cont}{\partial p_{ov}} = \frac{\partial Cont}{\partial W_j}\frac{\partial W_j}{\partial \rho_{ov}}\left(\frac{\partial \rho}{\partial p}\right)_{ov}} \tag{B.22}$$

$$\boxed{\frac{\partial Cont}{\partial T_{ov}} = \frac{\partial Cont}{\partial W_j}\frac{\partial W_j}{\partial \rho_{ov}}\left(\frac{\partial \rho}{\partial T}\right)_{ov}} \tag{B.23}$$

APPENDIX C

Verification of Adjoint Based Sensitivity Derivatives

This appendix contains the results of calculations used to verify the implentation of the adjoint for the average macroscopic core temperature and the peak core temperature. Verification is performed by comparing the finite differenced sensitivity derivatives against the adjoint based sensitivity derivatives. Proper implementation is verified by observing first order convergence of the finite differenced sensitivity derivatives. Difficulties of this method can arrise as it is not always possible to isolate a single input (e.g. changing a heat transfer coefficient affects the core temperature which affects thermal-physical properties), and derivatives that are small in magnitude require tightly converged solutions.

Table C.1: Verification of adjoint based sensitivity derivatives for HENDEL test 2311, average macroscopic temperature

ID	Value, μ	T_{MAC}, J	$\frac{\Delta J}{\Delta \mu}$	Error
$T_{BC,in}$	623.35	769.847	1.0088E+00	6.01E-05
	578.35	724.450	1.0088E+00	4.78E-05
	573.85	719.911	1.0088E+00	7.32E-05
W_{in}	0.2200	706.030	-6.6884E+02	6.86E+001
	0.2020	717.946	-7.2998E+02	7.42E+000
	0.2002	719.259	-7.3669E+02	7.12E-001
h_G	747.23	719.279	-2.5550E-03	4.58E-004
	702.23	719.392	-2.9565E-03	5.69E-005
	697.73	719.405	-2.9952E-03	1.83E-005
h_{J-90}	626.24	719.298	-2.1676E-03	5.15E-004
	581.24	719.393	-2.6325E-03	5.02E-005
	576.74	719.405	-2.6755E-03	7.17E-006
$k_{graphite}$	101.09	719.012	-7.8800E-03	1.38E-002
	56.09	719.301	-2.1034E-02	6.49E-004
	51.59	719.394	-2.4849E-02	-3.17E-003
G-W	0.0040	719.675	1.3408E+02	-1.73E+002
	0.0022	719.462	2.7583E+02	-3.13E+001
	0.00202	719.412	3.0442E+02	-2.76E+000
G-K	6.820	719.376	-8.8524E-03	8.12E-002
	3.751	719.376	-8.8524E-02	1.56E-003
	3.444	719.403	-8.9839E-02	2.41E-004

Table C.2: Verification of adjoint based sensitivity derivatives for HENDEL test 2311, peak temperature

ID	Value, μ	T_{MAC}, J	$\frac{\Delta J}{\Delta \mu}$	Error
$T_{BC,in}$	623.350	1029.653	9.8133E-01	7.51E-03
	578.350	985.491	9.8091E-01	7.08E-03
	573.850	981.077	9.8087E-01	7.04E-03
W_{in}	0.2200	956.250	-1.2168E+03	3.47E+02
	0.2020	977.467	-1.5598E+03	3.98E+00
	0.2002	980.273	-1.5698E+03	-6.05E+00
k_{heat}	20.0	956.250	-2.4337E+00	3.78E+00
	11.0	974.919	-5.6680E+00	5.48E-01
	10.1	979.969	-6.1731E+00	4.30E-02
h_{J-90}	626.24	977.975	-5.2232E-02	2.29E-03
	581.24	980.314	-5.4640E-02	-1.13E-04
	576.74	980.559	-5.4893E-02	-3.66E-04
$k_{graphite}$	101.09	975.773	-9.6267E-02	1.15E-01
	56.09	979.614	-1.9464E-01	1.70E-02
	51.59	980.479	-2.1567E-01	-3.99E-03
h_G	747.23	980.575	-2.4349E-04	4.68E-05
	702.23	980.585	-2.8660E-04	3.69E-06
	697.73	980.587	-2.9201E-04	-1.73E-06

Table C.3: Verification of adjoint based sensitivity derivatives for HTTR, average macroscopic temperature

ID	Value, μ	T_{MAC}, J	$\frac{\Delta J}{\Delta \mu}$	Error
$T_{BC,in}$	498.46500	569.885	1.0024E+00	-3.98E-05
	457.68150	529.002	1.0022E+00	-2.32E-04
	453.60315	524.915	1.0022E+005	-2.56E-04
W_{in}	13.64	517.869	-5.3154E+00	5.43E-001
	12.524	523.742	-5.7976E+00	6.11E-002
	12.4124	524.388	-5.8507E+00	8.05E-003
h_{J-87}	867.4	524.351	-1.3919E-03	2.35E-04
	796.4	524.448	-1.5873E-03	3.96E-05
	789.3	524.459	-1.6095E-03	1.73E-05
ε	0.900	524.588	1.2756E+00	6.23E-02
	0.810	524.472	1.2077E+00	-5.66E-03
	0.801	524.462	1.2013E+00	-1.21E-02
k_{PGX}	202.7	524.787	3.2690E-03	-1.32E-03
	112.7	524.504	4.3989E-03	-1.90E-04
	103.7	524.465	4.5673E-03	-2.14E-05
k_{IG-110}	62.7	524.521	2.0359E-03	-1.78E-03
	35.7	524.471	3.5381E-03	-2.82E-04
	33.0	524.462	3.8204E-03	7.28E-07
h_G	1045.9	5.245E+02	2.0216E-05	-1.93E-06
	960.4	5.245E+02	2.1940E-05	-2.11E-07
	951.9	5.245E+02	2.2129E-05	-2.18E-08

Table C.4: Verification of adjoint based sensitivity derivatives for HTTR, peak temperature

ID	Value, μ	T_{MAC}, J	$\frac{\Delta J}{\Delta \mu}$	Error
$T_{BC,in}$	498.46500	723.312	9.4454E-01	1.91E-03
	457.68150	684.780	9.4234E-01	-2.91E-04
	453.60315	680.937	9.4213E-01	-4.97E-04
W_{in}	13.6400	665.524	-1.2086E+01	1.18E+000
	12.5240	678.881	-1.3137E+01	1.33E-001
	12.4124	680.346	-1.3252E+01	1.78E-002
h_{J-87}	867.4	677.649	-3.6289E-02	3.46E-03
	796.4	680.200	-3.9351E-02	4.02E-04
	789.3	680.479	-3.9685E-02	6.69E-05
k_{fuel}	36.00	675.930	-2.5442E-01	2.54E-01
	19.80	679.677	-4.6258E-01	4.63E-02
	18.18	680.419	-5.0380E-01	5.03E-03
ε	0.900	679.900	-6.9075E+00	-4.21E-01
	0.810	680.453	-5.7404E+00	-6.36E-02
	0.801	680.504	-5.7070E+00	-3.02E-02
k_{IG-110}	62.7	678.370	-7.1323E-02	5.28E-02
	35.7	680.165	-1.1492E-01	9.20E-03
	33.0	680.473	-1.2307E-01	1.06E-03
k_{PGX}	202.7	680.984	4.7371E-03	-1.55E-03
	112.7	680.571	6.0857E-03	-2.03E-04
	103.7	680.516	6.2632E-03	-2.57E-05
$P_{BC,out}$	3.05800E+06	680.503	-2.4981E-08	8.58E-10
	2.80780E+06	680.509	-2.5732E-08	1.06E-10
	2.78278E+06	680.510	-2.5808E-08	3.11E-11
h_G	1045.9	680.510	4.8673E-06	-4.63E-07
	960.4	680.510	5.2781E-06	-5.22E-08
	951.9	680.510	5.3230E-06	-7.28E-09

BIBLIOGRAPHY

[1] R.W. Hamming. *Numerical Methods for Scientists and Engineers*. McGraw-Hill Book Compancy Inc., 1962.

[2] W.L. Oberkampf and C.J. Roy. *Verification and Validation in Scientific Computing*. Cambridge University Press, 2010.

[3] Emergency Core Cooling System; Revisions to Acceptance Criteria. Technical Report Federal Reister 53 (180), pp. 35996-36005, September 16, 1988.

[4] B.E. Boyack et. al. Quantifying Reacor Safety Margins Part 1: An Overview of the Code Scaling, Applicability, and Uncertainty Evaluation Methodology. *Nuclear Engineering and Design*, 119:1–15, 1990.

[5] G.E. Wilson et. al. Quantifying Reacor Safety Margins Part 2: Characterization of Important Contributors to Uncertainty. *Nuclear Engineering and Design*, 119:17–31, 1990.

[6] W. Wulff et. al. Quantifying Reacor Safety Margins Part 3: Assessment and Ranging of Parameters. *Nuclear Engineering and Design*, 119:33–65, 1990.

[7] G.S. Lellouche and S. Levy et. al. Quantifying Reacor Safety Margins Part 4: Uncertainty Evaluation of LBLOCA Analysis Based on TRAC-PF1/MOD 1. *Nuclear Engineering and Design*, 119:67–95, 1990.

[8] N. Zuber and G.E. Wilson et. al. Quantifying Reacor Safety Margins Part 5: Evaluation of Scale-Up Capabilities of Best Estimate Codes. *Nuclear Engineering and Design*, 119:97–105, 1990.

[9] H.Zhao and V.A. Mousseau. Use of Forward Sensitivity Analysis Method to Improve Code Scaling, Applicability, and Uncertainty (CSAU) Methodology. *Nucl. Eng. and Des.*, 239:188–196, 2012.

[10] R.W. Fox and A.T. McDonald. *Introduction to Fluid Mechanics 5th Ed.* John Wiley and Sons Inc., 1998.

[11] B.M. Adams, K.R. Dalbey, M.S. Eldred, L.P. Swiler, W.J. Bohnhoff, J.P. Eddy, D. M. Vigil, P.D. Hough, and S. Lefantzi. DAKOTA, A Multilevel Parallel Object-Ocriented Framework for Design Optimization Parameter Estimation, Uncertainty Quantification, and Sensitivity Analysis. Technical Report SAND2006-5001, SANDIA National Laboratories, 2006.

[12] G. Iaccarnio. Quantification of Uncertainty in Flow Simulations Using Probalilistic Methods. VKI Lecture Series, Sept. 8-12 2008.

[13] C.R. Roy and W.L. Oberkampf. A comprehensive framework for verification, validation, and uncertainty quantification in scientific computing. *Computer Methods in Appliced Mechanics and Engineering*, 200:2131–2144, 2011.

[14] R.P. Martin and L.D. O'Dell. AREVA's Realistic Large Break LOCA Analysis Methodology. *Nuclear Engineering and Design*, 235:1713–1725, 2005.

[15] H. Glaeser. GRS Method for Uncertainty and Sensitivity Evaluation of Code Results and Applications. *Science and Technology of Nuclear Intallations*, 2008.

[16] C. Frepoli. An Overview of Westinghouse Realistic Large Break LOCA Evaluation Model. *Science and Technology of Nuclear Intallations*, 2008.

[17] S.S. Wilks. Determination of Sample Sizes for Setting Tolerance Limits. *Ann. Math. Stat.*, 12:91–96, 1941.

[18] W.T. Nutt and G.B. Wallis. Evaluation of Nuclear Safety from teh Outputs of Computer Codes in the Presence of Uncertainties. *Reliab. Eng. Sys. Safety*, 83:57–77, 2004.

[19] J.C. Lee and N.J. McCormick. *Risk and Safety Analysis of Nuclear Systems*. John Wiley and Sons Inc., 2011.

[20] P. G. Constantine. Stanford ME-470: Uncertainty Quantification course notes. Spring 2010/2011.

[21] J.R. Koehelr and A.B. Owen. *Handbook of Statistics, 13*. Elsevier Science, 1996.

[22] J. H. Friedman. Multivariate Adaptive Regression Splines. *Ann. Stat.*, 19:1–141, 1991.

[23] L. Breiman and J. H. Friedman. Estimating Optimal Transformations for Multiple Regression and Correlation. *Journal of American Statistical Association*, 80:580–598, 1985.

[24] H.G. Kim and J.C. Lee. Development of a Generalized Critical Heat Flux Correlation through the Alternating Conditional Expectation Algoritm. *Nuclear Science and Engineering*, 127:300–316, 1997.

[25] C.E. Rasmussen and K.I. WIlliams. *Gaussian Process for Machine Learning*. MIT Press, 2006.

[26] M. Pilch, T.G. Trucano, and J.C. Helton. Ideas Underlying Quantification of Margins and Uncertainties (QMU): A White Paper. Technical Report SAND2010-2183, SANDIA National Laboratories, 2009.

[27] D.A. Fynan, K.I. Ahn, H.G. Lim, and J.C. Lee. Uncertainty Quantification of LBLOCA PCT for a Pressurized Water Reactor by ACE Algorithm and Gaussian Process Model. In *The 18th Pacific Basin Nuclear Conference (PBNC 2012)*, Busan, Korea, March 18-23, 2012.

[28] A.A. Giunta, J.M. McFarland, L.P. Swiler, and M.S. Eldred. The Promise and Peril of Uncertainty Quantification Using Response Surface Approximations. *Structure and Infrastructure Engineering*, 2:175–189, 2006.

[29] J.P. Boyd. *Chebyshev and Fourier Specral Mehtods, 2nd Ed.* Dover Publications Inc., 2001.

[30] D. Xiu and G.E. Karniadakis. The Wiener-Askey Polynomical Chaos for Stochastic Differential equations. *SIAM Journal on Scientific Computing*, 24:619–644, 2002.

[31] Q. Wang. *Uncertainty Quantification for Unsteady Fluid Flow Using Adjiont Based Approaches*. PhD thesis, Stanford University, 2008.

[32] M. Martinelli and R. Duvigneau. On the use of second-order derivatives and metamodel-based monte-carlo for uncertainty estimation in aerodynamics. *Computers and Fluids*, 39:953–964, 2010.

[33] V. Seker. *Multiphysics Methods Development for High Temperature Gas Cooled Reactor Analysis*. PhD thesis, Purdue University, 2007.

[34] T.J. Downar et. al. PARCS: Purdue Advanced Reactor Core Simulator. In *PHYSOR 2002*, Seoul, Korea, October 7-10, 2002.

[35] T.J. Drzewiecki, V. Seker, T.J. Downar, J.M. Kelly, and N. Hudson. Analysis of Prismatic High Temperature Reactor with AGREE. In *HTR 2010*, Prague, Czech Republic, October 18-20, 2010.

[36] T.J. Drzewiecki, V. Seker, T.J. Downar, and J.M. Kelly. The US NRC Advanced Gas Reactor Evalulator (AGREE). In *NURETH-14*, Toronto, Ontario, Canada, September 25-30, 2011.

[37] V. Seker, T .Drzewiecki, T. Downar, and J.M. Kelly. Modeling Prismatic HTGRs with the US NRC Advanced Gas Reactor Evaluator (AGREE). In *PHYSOR 2012*, Knoxville, Tennessee, USA, April 15-20, 2012.

[38] N.I. Tak, M.M. Kim, H.S. Lim, J.M. Noh, T.J. Drzewiecki., and V. Seker.J. Downar. Validation of Numerical Methods to Calculate Bypass Flow in a Prismatic Gas-Cooled Reactor Core. In *ICAPP 2013*, Jeju Island, Korea, April 14-18, 2013.

[39] N.I. Tak, V. Seker, T.J. Drzewiecki, J.M. Kelly, and T.J. Downar. Verification and Validation of Heat Transfer Model of AGREE Code. In *Transactions of the Korean Nuclear Society Spring Meeting*, Gwangju, Korea, May 29-31, 2013.

[40] M.H. Kim, N.I. Tak, and J.M. Noh. CFD Benchmark Study on Cross Flow Experiment in Prismatic HTGR Core Fuel Blocks. In *The 15th International Topical Meeting on Nuclear Reactor Thermal-Hydraulics (NURETH-15)*, Pisa, Italy, May 12-17, 2013.

[41] D.G. Cacuci and M. Ionescu-Bujor. Anjoint Sensitivity Analysis of the RELAP5/MOD3.2 Two-Fluid Thermal-Hydraulic Code System I: Theory. *Nuclear Science and Engineering*, 136:59–84, 2000.

[42] D.G. Cacuci, C.F. Weber, E.M. Oblow, and J.H Marable. Sensitivity Theory for General Systems of Non-linear Equations. *Nuclear Science and Engineering*, 75:88, 1980.

[43] D.G. Cacuci. Sensitivity Theory for Nonlinear Systems: I. Nonlinear Functional Analysis Approach. *Journal of Mathematical Physics*, 22:2794, 1981.

[44] D.G. Cacuci. Sensitivity Theory for Nonlinear Systems: II. Extensions to Additional Classes of Responses. *Journal of Mathematical Physics*, 22:2794, 1981.

[45] S.V. Patankar. *Numerical Heat Transfer and Fluid Flow*. Taylor and Francis, 1980.

[46] H.K. Versteeg and W. Malalasekera. *An Introduction to Computational Fluid Dynamics: The Finite Volume Method*. Pearson Prentice Hall, 1995.

[47] A. Stück and T. Rung. Adjoint Complement to Viscous Finite-Volume Pressure-Correction Methods. *Journal of Computational Physics*, (In Press).

[48] Next Generation Nuclear Plant Phenomena Identification and Ranking Tables (PIRTs), Volume 1: Main Report. Technical Report NUREG/CR-6944, March 2008.

[49] M.M. Putko, A.C. Taylor III, P.A. Newman, and L.L. Green. Approach for Input Uncertainty Propagation and Robust Design in CFD Using Sensitivity Derivatives. *Transactions of the ASME*, 124:60–69, 2002.

[50] Q. Wang, K. Duraisamy, J.J. Alonso, and G. Iaccarino. Risk Assessment of Scramjet Unstart Using Adjoint-Based Sampling Methods. In *AIAA 2010*, Orlando, Florida, USA, April 12-15, 2010.

[51] Next Generation Nuclear Plant Licensing Strategy. A Report to Congress. Technical report, US Nuclear Regulatory Commision and the US Department of Energy, August 2008.

[52] R.B. Vilim, W.D. Pointer, and T.Y.C. Wei. Prioritization of VHTR System Modeling Needs Based on Identification, Ranking, and Sensitivity Studies. Technical Report ANL-GenIV-071, April 2006.

[53] A.Shenoy. Reacor System Design. In *GT-MHR Technology Course)*, December 10-12, 2001.

[54] B.L. Strain. FLOPSY II a A Digital Computer Program for Calculating Flow and Pressure Drops in Hydraulic Networks. Technical Report KAPL-3030, 1965.

[55] R.B. Vilim. GAS-NET: A Two-Dimensional Network Code for Prediction of Core Flow and Temperature Distribution in the Prismatic Gas Reactor. In *ICAPP 2007*, Nice, France, May 13-18, 2007.

[56] R. Stainsby, A. Grief, and W. Worsley. Investigation of Local Heat Transfer Phenomena in a Prismatic Modular Reactor Core. Technical Report NR001/RP/001 R1, AMEC NSS Limited, March 30, 2009.

[57] J.P. Simoneau, J. Champigny, B. Mays, and L. Lommers. Three-dimensional simulation of the coupled convective, conductive, and radiative heat transfer during decay heat removal in an HTR. *Nuclear Engineering and Design*, 237:1923–1937, 2007.

[58] W.D. Pointer, C.H. Lee, J.W. Thomas, Y.S. Jung, and W.S. Yang. Steadyt-State, Whole-Core VHTR Simulation with Consistent Coupling of Neutronics and Thermofluid Analysis. Technical Report ANL-GenIV-121, September 2009.

[59] C.W. Stewert, C.L. Wheeler, R.J. Cena, C.A. McMonagle, J.M. Cuta, and D.S. Trent. COBRA-IV: The Model and the Method. Technical Report BNWL-2214, Battelle Pacific Northwest Laboratories, July 1977.

[60] C.W. Stewert, J.M Cuta, S.D. Montgomery, J.M Kelly, K.L. Basehore, T.L. George, and D.S. Rowe. VIPRE-01: A Thermal-Hydraulic Code for Reator Cores. Technical Report NP-2511-CCM, Volume 1, Rev 2, Battelle Pacific Northwest Laboratories, July 1985.

[61] T.J. Drzewiecki, V. Seker, and T.J. Downar. Software Requirements Specification Document, PMR Core Fluids Modeling in AGREE. Technical Report UM-NERS-10-0002, March 2010.

[62] M. Ishii and T. Hibiki. *Thermo-Fluid Dynamics of Two-Phase Flow*. Springer, 2006.

[63] RELAP5-3D Code Development Team. RELAP5-3D Code Manual Volume I: Code Structure, System Models, and Solution Methods. Technical Report INEEL-EXT-98-00834, June 2005.

[64] V.L. Streeter. *Handbook of Fluid Dynamics*. McGraw-Hill Book Co., 1961.

[65] H. Petersen. The Properties of Helium: Density, Specific Heats, Viscosity, and Thermal Conductivity at Pressures from 1 to 100 bar and from Room Temperature to about 1800 K. Technical Report Risö Report No. 224, Danish Atomic Energy Commission, September 1970.

[66] Reactor Core Design for High-Temperature Gas-Cooled Reactor, Part 1: Calculation of the Material Properties of Helium. Technical Report KTA 3102.1, Nuclear Safety Standards Commission (KTA), June 1978.

[67] S.W. Churchill. Friction factor equation spans all fluid-flow regimes. *Chemcial Engineering*, 91, 1977.

[68] C.F. Colebrook. Turbulent Flow in Pipes, with Particular Reference to the Transition between the Smooth and Rough Pipe Laws. *Journal of the Institution of Civil Engineerings, London*, 11:133–156, 1938-1939.

[69] H.Kaburaki and T. Takizuka. Effect of Crossflow on Flow Distribution on HTGR Core Column. *Journal of Nuclear Science and Technology*, 24:516–525, 1987.

[70] S.J. Yoon, Y.J. Cho, K.Y. Kim, and M.H. Kim. Experimental Evaluation of the Bypass Flow in the VHTR Core. In *Transcations of SMiRT 19*, Toronto, Ontario, Cananda, August 12-17, 2007.

[71] G.C. Park, S.J. Yoon, and C.Y. Jin. Fundamental Thermal-Fluid Experiment for Optimum Design of Very High Temperature Reactor. Technical Report KAERI/CM-1127/2008, Korea Atomic Energy Research Institute, April 2009.

[72] S.J. Yoon, C.Y. Yin, M.H. Kim, and G.C. Park. Experimental and Computational Assessment of Core Bypass Flow in Block-Type Very High Temperature Reactor. *Nuclear Technology*, 175:419, 2011.

[73] S.J. Yoon, C.Y. Yin, J.H. Lee, and Y.G. Lee. Study on the Flow Distribution in Prismatic VHTR Core with a Multi-Block Experiment and CFD Analysis. *Nuclear Engineering aned Design*, 241:5174, 2011.

[74] G.C. Park, S.J. Yoon, J.H Lee, and Y.G. Lee. Fundamental Thermal-Fluid Experiments for the Evaluation of the Bypass Flow in the VHTR Core. Technical Report KAERI/CM-1449/2010, Korea Atomic Energy Research Institute, December 2011.

[75] M.H. Kim et. al. Experimental and Analytic Study on the Core Bypass Flow in a Very High Temperature Reactor. Technical Report KAERI/RR-3293/2010, Korea Atomic Energy Research Institute, December 2011.

[76] S.J. Yoon, J.H. Lee M.H. Kim, and G.C. Park. The Effects of Crossflow Gap and Axial Bypass Gap Distribution on the Flow Characteristics in Prismatic VHTR Core. *Nuclear Engineering aned Design*, 250:465–479, 2012.

[77] W.D. Pointer. CFD Predictions of Gap Bypass in Prismatic VHTR Cores. *Transcations of the American Nuclear Society*, 103:897, Las Vegas, Nevada, November 7-11, 2010.

[78] J.M. Noh et. al. Development of Very High Temperature Reactor Design Technology. Technical Report KAERI/RR-3462/2011, Korea Atomic Energy Research Institute, 2012.

[79] M.H. Kim and H.S. Lim. Evaluation of the Influence of Bypass Flow Gap Distribution on the Core Hot Spot in Prismatic VHTR Core. *Nuclear Engineering and Design*, 241:3076, 2011.

[80] H.S. Lim and H.C. No. GAMMA Multidimensional Multicomponent Mixture Analysis to Predict Air Ingress Phenomena in HTGR. *Nuclear Science and Engineering*, 152:87–97, 2006.

[81] M.H. Kim, H.S. Lim, and N.I. Tak. Computational Assessment of Bypass Flow in a Multi-Block Air Test. In *Transactions of the Korean Nuclear Society Spring Meeting*, Pyeongchang, Korea, May 27-28, 2010.

[82] R.B. Vilim. Coolant Distribution in the VHTR Prismatic Core. In *ICAPP 2010*, San Diego, CA, USA, Jun 13-17, 2010.

[83] N.A. Pierce and M.B. Giles. Adjiont Recovery of Superconvergent Functionals from PDE Approximations. *SIAM Review*, 42:247–264, 2000.

[84] M.L. Williams. *CRC Handbook of Nuclear Reactor Calculations, Vol. III (p. 63-188)*. CRC Press, 1986.

[85] C.R. Weisbin, E.M. Oblow, J.H. Marable, R.W. Peelle, and J.L. Lucius. Application of Sensitivity and Uncertainty Methodology to Fast Reactor Integral Experiment Analysis. *Nuclear Science and Engineering*, 66:307–333, 1978.

[86] T.J. Downar and H. Khalil. Uncertainty in the Burnup Reactivity Swing of Liquid-Metal Fast Reactors. *Nuclear Science and Engineering*, 109:278–296, 1991.

[87] J.L. Lewmins. *Importance - The Adjoint Function*. Pergamon Press, 1965.

[88] M.B. Giles and N.A. Pierce. An Introduction to the Adjoint Approach to Desgin. *Flow, Turbulence, and Comustion*, 65:393–415, 2000.

[89] D.Ghate and M.B. Giles. Inexpensive Monte Carlo Uncertainty Analysis. In *SAROD-2005*, Hyderabad, India, December 8-9, 2005.

[90] M.D. McKay, R.J. Beckman, and W.J. Conover. A Comparison of Three Methods for Selecting Values of Input Variables in the Analysis of Output from a Computer Code. *Technometrics*, 21:239–245, 1979.

[91] S.Maruyama, N. Fujimoto, S. Fujii, T. Watanabe, and Y. Sudo. Verification of Fuel Temperature Analysis Code TEMDIM. Technical Report JAERI-M 88-170, August 1988.

[92] C. Bischof, A. Carle, P. Hovland, P. Khademi, and A. Mauer. ADIFOR 2.0 User's Guide. Technical Report ANL/MCS-TM-192, Argonne National Lab, June 1998.

[93] L. Hascoët and V. Pascual. The Tapenade Automatic Differentiation tool: Principles, Model, and Specification. *ACM Transactions On Mathematical Software*, 39(3), 2013.

[94] W.H. Press, S.A. Teukolsky, W.T. Vetterling, and B.P. Flannery. *Numerical Reipcies, 3rd Ed.: The Art of Scientific Computing*. Cambridge University Press, 2007.

[95] A. Ward. *A Newton-Krylov Solution to the Coupled Neutronics-Porous Medium Equations*. PhD thesis, University of Michigan, 2013.

[96] Greg Wilson, D. A. Aruliah, C. Titus Brown, Neil P. Chue Hong, Matt Davis, Richard T. Guy, Steven H. D. Haddock, Katy Huff, Ian M. Mitchell, Mark Plumbley, Ben Waugh, Ethan P. White, and Paul Wilson. Best practices for scientific computing. *CoRR*, abs/1210.0530, October 2012.

[97] Satish Balay, Jed Brown, , Kris Buschelman, Victor Eijkhout, William D. Gropp, Dinesh Kaushik, Matthew G. Knepley, Lois Curfman McInnes, Barry F. Smith, and Hong Zhang. PETSc users manual. Technical Report ANL-95/11 - Revision 3.4, Argonne National Laboratory, 2013.